SYNTHESES OF CONJUGATED POLYMERS AND INVESTIGATION THE EFFECT OF GOLD NANOPARTICLE - THIOL INTERACTION FOR ORGANIC SOLAR CELL APPLICATION

A THESIS SUBMITTED TO
THE GRADUATE SCHOOL OF NATURAL AND APPLIED SCIENCES
OF
MIDDLE EAST TECHNICAL UNIVERSITY

BY

SELİN GÜLMEZ

IN PARTIAL FULFILLMENT OF THE REQUIREMENTS
FOR
THE DEGREE OF MASTER OF SCIENCE
IN
CHEMISTRY

AUGUST 2022

Approval of the thesis:

SYNTHESES OF CONJUGATED POLYMERS AND INVESTIGATION THE EFFECT OF GOLD NANOPARTICLE - THIOL INTERACTION FOR ORGANIC SOLAR CELL APPLICATION

submitted by **SELİN GÜLMEZ** in partial fulfillment of the requirements for the degree of **Master of Science** i**n Chemistry, Middle East Technical University** by,

Prof. Dr. Halil Kalıpçılar
Dean, Graduate School of **Natural and Applied Sciences** _____

Prof. Dr. Özdemir Doğan
Head of the Department, **Chemistry** _____

Prof. Dr. Ali Çırpan
Supervisor, **Chemistry, METU** _____

Examining Committee Members:

Prof. Dr. Levent Kamil Toppare
Chemistry, METU _____

Prof. Dr. Ali Çırpan
Chemistry, METU _____

Prof. Dr. Atilla Cihaner
Chemical Engineering, Atılım Uni. _____

Assoc. Prof. Dr. Emrullah Görkem Günbaş
Chemistry, METU _____

Assist. Prof. Dr. Erol Yıldırım
Chemistry, METU _____

Date: 31.08.2022

I hereby declare that all information in this document has been obtained and presented in accordance with academic rules and ethical conduct. I also declare that, as required by these rules and conduct, I have fully cited and referenced all material and results that are not original to this work.

Name Last name : Selin Gülmez

Signature :

ABSTRACT

SYNTHESES OF CONJUGATED POLYMERS AND INVESTIGATION THE EFFECT OF GOLD NANOPARTICLE - THIOL INTERACTION FOR ORGANIC SOLAR CELL APPLICATION

Gülmez, Selin
Master of Science, Chemistry
Supervisor : Prof. Dr. Ali Çırpan

August 2022, 95 pages

In this thesis, five benzo[*c*][1,2,5] thiadiazole-based conjugated polymers were synthesized. Four of them were synthesized via Stille and Suzuki coupling reactions and the remaining one was synthesized by post-polymerization. The effect of functional groups of the tip of the alkyl chain was analyzed. Moreover, thiol group and gold nanoparticle interaction on the organic solar cell efficiency for P1-SH were investigated. Electronic and optical band gaps of polymers were found as 1.85/1.81, 1.95/1.85, 1.83/1.95, 1.87/1.87, and 1.83/1.85 eV respectively for P1, P1-Br, P1-SH, P2, and P3. Furthermore, the effect of the addition of gold nanoparticles to the active layer of organic solar cells on photovoltaic properties was investigated. Gel permeation chromatography (GPC), thermal gravimetric analysis (TGA), differential scanning calorimeter (DSC), and UV-Vis-NIR spectroscopy were used to evaluate the synthesized polymers. By using the cyclic voltammetry (CV) technique, redox behaviors and electronic band gaps of polymers were examined. In a nitrogen-filled glovebox setup, device manufacture and current/voltage property measurements were performed. Synthesized polymers served as the donor units for the typical type

device structure of ITO/PEDOT:PSS/polymer:$PC_{71}BM$/LiF/Al, with $PC_{71}BM$ serving as the acceptor unit. Under 100 mW cm^{-2} light, the photovoltaic characteristics of the built-in devices were measured. Best device performances in terms of PCE were found as 2.06 % for P1, 1.52 % for P1-Br, 1.22 % for P1-SH. Photovoltaic studies of P1-SH:AuNPs were investigated and the best device performances in terms of PCE were found as 1.08 %.

Keywords: Conjugated Polymers, Gold Nanoparticles, Benzothiadiazole, Power Conversion Efficiency

ÖZ

ORGANİK GÜNEŞ HÜCRELERİ UYGULAMASI İÇİN KONJÜGE POLİMER SENTEZİ VE ALTIN NANOPARTİKÜL - TİOL ETKİLEŞİMİNİN İNCELENMESİ

Gülmez, Selin
Yüksek Lisans, Kimya
Tez Yöneticisi: Prof. Dr. Ali Çırpan

Ağustos 2022, 95 sayfa

Bu tezde beş adet benzo[c][1,2,5]tiadiazol bazlı konjuge polimer sentezlenmiştir. Bunlardan dördü Stille ve Suzuki kenetlenme tepkimeleri ile sentezlenmiştir ve geri kalan polimer, post-polimerizasyon ile sentezlendi. Alkil zincirinin ucundaki fonksiyonel grupların etkisi analiz edildi. Ayrıca, P1-SH için organik güneş pili verimliliği üzerindeki tiyol grubu ve altın nanoparçacık etkileşimi araştırıldı. Polimerlerin elektronik ve optik bant aralıkları P1, P1-Br, P1-SH, P2 ve P3 için sırasıyla 1.85/1.81, 1.95/1.85, 1.83/1.95, 1.87/1.87 ve 1.83/1.85 eV olarak bulunmuştur. Ayrıca, organik güneş pillerinin aktif tabakasına altın nanoparçacıkların eklenmesinin fotovoltaik özellikler üzerindeki etkisi araştırılmıştır. Sentezlenen polimerleri değerlendirmek için jel geçirgenlik kromatografisi (GPC), termal gravimetrik analiz (TGA), diferansiyel taramalı kalorimetre (DSC) ve UV-Vis-NIR spektroskopisi kullanıldı. Döngüsel voltametri (CV) tekniği kullanılarak polimerlerin redoks davranışları ve elektronik bant boşlukları incelenmiştir. Nitrojen dolu bir eldivenli kabin sisteminde cihaz üretimi ve akım/gerilim özelliği ölçümleri yapılmıştır. Sentezlenen polimerler, ITO/PEDOT:PSS/polimer:$PC_{71}BM$/LiF/Al'nin tipik tip cihaz yapısı için verici

birimler olarak görev yaptı ve $PC_{71}BM$ alıcı birim olarak hizmet etti. 100 mW cm^{-2} ışık altında, cihazların fotovoltaik özellikleri ölçüldü. PCE açısından en iyi cihaz performansları P1 için %2.06 , P1-Br için % 1.52, P1-SH için %1,22 bulundu. P1-SH:AuNP'lerin fotovoltaik çalışmaları araştırılmış ve PCE açısından en iyi cihaz performansları % 1.08 olarak bulunmuştur.

Anahtar Kelimeler: Konjuge Polimerler, Altın Nanopartiküller, Benzothiadiazole, Güç Dönüştürme Verimliliği

To my family….

ACKNOWLEDGMENTS

I would like to thank Prof. Dr. Ali Çırpan for his wisdom and unending support, as well as for making me feel like I can always knock on his door while living away from my family. He is not only my supervisor but also a part of my family. He's always been patient and kind with me.

I would like to Dr. Bülend Ortaç and Ortaç Group Members for the synthesis and characterization of Au-NPs.

I would like to thank Duygu Keleş Cevher for her help in electrochemical and optical characterizations and also for sharing her knowledge.

I would like to thank Mertcan Erer and Eda Alemdar Yılmaz for their help in photovoltaic characterizations.

I would like to express my gratitude to Sultan Taşkaya Aslan and Şevki Can Cevher. They always help me with their valuable advice.

I would like to thank Dilan Ece Dikbıyık for her help in the synthesis of the monomer unit of P1 and for endless support during my master's study.

A special thank goes to my lab-mate Oğuzhan Karakurt. He always helps and supports me on all issues. His presence gave me the courage and made the lengthy and grueling experiments enjoyable.

Last but not least, I would like to thank my dad İbrahim Gülmez, and my mother Arife Gülmez. I dedicated this thesis to them. Their trust and belief in me are precious to me. I am the luckiest person alive to have them. I owe them everything.

This study was supported by the Scientific and Technological Research Council of TURKEY (TUBITAK) with project number 118Z738.

TABLE OF CONTENTS

LIST OF TABLES

TABLES

LIST OF FIGURES

FIGURES

LIST OF ABBREVIATIONS

ABBREVIATIONS

CP	Conjugated Polymer
PV	Photovoltaic
OPV	Organic Photovoltaic
OSC	Organic Solar Cell
OLED	Organic Light Emitting Diode
OFET	Organic Field Effect Transistor
NP	Nanoparticle
HOMO	Highest Occupied Molecular Orbital
LUMO	Lowest Unoccupied Molecular Orbital
E_g	Band Gap
E_g^{op}	Optical Band Gap
E_g^{el}	Electronic Band Gap
CB	Conduction Band
VB	Valence Band
BHJ	Bulk Heterojunction
ITO	Indium Tin Oxide
Al	Aluminium
PEDOT:PSS	Poly(3,4-ethylenedioxythiophene)-Poly(styrenesulfonate)
LiF	Lithium Fluoride

HTL	Hole Transport Layer
ETL	Electron Transport Layer
PCBM	[6,6]-Phenyl-C_{71}-Butyric Acid Methyl Ester
D	Donor
A	Acceptor
SAM	Self-Assembled Monolayer
TLC	Thin Layer Chromatograpy
NMR	Nuclear Magnetic Resonance
TMS	Tetramethylsilane
TGA	Thermal Gravimetric Analysis
DSC	Differential Scanning Calorimeter
AFM	Atomic Force Microscopy
TEM	Transmission Electron Microscopy
SEM	Scanning Electron Microscopy
HRMS	High-Resolution Mass Spectrometer
GPC	Gel Permeation Chromatography
PDI	Polydispersity Index
M_n	Number Average Molecular Weight
M_w	Weight Average Molecular Weight
CV	Cyclic Voltammogram
CE	Counter Electrode
WE	Working Electrode

RE	Reference Electrode
SHE	Standard Hydrogen Electrode
ACN	Acetonitrile
$TBAPF_6$	Tetrabutylammonium hexafluorophosphate
UV-Vis	Ultraviolet-Visible
ICT	Internal Charge Transfer
J-V	Current Density vs Voltage
J_{SC}	Short Circuit Current Density
V_{OC}	Open Circuit Voltage
J_{max}	Maximum Current Density
P_{max}	Maximum Power
V_{max}	Maximum Voltage
P_{in}	Incident Power
FF	Fill Factor
o-DCB	*ortho*-Dichlorobenzene
PCE	Power Conversion Efficiency
$CHCl_3$	Chloroform
THF	Tetrahydrofuran
DMF	Dimethylformamide
DCM	Dichloromethane
EtOAc	Ethyl Acetate
NBS	N-Bromosuccinimide

LIST OF SYMBOLS

SYMBOLS

λ_{max}	maximum wavelength
J	coupling constant
η	power conversion efficiency
δ	chemical shift

CHAPTER 1

INTRODUCTION

1.1 Renewable Energy

According to International Energy Agency, renewable energy is the energy produced from natural processes that are continually renewed [1]. Renewables, such as solar, wind, hydro, biofuels, and others, are at the heart of the transition to a lower-carbon, more sustainable energy system. Increasing the amount of variable renewable energy (VRE) technologies in power systems, such as wind and solar photovoltaic, is critical for decarbonizing the power sector while meeting rising energy demand [2]. Electricity is tried to generate using all renewable energy sources. Furthermore, geothermal steam is directly used for heating and cooking. Biomass and solar energy are also utilized to heat buildings and water. Transportation fuels include ethanol and biodiesel. Renewables have developed quickly in recent years, owing to regulatory backing and significant cost reductions for solar photovoltaics and wind generation. With the rapid expansion of solar photovoltaics and wind in recent years, the energy industry remains the brightest place for renewables [3].

1.1.1 Solar Energy and Solar Technology

The sun is an unlimited supply of free energy (i.e., solar energy) for the Earth. Solar energy resources are abundant and widely available, and they may be exploited any place there is sunlight. The quantity of solar radiation, also known as insolation, that reaches the Earth's surface every hour is greater than the total energy utilized by all human activities in a year. A variety of elements, such as geographic location, time

of day, and weather conditions, all influence the quantity of energy that can be harvested for electrical production or heating [3].

A solar cell, also known as a photovoltaic cell, is a device that uses the photoelectric effect to convert sunlight into energy. This phenomenon happens in semiconductor materials, which have two energy bands, one of which allows the presence of electrons (valence band) and the other of which does not, i.e., the band is fully "empty" (conduction band) [4].

Moreover, photovoltaic technology harbored many advantages compared to traditional power-generating sources that use fossil fuels. Photovoltaic technology does not generate the major environmental issues that these sources do during generation, such as climate change, global warming, air pollution, acid rain, and something that. Another benefit of solar energy over fossil fuels is that it does not need to be harvested, processed, or transported to the generation site, which is located near the load. Furthermore, solar-generated power generates no greenhouse emissions [4].

Solar photovoltaics are the fastest increasing source of power. Roughly 139 GW of worldwide capacity was installed in 2020, bringing the total to around 760 GW and providing nearly 3% of the world's power [3].

Based on the raw material utilized and the level of commercial development, photovoltaic cell technologies are often classified into three generations. First-generation solar panels use mono and multi-crystalline silicon cells, whilst second-generation solar panels use thin films such as amorphous silicon or CdTe. Organic and tandem solar cells are examples of novel material solar cells of the third generation. Organic cells have shorter lives and lower efficiency than inorganic cells, but they have advantages in terms of flexibility and the potential for reduced production and installation costs [5]. In recent years, a monocrystalline silicon cell achieved a peak efficiency of 26.7 %, a multi-crystalline silicon cell achieved a peak efficiency of 23.3 %, a CdTe cell had a peak efficiency of 22.1 %, and an organic cell achieved a high efficiency of 18.2 % in the lab [6].

1.2 Conjugated Polymers

A polymer is described as a molecule with a high relative molecular mass whose structure consists mainly of many repetitions of units generated from molecules with a low relative molecular mass [7]. If the polymer chains are formed with monomers that allow the π molecular orbitals to delocalize, this type of macromolecule is known as a conjugated polymer. They are organic semiconductors exhibiting semiconducting behavior associated with delocalized molecular orbitals along the polymer chain [8]. Alan J. Heeger, Alan MacDiarmid, and Hideki Shirakawa reported in 1977 that oxidized iodine-doped polyacetylene had better conductivity than undoped polyacetylene. They were awarded the Nobel Prize in Chemistry in 2000 for this work "for the invention and development of conductive polymers" [9]. Although polyacetylene itself did not find practical uses, it piqued the interest of scientists and fuelled the conductive conjugated polymer field's fast expansion. In Figure 1.1, the structures of some prevalent examples of conjugated polymers are demonstrated. Currently, monomer units have chosen more complicated structures to obtain a narrow bandgap to enhance solubility, conjunction, and absorption of conjugated polymers.

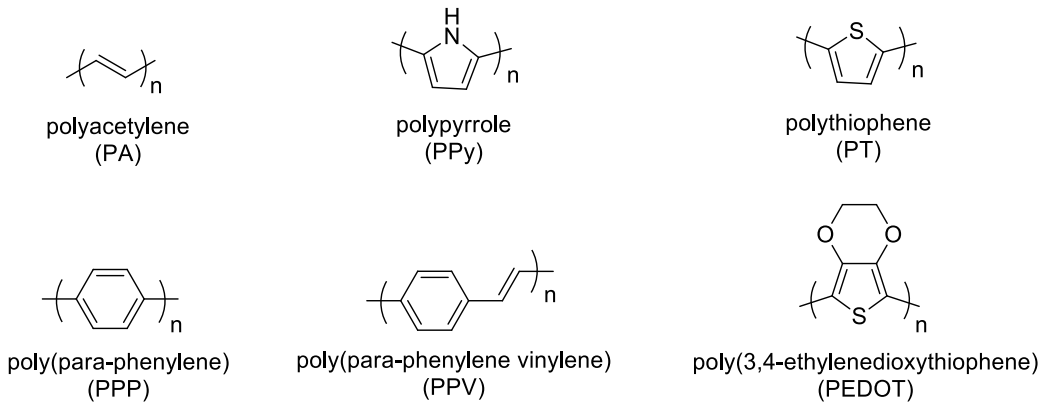

Figure 1.1. Common examples of conjugated polymers

Conjugated polymers are a more intriguing subject due to their low-cost production technique, appropriate stability, optical and electrochemical characteristics. Furthermore, they can be solution-processed to enable the production of flexible and

lightweight devices with broad application areas such as OLED (Organic Light Emitting Diode), OFET (Organic Field Effect Transistor), and OSC (Organic Semiconductor) [10].

1.2.1 Band Theory

Electron energy levels are divided into two groups: the 'valence band' and the 'conduction band.' The valence band has the highest occupied electron energy levels that confine π orbital, whereas the conduction band has the lowest unoccupied electron energy levels that confine π^* orbital. The energy difference between the top of the valence band and the bottom of the conduction band is named the 'bandgap (E_g) [11]. Moreover, the matters are divided into three groups according to their conductivity, which is affected by a bandgap, metal, insulator, and semiconductor, as demonstrated in Figure 1.2.

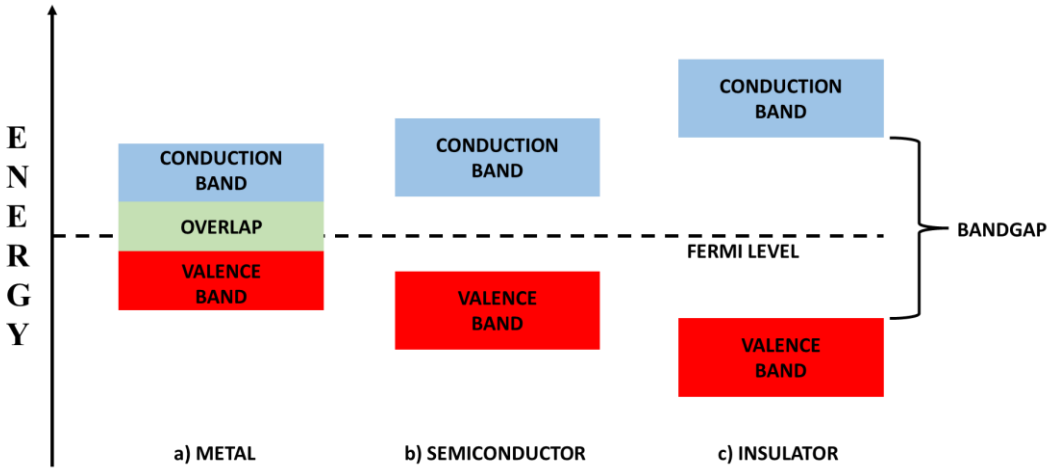

Figure 1.2. Illustration of band gap energies for a) metal, b) semiconductor and c) insulator

There is no bandgap in a conductor because the valence band is not entirely filled, enabling electrons to pass freely through the material. Insulators have huge band gaps (>4 eV) that need a lot of energy to bridge - as a result, electrons cannot travel from the valence band to the conduction band [12]. In semiconductors, on the other

hand, the bandgap is relatively small (<3 eV), allowing some electrons to shift to the conduction band by infusing modest amounts of energy [12]. In other terms, the bandgap is defined as the smallest amount of energy required to excite an electron from the valance band to the conduction band [13].

1.2.2 Donor-Acceptor Approach

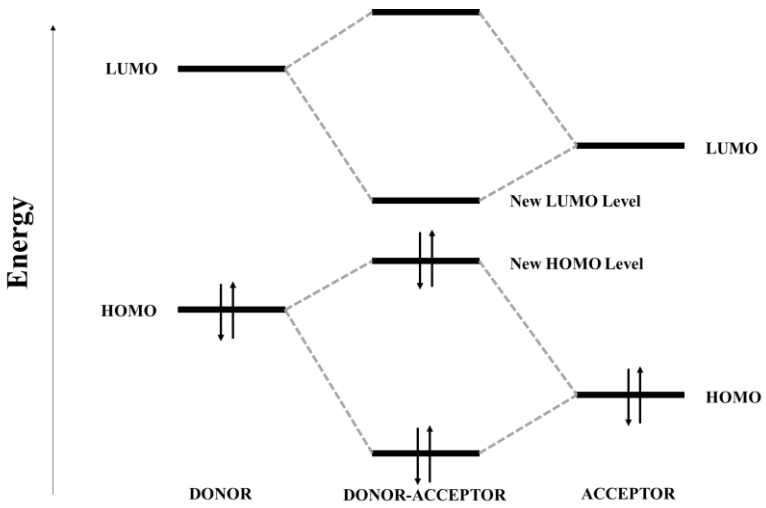

Figure 1.3. Generation of new HOMO-LUMO energy levels in donor-acceptor approach

Electrically conjugated polymers are designed using a molecular approach to provide minimal band gaps. In 1993, employing donor moieties that are electron-rich and acceptor moieties that are electron-deficient, Havinga and his colleagues developed a novel structural idea for the polymer backbone [14]. Interchain charge transfer between nearby molecules causes the band gap to decrease when electron donors with greater HOMO and electron acceptors with lower LUMO are combined. According to the new theory shown in Figure 1.3, the polymer lowest empty molecular orbital of polymer corresponds to the acceptor group's LUMO level and its highest occupied molecular orbital to the donor group's HOMO level [14]. It has been demonstrated that the D-A method gives conjugated systems additional optical

and electrical features, such as improved charge mobility and longer wavelength absorption, in addition to decreasing E_g [15].

1.2.3 Synthesis of Conjugated Polymers

Two different methodologies can be followed for the production of conjugated polymers on the basis of synthesis chemically and electrochemically. Chemically synthesis of conjugated polymers can also be divided into two polymerization methods, chemical oxidative polymerization and organometallic couplings. Moreover, the electrochemical oxidative polymerization method is used for the synthesis of conjugated polymers electrochemically [16].

Conjugated polymers synthesized by the organometallic coupling method can demonstrate proper structural characteristics that high molecular weight, low failure rate, and superior purity. Because the optical, electrical, and mechanical characteristics of conjugated polymers are substantially influenced by their molecular structure and material quality, the polycondensation process has been widely employed to create conjugated polymers with tailored architectures and well-defined capabilities [17].

1.2.3.1 Palladium Catalysed Cross-Coupling Polymerization Reactions

Transition metal-catalyzed polycondensation or palladium-catalyzed polymerization reactions include the reaction between a di-halogenated aryl monomer and another monomer in the presence of a catalytic amount of palladium catalyst. As a result of the reactions, a new carbon-carbon bond is constructed between monomers. The primary mechanism of palladium-catalyzed cross couplings is the production of metal-carbon bonds between two molecules. Carbon atoms coupled to palladium are therefore brought very near to one another. They then pair with one another, resulting in the production of a new carbon-carbon single bond [18]. Suzuki and Stille, Heck, Sonogashira, and Negishi cross-couplings are reactions used to design conjugated

polymers. In this study, polymers were synthesized via Suzuki and Stille cross-coupling reactions.

1.2.3.2 Suzuki Cross-Coupling Reaction

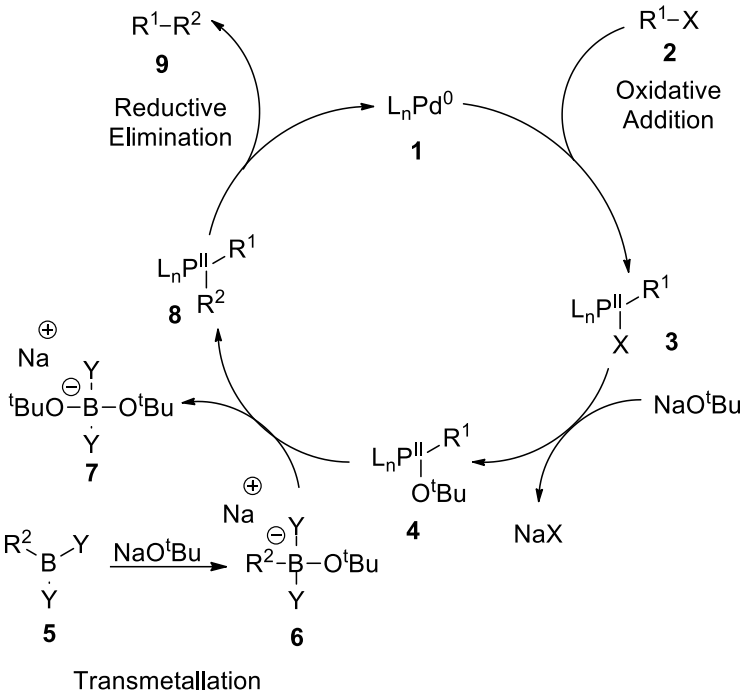

Figure 1.4. The general reaction mechanism of Suzuki cross-coupling reaction

The reaction between aryl or vinyl halide and aryl or vinyl boronic acid and also palladium (0) complex as a metal catalyst is called as Suzuki cross-coupling reaction. The mechanism of the reaction is shown in Figure 1.4. In the first step, the organopalladium derivative is produced via oxidative addition of palladium catalyst to the alkyl halide derivative. An intermediate specie is formed after the addition of a base. In the transmetallation step, this intermediate specie gives a reaction with the boron-ate complex, and another organopalladium derivative is formed. In the final step, the preferred product is obtained via reductive elimination of palladium [18].

1.2.3.3 Stille Cross-Coupling Reaction

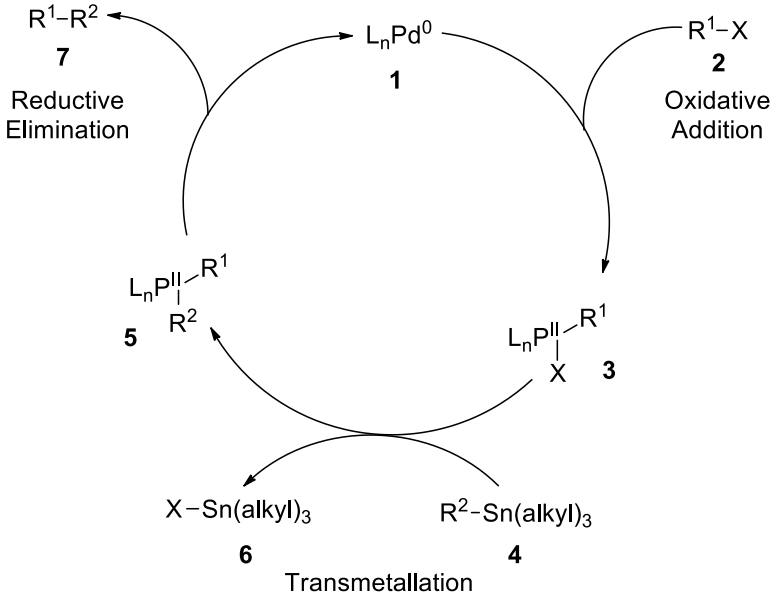

R1, R2 = ally, alkenyl, aryl ; X= Cl, Br, I, OTf, etc.
L= phosphine; alkyl= Me, Bu

Figure 1.5. The general reaction mechanism of Stille cross-coupling reaction

The reaction between aryl or alkenyl halide and organotin compound and also palladium (0) complex as a metal catalyst is called as Stille cross-coupling reaction. The mechanism of reaction is shown in Figure 1.5. The catalytic cycle including three steps is brought forward for Stille cross-coupling reaction. In the first step, the organopalladium derivative is produced via oxidative addition of palladium catalyst to the alkyl halide derivative. In the transmetallation step, this intermediate specie gives a reaction with organotin compound and another organopalladium derivative is formed. In the final step, the preferred product is obtained via reductive elimination of palladium [19].

1.3 Organic Solar Cells

As mentioned in Section 1.1., electricity can be obtained from sunlight by converting energy via solar cell devices. Though sunlight is eternal and free of charge, the manufacturing cost of electricity from solar cells is higher than the manufacturing cost of electricity from fossil fuel or nuclear power stations; because the solar cells are generally produced from inorganic materials and needed an uneconomic vacuum system. In addition, a high-temperature process is needed for them. To come through the financial problems of manufacturing conventional solar cells, organic materials which can absorb light have been put in solar cell devices due to their low-temperature potential and vacuum-free process instead of inorganic materials [20].

Alongside having a low-cost manufacturing process of organic photovoltaics, they demonstrate flexibility, semi-transparency, nominal environmental damage, low-weight, constant production process, workableness to new market areas, and short payback response [21].

Organic solar cells were first built as a single layer; however, there were some problems with getting high yields from single layer organic solar cell. The n-type or p-type organic material between the two electrodes was insufficient for charge generation for the single layer organic solar cells. In addition, the separation efficiency of the resulting charges was low. For this reason, the construction of double-layer solar cells was started. The bilayer type organic solar cells showed a dramatic increase in efficiency up to about 0.9% [20]. Although the use of both conjugated polymer and fullerene-derived structures as donor and acceptor layers in bilayer organic solar cells increased the efficiency of charge separation, there were still problems with delivering the charges to the electrodes. This has led to the emergence of bulk heterojunction organic solar cells by mixing conjugated polymers and fullerenes in an active layer. The idea of blending donor and acceptor was helped adjust diffusion length and the interfacial area of donor and acceptor. Thus, both the charge generation and charge separation problem improved. The detailed device

architecture and working principle of a bulk heterojunction organic solar cell is discussed in the following sections.

1.3.1 Device Architecture of BHJ Organic Solar Cells

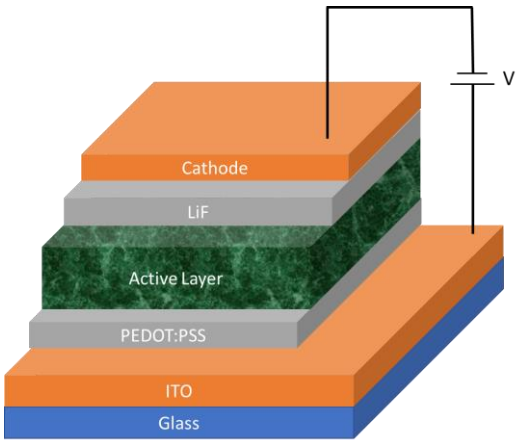

Figure 1.6. Device architecture of conventional bulk heterojunction OSCs

The device architecture of conventional bulk heterojunction solar cells is shown in Figure 1.6. Glass is used as a transparent substrate. The layers are sandwiched between electrodes. Indium Tin Oxide (ITO) that is coated on the glass substrate acts as an anode layer, and Al metal is generally used for the cathode layer. Electrodes are supported by the interfacial layers for the effective transportation of charges. The smoother ITO layer is provided by coating PEDOT:PSS onto the ITO layer. The work function of ITO is also reduced by PEDOT:PSS. In this way, hole transportation becomes easier. Therefore, PEDOT:PSS is known as the hole transport layer. On the other hand, LiF reduces the work function of the cathode and helps electron transportation between the LUMO of PCBM and Al by decreasing the energy barrier. Finally, in the middle of the device, there is an active layer containing a Polymer: PCBM blend at different concentrations. As mentioned before, mixing conjugated polymers and PCBM, which is a fullerene derivative, allowed the birth of bulk heterojunction organic solar cells. The prime movers of this idea are Heeger and Sarıçiftçi. In 1992, these two scientists proved that photoinduced charge transfer

takes place in the active layer of bulk heterojunction organic solar cells between the donor and acceptor groups very fast [22]. Conjugated polymers or small molecules have electron rich structures compared to fullerene derivatives, so they act as donors, while fullerene derivatives, which have the ability to accept six electrons, act as acceptors. The working principle of the BHJ organic solar cells is mentioned in the following section.

1.3.2 Working Principle of BHJ Organic Solar Cells

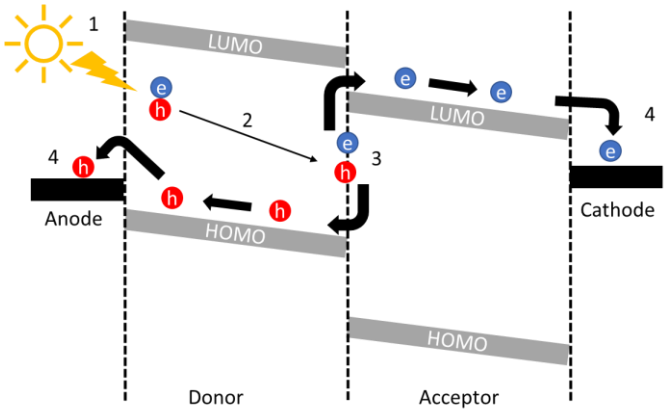

Figure 1.7. Schematic representation of working principle of OSCs

The working principle of an organic solar cell could be explained basically in four processes, as illustrated in Figure 1.7. First, light is absorbed by photoactive material in the active layer. When light is absorbed, electrons are excited to a higher energy level (LUMO), leaving holes in the lower energy level (HOMO), yet the electrons and holes are still constrained by coulombic interactions [23]. Electron and hole pairs, called excitons, form this way. Secondly, excitons diffuse the donor-acceptor interface. At that point, diffusion length is essential to prevent the recombination of electrons and holes. It should be approximately 5-20 nm [24].

Moreover, for excitons to be separated into free charges, a driving force is needed to overcome the coulombic effect between electrons and holes. After the diffusion of excitons, they separate from each other. However, if the exciton binding energy is

higher than the difference between the HOMO-LUMO band gap of D-A, charge separation will not happen. This is the crucial point for charge separation. After those free charges collect on the corresponding electrodes with the help of interfacial layers. The electrodes work function is also an essential parameter for this process. The HOMO energy level of donor moiety should be lower than the work function of the anode material and also the LUMO level of the acceptor material should be higher than work function of cathode for the effective charge collection [23]. Finally, the collection of charges at corresponding electrodes causes electricity production.

1.3.3 Characterization and Parameters of Organic Solar Cells

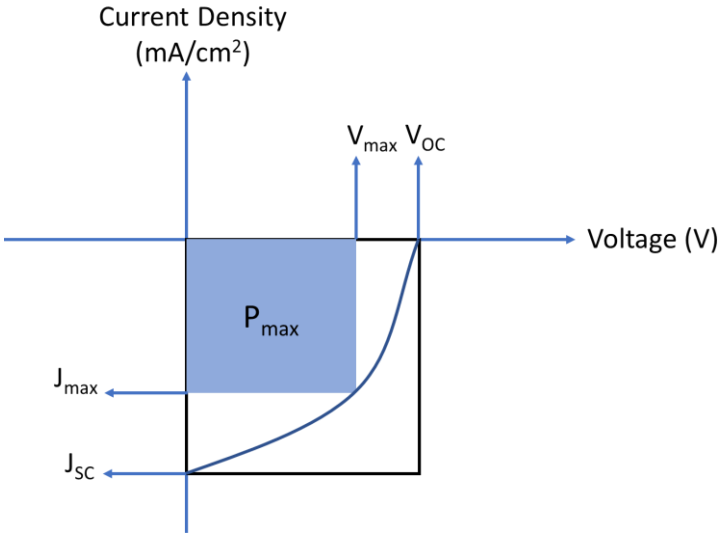

Figure 1.8. Illustration of a sample J-V curve

Power conversion efficiency (PCE) is essentially the ratio of the highest amount of power produced by the solar cell to the entire amount of power that the solar spectrum has applied to the object. In order to define this parameter as the maximum efficiency of a solar cell. However, several more factors relating to the performance of a solar cell need to be described in order to completely comprehend the idea of PCE. Following current-voltage evaluation of a solar cell under AM1.5G light, the

PCE of a solar cell is determined [25]. An example current density-voltage (J-V) curve is shown in Figure 1.8, together with all the parameters.

$$FF = \frac{J_{max} V_{max}}{J_{SC} V_{OC}} \qquad and \qquad PCE = \frac{P_{max}}{P_{in}} = \frac{J_{SC} V_{OC} FF}{P_{in}}$$

Essentially, open circuit voltage (V_{OC}) is the voltage measured when the system is not receiving any current. Typically, the difference in the work functions of electrodes is used to calculate V_{OC}. However, for the more recently created OSC designs, the active layer primarily increases the V_{OC} levels toward the interfacial layers employed in the device architecture. As previously stated, in order to obtain a tight band gap for conjugated polymers in OSCs, HOMO levels should not be overly elevated in order to minimize losses from V_{OC}. Another way to raise V_{OC} for OSCs is to use non-fullerene acceptors with adjustable LUMO values [26,27].

When there is no external voltage connected to a solar cell, the current density is said to be measured as a short circuit current density (J_{SC}). Because it is the current value measured for the area of the solar device, it is known as current density rather than short circuit current. J_{SC} value for an OSC is mostly correlated with active layer absorption.

The parameter known as the fill factor (FF) establishes the range of performance that a solar cell may achieve. In a perfect scenario, FF's value would be 1. J_{max} and V_{max}, which are less than ideal values, are what define the solar cell's maximum power output, nevertheless. Apart from the active layer's absorption, all J_{SC}-affecting factors also have an impact on FF values. The efficient D-A phase separation at the active layer, together with an interpenetrated bicontinuous shape and optimal domain sizes, are the primary determinants of FF value. As a result, the active layer morphology has a significant impact on FF [28,29].

1.4 Metallic Nanoparticles

Noble metal nanoparticles (NPs) have been widely used in a variety of applications due to their distinctive optical characteristics that result from their interactions with an incoming light [30]. Numerous characteristics of noble metal NPs make them desirable for a variety of applications in healthcare, energy, and information technology [30]. The surface plasmon resonance is produced when these metallic nanostructures interact with an incoming light and a dominating collective oscillation of free electrons, known as a plasmon, takes over [31].

The interaction between electromagnetic fields and free electrons in metals is known as surface plasmon resonance (SPR). Electrical aspects of light may excite free electrons in metals to create collective oscillations. These electron oscillations produce two modes. One such phenomenon is the surface plasmon-polariton (SPP), which is capable of propagating through metal/dielectric contacts. The second is called localized surface plasmon resonance (LSPR), and it is restricted to a very tiny volume surrounding a solitary nanoparticle or nanostructure [32]. The surface plasmon resonance, which involves a high number of these electrons, results in substantial absorption, scattering, and near-field amplification of plasmonic-metal nanoparticles at their native frequency [31].

For collecting and converting solar energy for use in a variety of applications, several methods, including photothermal, photovoltaic, and photochemical approaches, have been developed. The lack of light absorption and conversion efficiency is one of the key obstacles to the widespread implementation of these established technologies; nevertheless, using metallic NPs in energy conversion devices has shown promise for enhancing the results of these approaches [33].

1.4.1 Effect of Gold Nanoparticle Addition on Solar Cell

One of the best examples of a solar power system that produces electricity straight from the sun is a photovoltaic system. At fact, the photovoltaic effect produces

electron-hole pairs in the junction by absorbing light, converting solar energy to electricity. It is possible to increase light absorption and prevent electron-hole pair recombination throughout the process, but these two strategies compete with one another since one calls for a thick absorption layer and the other a thin one [30]. To solve this issue, plasmonic NPs can be used to increase the efficiency of solar cells by making use of their distinctive optical features, large scattering cross sections, field enhancements at the particle surfaces, and carrier production in the substrate [34].

One of the key obstacles to achieving EQEs and PCEs in solar cell devices continues to be the efficiency with which incoming light is absorbed. The ideal active layer thickness for an OPV device is often in the range of 100–200 nm, or even less; a layer this thin can result in poor light absorption [35]. Therefore, one strategy for more effective light absorption is to increase the thickness of active layer [36]. However, because organic materials have poor carrier mobilities and short exciton diffusion lengths, a thicker layer unavoidably raises the device resistance [37].

The photovoltaic absorber layers may be physically thinned out while maintaining the same optical thickness using plasmonic structures. First, by folding the light into a thin absorber layer, metallic nanoparticles may be utilized as subwavelength scattering components to link and trap freely propagating solar plane waves into an absorbent semiconductor thin film. Second, metallic nanoparticles can be utilized as subwavelength antennas, boosting the effective absorption cross-section of semiconductors by coupling the plasmonic near-field to it [33].

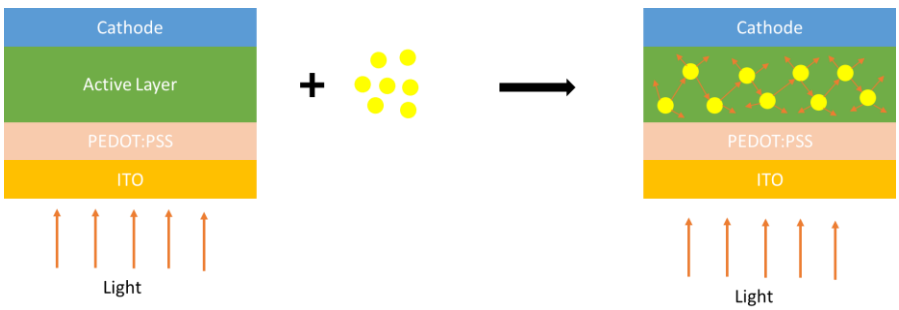

Figure 1.9. Representation of Au-NPs insertion to OSC device

Moreover, the dispersion of NPs into the photoactive layer also improves the structural integrity of the layer, which results in a slower rate of device deterioration under sustained illumination, according to current research efforts [38].

1.4.2 Gold Nanoparticle-Thiol Interaction

A crucial field for molecular electronics and biotechnology applications is the self-assembly of organic molecules onto metal surfaces and nanoparticles via thiol groups [39,40]. Thiols have a strong affinity for gold surfaces, which allows for the creation of well-defined organic surfaces with valuable and highly modifiable chemical functions exposed at the interface [41]. On the surfaces of recently evaporated gold films, long-chain alkanethiols ($HS(CH2)_nX$) adsorb from solutions and form oriented monolayers. These adsorptions may hold both polar and nonpolar tail groups (X). Self-assembled monolayers (SAMs), produced by adsorption on a metal, have similar wetting characteristics [42].

In addition, Kokkin and his colleagues reported that the ground state's bond length and dissociation energy are calculated to be 2.156 Å and 298 ±2 kJ/mol, respectively [43]. Binding interaction between Au-S, that based on the literature information helps regulates the distribution of Au-NPs on the active layer for organic photovoltaics.

1.5 Literature Review

Many studies in the literature support the idea behind this study. The literature research focuses on the fact that the efficiency of organic solar cells constructed from conjugated polymers with relatively high-power conversion efficiency can reach a higher efficiency by adding spherical metallic particles to the devices.

In this study, five different polymers were synthesized to be used as donor groups for devices. An analog of the P1 polymer with a different alkyl chain length has already been synthesized in the literature. Although it has been synthesized before, polymers (P1-Br and P1-SH) that have the potential to increase the power conversion efficiency by increasing the interaction with metallic particles with modifications to the end of the alkyl chain are promising. Figure 1.10 shows the structures of P1, pCzS, and PCDTBT-8, and Table 1.1. shows the device performances of similar polymers. The remaining two polymers are new to the literature. Although there are conjugated polymers synthesized using the same donor group, dithienopyrrolobenzothiadiazole derivative, in the literature, there is no example synthesized with the acceptor group used in this study.

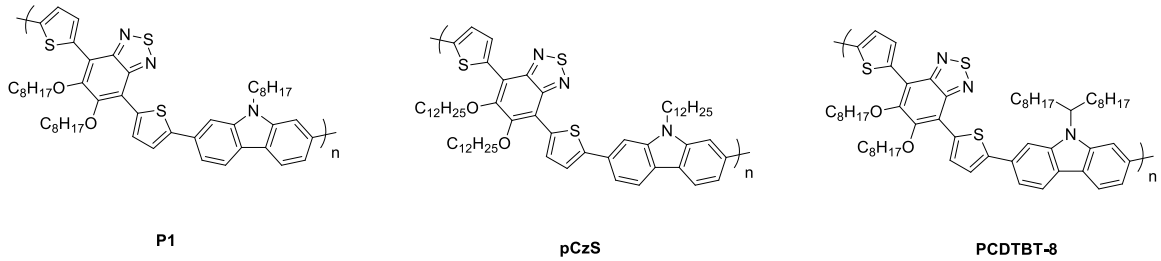

Figure 1.10. Structures of P1, pCzS and PCDTBT-8

Table 1.1. Photovoltaic parameters of pCzS:PCBM and PCDTBT-8:PCBM devices

Polymer	P:PCBM Ratio	Solvent	V_{OC}	J_{SC}	FF(%)	PCE(%)	Reference
pCzS	1:2	o-DCB	0.83	6.66	59.3	3.28	[44]
PCDTBT-8	1:4	CB	0.96	9.39	48.90	4.41	[45]

In the literature, there are studies on the effects of the distribution of particles in the active layer and at the interfaces on the performance of organic solar cells. Its distribution in the active layer is emphasized in this section. Stratakis and Kymakis published a review paper titled "Nano-particle-based plasmonic organic photovoltaic systems" in 2013 to provide a summary of their literature review on the effect of

metallic NPs on solar cell efficiency [46]. Table 1.2. was created using data from this review.

Table 1.2. Literature examples of device characterization of OPVs with NPs dispersed into the active layer

Geometry	Photoactive Layer	Η (%)	± (%)*	Mechanism	References
70 nm Ag NPs	PCDTBT:$PC_{70}BM$	7.1	13	Scattering	[47]
4.2–6.4 nm Au NPs	P3OT-C_{60}	1.65	50	Electrical	[48]
3.7 nm Au NPs	P3HT:PCBM	1.5	-67	Exciton Quenching	[49]
Ag NPs	P3HT:PCBM	3.56	8	LSPR Scattering	[50]
5–15 nm Ag NPs	P3HT:PCBM	3.3	-3	Monomolecular recombination	[51]
1.5–20 nm Au NPs	P3HT:PCBM	3.71	41	LSPR Scattering Morphology	[52]

± (%)* = percent change in Η

The numerous processes may occur according to Table 1.2. It is evident that some types of mechanisms result in poor efficiency, even though NPs dispersion in the photoactive layer normally results in a mechanism that increases efficiency. Potential options to modify the mechanism include NPs' size, shape, and type of nanoparticle. Additionally, the acceptor and donor units' structures might be important. As a result, the significance of the size, shape, and technique used to synthesize NPs emerges as a key component of the functioning mechanism.

1.6 Aim of the Study

Recently, literature researches have been continuing on the increase of power conversion efficiency with the addition of metallic particles to the active layer of organic solar cells. Strategies are applied to increase efficiency by taking advantage of the light trapping and light scattering properties of spherical metallic nanoparticles. In addition, an electron-rich donor monomer and an electron-deficient acceptor monomer are polymerized along the conjugated polymer backbone to create a low band gap polymer, which is a common method of making them. Along with the D-A approach, forcing planarization in the polymer backbone by covalently attaching neighboring aromatic units offers a successful method to close the band gap and improve charge carrier ability. The design and synthesis of coplanar multifused aromatic or heteroaromatic structures have received a lot of attention in this respect [53].

2,1,3-Benzothiadiazole is regarded as one of the most traditional electron-deficient acceptor units utilized in OSCs because of its planar and solid structure [54]. Additionally, the π-bridge is crucial in organic solar cells. The range of absorption is increased, the HOMO-LUMO levels are adjusted, and the donor and acceptor are connected . The shape of the π-bridge should be somewhat flat rather than deformed as it is the pathway that can aid electron migration from the donor to the acceptor [55]. An unfused structure is created by the benzothiadiazole unit partnering up with two thienyl rings acting as a π-bridge. This is why this study also employed a more planar dithienopyrrolobenzothiadiazole derivative acceptor.

In this thesis, the effect of the interaction of metallic nanoparticles with synthesized thiol group-containing polymers on the power conversion efficiency of organic solar cells was investigated, as well as the link between the chemical structure of solar cell devices and their photovoltaic performance. Five polymers were synthesized via Stille and Suzuki cross coupling reactions, and the spherical gold nanoparticles were also synthesized with the laser ablation technique. The first polymer (P1), that is already present in the literature with different alkyl chains combinations, was

synthesized according to the TUBITAK project to compare the difference in the photovoltaic performance of the solar cell devices of P1-Br and P1-SH when interacted with gold nanaparticle. Synthesized conjugated polymers P2 and P3, according to literature research, are new in the literature and their photovoltaic performances are aimed to investigate in this study.

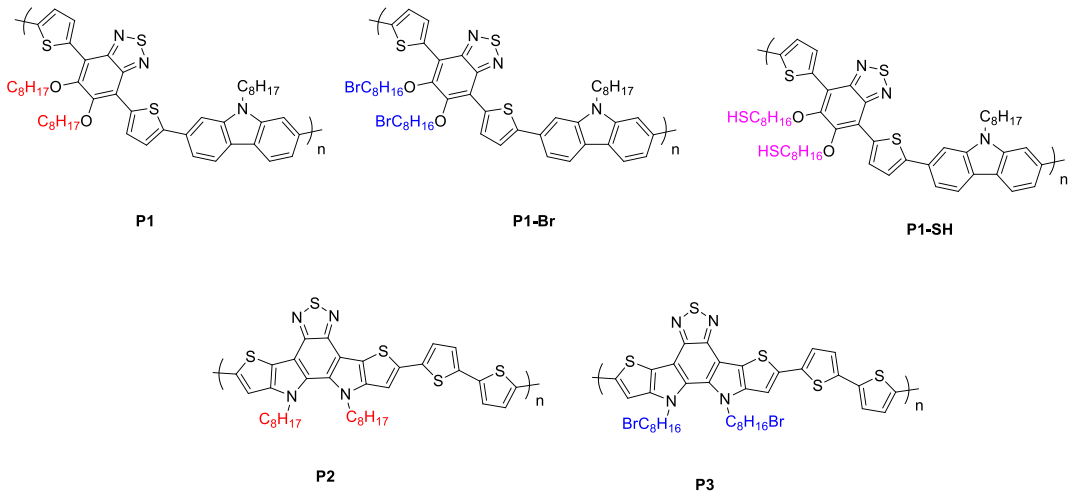

Figure 1.11. Chemical structures of target polymers

CHAPTER 2

EXPERIMENTAL

2.1 Materials and Equipment

All chemicals used for the monomer and polymer synthesis were ensured from Sigma Aldrich Chemical and Tokyo Chemical Industry (TCI). Air and moisture-sensitive reactions were fulfilled under a nitrogen atmosphere. Dry acetonitrile (ACN), toluene, tetrahydrofuran (THF), dichloromethane (DCM), and chloroform that received from Mbraun MBSPS5 solvent drying system were used for the reactions. Triethylamine was used freshly distilled by using calcium hydride as a drying agent. Molecular sieves, which have 4 Å size, were left in solvents to capture water and humidity, and solvents had degassed by nitrogen for one day for polymerization reactions. The purification processes of synthesized materials were carried out in column chromatography with Merck Silica Gel 60 as a stationary phase. In addition, thin layer chromatography with silica gel plates (0.25 mm) which is commercially available, was performed.

The structural characterization of compounds was materialized with Bruker Spectrospin Avance DPX-400 MHz spectrometer for both ^{1}H and ^{13}C NMR spectra. The internal standard of the system was tetramethylsilane (TMS), and samples were prepared in deuterated solvents.

HRMS, high-resolution mass spectroscopy, was used for the determination of the exact molecular weight of novel molecules. (Water Synapt MS System.)

Gel permeation chromatography (Shimadzu-20A) with polystyrene internal standard was used to indicate the molecular weight distribution of synthesized polymers. All solutions were prepared in chloroform solvent.

Thermal analyses of the polymers were detected by using a thermogravimetric analyzer (Pyris 1 TGA) and differential scanning calorimeter (Perkin Elmer Diamond DSC).

Energy levels and electronic band gaps were determined by cyclic voltammogram (CV) by using Gamry 600 Potentiostat with a constant scan rate of 100 mV/s. Optical properties were determined by UV-Vis spectroscopy technique with Varian Carry 5000 model spectrometer.

Finally, photovoltaic studies were carried out the Keithley 2400 instrument to obtain current and voltage measurements under 1.5 G illumination and 100 mW cm^{-2} photocurrent.

2.2 Synthesis of Monomers

2.2.1 Synthesis of 1,2-dimethoxy-4,5-dinitrobenzene

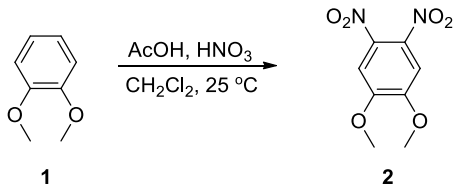

Figure 2.1. Synthetic route of compound 2

10 g (72.38mmol) veratrole (1) and 9.5 mL acetic acid were added to the two-necked 250 mL round-bottom reaction flask. 40 mL DCM was added to dissolve, and they stirred. The reaction temperature was decreased to 0 °C with an ice bath. After the temperature reached 0 °C, 27 mL fuming HNO_3 was added dropwise. The temperature of the reaction was allowed to rise to room temperature. Then, the reaction was stirred for 24 hr. The mixture was poured into the ice to precipitate the

resultant product. The yellow precipitate was filtered and washed with cold water several times to eliminate excess acid. The product was recrystallized with ethanol (EtOH), and yellow crystals were obtained (14.8 g, 90% yield).

^{1}H NMR (400 MHz, $CDCl_3$) δ 7.32 (s, 2H), 4.00 (s, 6H).

^{13}C NMR (100 MHz, $CDCl_3$) δ 151.9, 136.7, 107.0, 57.1

2.2.2 Synthesis of 4,5-dimethoxybenzene-1,2-diamine

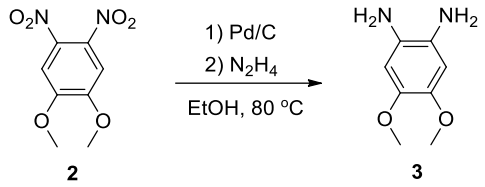

Figure 2.2. Synthetic route of compound 3

1,2-Dimethoxy-4,5-dinitrobenzene (3g, 13.15 mmol) and Pd/C catalyst (0.42 g, 3.94 mmol) were added to the two-necked 250 mL round bottom flask and dissolved in 50 mL EtOH. The temperature was raised to 50 °C. Then, hydrazine monohydrate (4.21 g, 131.49 mmol) was added drop by drop. The reaction was refluxed for 6 hr at 80 °C. After the reaction temperature was cooled down to room temperature, the reaction mixture was passed through the Celite to filter Pd/C and washed with hot ethanol. The solvent was removed from the filtrate under reduced pressure, and the tattletale grey solid was obtained. The product was used in the next step right away without further purification because of the decomposition issue in time.

2.2.3 Synthesis of 5,6-dimethoxybenzo[*c*][1,2,5]thiadiazole

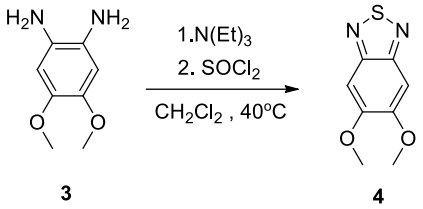

Figure 2.3. Synthetic route of compound 4

4,5-Dimethoxybenzene-1,2-diamine (1.5 g, 6.22 mmol) was dissolved in 80 mL dry DCM in two-necked 250 mL round-bottom flask. Freshly distilled triethylamine (8,67 mL, 62.26 mmol) was added to the mixture. The solution of thionyl chloride was added drop by drop to the mixture in an ice bath after thionyl chloride (1 mL, 13.7 mmol) was diluted in 10 mL dry DCM. The mixture was stirred and refluxed for 6 hr at 40 °C, and then the solution was cooled to room temperature. The reaction solvent was evaporated under reduced pressure. Then the residual solid was washed with water several times and filtered. The filtrate was recrystallized in ethanol, and sand-colored crystals were obtained (0.61 g, 50% yield).

^{1}H NMR (400 MHz, $CDCl_3$) δ 7.14 (s, 2H), 3.97 (s, 6H)

^{13}C NMR (100 MHz, $CDCl_3$) δ 154.2, 151.3, 98.0, 56.3

2.2.4 Synthesis of benzo[*c*][1,2,5]thiadiazole-5,6-diol

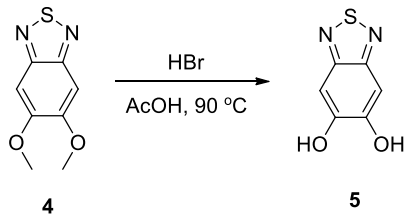

Figure 2.4. Synthetic route of compound 5

5,6-Dimethoxybenzo[*c*][1,2,5]thiadiazole (0.50 g, 2.55 mmol), 5 mL acetic acid and 15 mL of hydrobromic acid (48%) were added to the 100 mL round-bottom flask

and stirred at 90 °C for 2 days. The dirty yellow solid was precipitated in the mixture after two days. The reaction temperature was cooled down, and the resulting solid was filtered. After that, the filtrate was washed with water several times to eliminate excess acid (0.32 g, 75% yield).

^{1}H NMR (400 MHz, DMSO) δ 10.58 (s, 2H), 7.12 (s, 2H).

^{13}C NMR (100 MHz, DMSO) δ 152.6, 151.2, 100.0.

2.2.5 Synthesis of 5,6-bis((8-bromooctyl)oxy)benzo[*c*][1,2,5]thiadiazole

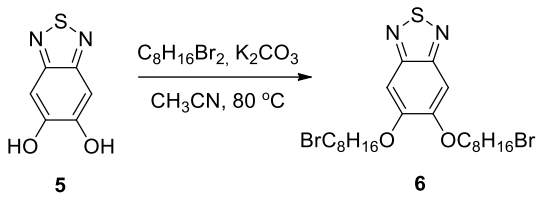

Figure 2.5. Synthetic route of compound 6

Benzo[*c*][1,2,5]thiadiazole-5,6-diol (0.58 g, 3.45 mmol) and potassium carbonate (1.9 g, 13.8 mmol) were added to the two-necked 100 mL round-bottom flask. The mixture was vacuumed and gassed with nitrogen several times. Then, 50 mL dry acetonitrile was added, and the temperature was increased up to 80 °C. After the reaction mixture was stirred for 1 hour at that temperature, 1,8-dibromooctane (7.60 g, 27.60 mmol) was added to the reaction. The reaction was continued to stir for two days. After the reaction was finished with TLC control, the reaction solvent was eliminated under reduced pressure, and the crude product was extracted with DCM and brine a few times. The organic phase was separated and dried with magnesium sulfate. After that, the organic phase was evaporated under reduced pressure. The product was precipitated with cold hexane and washed several times. The white product was filtered (0.30 g, 16% yield).

^{1}H NMR (400 MHz, $CDCl_3$) δ 7.15 (s, 2H), 4.11 (t, J = 6.5 Hz, 4H), 3.43 (t, J = 6.8 Hz, 4H), 1.97 – 1.84 (m, 8H), 1.58 – 1.37 (m, 16H).

^{13}C NMR (100 MHz, $CDCl_3$) δ 153.9, 151.2, 98.3, 68.9, 33.8, 32.7, 29.0, 28.6, 28.6, 28.0, 25.8.

2.2.6 Synthesis of 4,7-dibromo-5,6-bis((8-bromooctyl)oxy) benzo[*c*][1,2,5] thiadiazole

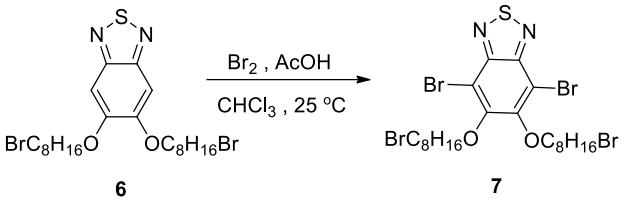

Figure 2.6. Synthetic route of compound 7

Compound 6 (0.30 g, 0.5 mmol) and 10 mL acetic acid were added to the two-necked 100 mL round-bottom flask. Then, the compound was dissolved in 30 mL chloroform. The reaction was stirred at room temperature for 30 min. After that, bromine (0.1 mL, 2.2 mmol) was diluted in 5 mL acetic acid, and the bromine solution was added dropwise into the reaction. Then, the reaction mixture was stirred for three days at room temperature. The reaction was finished with TLC control and extracted with sodium metabisulfite solution ($Na_2S_2O_5$) and chloroform to eliminate excess bromine. The organic phase was collected and dried with magnesium sulfate. Then, the solution was filtered, and chloroform was evaporated under reduced pressure. The yellowish-white crude product was purified with silica gel column chromatography (3:1 hexane-chloroform), and a white solid was obtained (0.3 g, 78% yield).

^{1}H NMR (400 MHz, $CDCl_3$) δ 4.15 (t, J = 6.5 Hz, 4H), 3.42 (t, *J* = 6.8 Hz, 4H), 1.92 – 1.82 (m, 8H), 1.57 – 1.34 (m, 16H).

^{13}C NMR (100 MHz, $CDCl_3$) δ 154.3, 150.2, 106.2, 74.9, 33.9, 32.6, 30.1, 29.1, 28.6, 28.0, 25.8.

2.2.7 Synthesis of tributyl(thiophen-2-yl)stannane

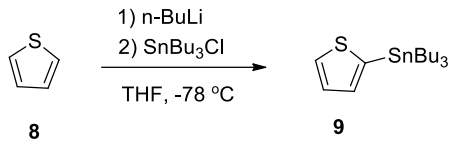

Figure 2.7. Synthetic route of compound 9

Thiophene (2 g, 23.8 mmol) was placed in a 100 mL schlenk tube, and 25 mL dry THF was added to dissolve thiophene. The solution was stirred under a nitrogen atmosphere, and the reaction temperature was decreased to -78 °C. Then, n-butyllithium (2.5 M in hexane) (10.5 mL, 26.2 mmol) was added to the reaction dropwise in 45 min. The reaction was continued to stir for 1 hour at -78 °C. At the end of 1 hour, tributyl stannyl chloride ($SnBu_3Cl$) (7.1 mL, 26.2 mmol) was added slowly. The mixture was stirred overnight at room temperature. After that, the reaction was quenched with distilled water to eliminate excess n-butyllithium. The mixture was extracted with chloroform and brine. The organic phase was separated and dried with magnesium sulfate. After filtration, the mixture was concentrated with a rotary evaporator. A transparent light-yellow liquid was collected (8 g, 90% yield).

^{1}H NMR (400 MHz, CDCl3): δ 7.58 (d, J=4.7 Hz, 1H), 7.19 (t, J= 3.3 Hz, 1H), 7.12 (d, J= 3.2 Hz, 1H), 1.50 (m, J=7.8 Hz, 6H), 1.28 (m, J= 7.3 Hz, 6H), 1.03 (t, J= 8.4 Hz, 6H), 0.82 (t, J= 7.3 Hz, 9H).

2.2.8 Synthesis of 5,6-bis((8-bromooctyl)oxy)-4,7-di(thiophen-2-yl) benzo[*c*][1,2,5]thiadiazole

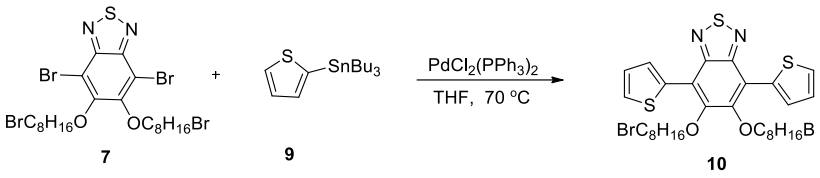

Figure 2.8. Synthetic route of compound 10

Compound 7 (0.73 g, 1.04 mmol) and compound 9 (0.86 g, 2.08 mmol) were placed in 100 mL schlenk tube. The tube was vacuumed and gassed three times with N_2 gas for 30 min. Then, 40 mL dry THF was added to dissolve the compounds, and bubbling was performed for 30 min under a nitrogen atmosphere. Then, $PdCl_2(PPh_3)_2$ (0.15 g, 0.21 mmol) was added fast to the reaction medium, and the temperature was increased up to 70 °C. The reaction was stirred for one day and finished by performing TLC control. THF was evaporated under reduced pressure. The crude product was purified by using silica gel column chromatography with hexane as a mobile phase. The polarity of the mobile phase was increased gradually (up to 3:1 hexane: chloroform). The orange solid was collected (0.55 g, 74% yield).

^{1}H NMR (400 MHz, $CDCl_3$) δ 8.49 (d, *J* = 3.8 Hz, 2H), 7.53 (d, *J* = 5.1 Hz, 2H), 7.27 (dd, *J* = 9.5, 4.5 Hz, 2H), 4.13 (t, *J* = 7.0 Hz, 4H), 3.44 (t, *J* = 6.8 Hz, 4H), 1.97 – 1.86 (m, 8H), 1.49 – 1.35 (m, 16H).

^{13}C NMR (100 MHz, $CDCl_3$) δ 151.77, 150.89, 133.95, 130.49, 127.25, 126.69, 117.55, 74.15, 33.88, 32.67, 30.15, 29.21, 28.62, 27.99, 25.74.

2.2.9 Synthesis of 5,6-bis((8-bromooctyl)oxy)-4,7-bis(5-bromothiophen-2-yl)benzo[*c*][1,2,5]thiadiazole

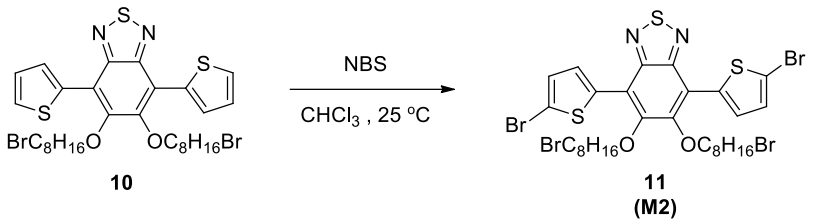

Figure 2.9. Synthetic route of compound 11

Compound 10 (0.36 g, 0.50 mmol) and 30 mL chloroform were added to the two-necked 100 mL round-bottom flask. While the reaction was stirred under a nitrogen atmosphere, NBS (0.20 g, 1.11 mmol), which dissolved in 10 mL chloroform, was added to the reaction drop by drop in 20 min in the dark. After the addition process was completed, the reaction was continued to stir for one hour. Then, the reaction was finished with TLC control. Extraction was performed with brine and chloroform. The organic phase was collected and dried with magnesium sulfate. Then, the mixture was filtered with filter paper, and the organic phase was concentrated under reduced pressure with a rotary evaporator. The crude product was purified using silica gel column chromatography with hexane as a mobile phase. The polarity of the mobile phase was increased gradually (up to 3:1 hexane: chloroform). The orange solid was collected (0.35 g, 80% yield).

^{1}H NMR (400 MHz, $CDCl_3$) δ 8.36 (d, *J* = 4.1 Hz, 2H), 7.17 (d, *J* = 4.1 Hz, 2H), 4.12 (t, *J* = 7.1 Hz, 4H), 3.42 (t, *J* = 6.8 Hz, 4H), 1.94 – 1.84 (m, 8H), 1.48 – 1.36 (m, 16H).

^{13}C NMR (100 MHz, $CDCl_3$) δ 151.2, 150.3, 135.5, 131.0, 129.6, 116.9, 115.4, 74.3, 33.9, 32.7, 30.1, 29.2, 28.6, 28.0, 25.7.

2.2.10 Synthesis of 4,7-dibromobenzo[*c*][1,2,5]thiadiazole

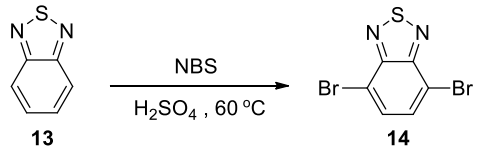

13 14

Figure 2.10. Synthetic route of compound 14

Thiadiazole (6 g, 44.1 mmol) and NBS (16.5 g, 92.5 mmol) were placed in a two-necked 100 mL round bottom flask and dissolved in 60 mL concentrated H_2SO_4 (97%). The temperature was increased to 60 °C, and the reaction was stirred overnight. Then, the reaction was finished with TLC control and poured into the ice. The solution was stirred until the ice was melted. After that, the precipitate was filtered and washed with cold water. The precipitate was recrystallized in EtOH, and white crystals were obtained (10 g, 77% yield).

^{1}H NMR (400 MHz, DMSO) δ 7.94 (s, 2H).

^{13}C NMR (100 MHz, DMSO) δ 152.3, 132.8, 113.1.

2.2.11 Synthesis of 4,7-dibromo-5,6-dinitrobenzo[*c*][1,2,5]thiadiazole

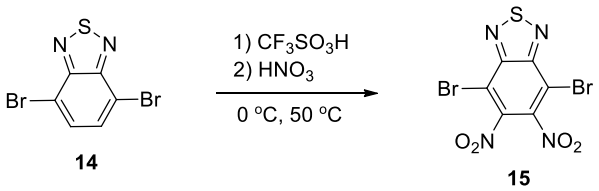

14 15

Figure 2.11. Synthetic route of compound 15

Fuming nitric acid (HNO_3) (3.41 mL, 81.6 mmol) was added dropwise at 0 °C to the fuming trifluoromethanesulfonic acid (CF_3SO_3H) (21.5 mL, 245.0 mmol), which was placed in a two-necked 100 mL round-bottom flask. A solid white complex was formed in the reaction medium. Then, 4,7-dibromobenzo[*c*][1,2,5]thiadiazole (6 g, 20.4 mmol) was added to the reaction medium portion by portion in 30 min. The

reaction temperature was increased to 50 °C and stirred overnight. After TLC control, the reaction was finished, and cold water was poured into the solution. NaOH solution was added to neutralize the reaction mixture. The pale-yellow precipitate was filtered and washed with cold water. Finally, the residue was recrystallized with EtOH, and pale-yellow crystals were obtained (6.65 g, 85% yield).

^{13}C NMR (100 MHz, DMSO) δ 151.9, 144.0, 111.7.

2.2.12 Synthesis of 5,6-dinitro-4,7-di(thiophen-2-yl)benzo[*c*][1,2,5] thiadiazole

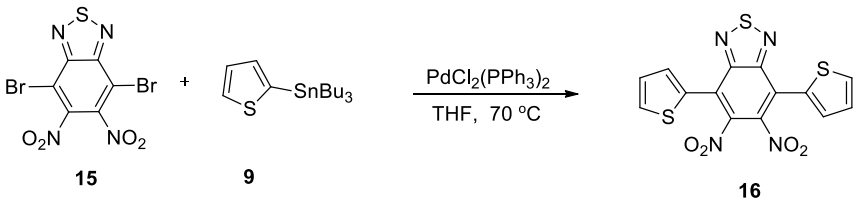

Figure 2.12. Synthetic route of compound 16

4,7-dibromo-5,6-dinitrobenzo[*c*][1,2,5]thiadiazole (3 g, 7.8 mmol) and 2-tributylstannyl thiophene (7.55 g, 17.2 mmol) were placed in 100 mL schlenk tube. The tube was vacuumed for a time and gassed with N_2 gas to eliminate humidity and oxygen in the reaction medium. This process was repeated several times. 50 mL dry THF was added to the schlenk tube to dissolve compounds, and the reaction mixture was bubbled with N_2 gases for 20 min. Then, $PdCl_2(PPh_3)_2$ (0.27 g, 0.39 mmol) was added. The reaction temperature was raised to 80 °C and stirred overnight. According to TLC control, the reaction was finished, and the reaction passed through the Celite to remove the catalyst. The collected mixture was concentrated under reduced pressure and precipitated in hexane several times. The precipitate was collected with filtering, and an orange solid was obtained (2.3 g, 73% yield).

^{1}H NMR (400 MHz, $CDCl_3$) δ 7.75 (dd, *J* = 5.1, 0.9 Hz, 2H), 7.52 (dd, *J* = 3.7, 1.0 Hz, 2H), 7.24 (dd, *J* = 5.0, 3.8 Hz, 2H).

^{13}C NMR (100 MHz, $CDCl_3$) δ 152.2, 141.9, 131.5, 131.0, 129.6, 128.1, 121.5.

2.2.13 Synthesis of 10,11-dihydro-[1,2,5]thiadiazolo[3,4-*e*]thieno[2',3':4,5] pyrrolo[3,2-*g*]thieno[3,2-*b*]indole

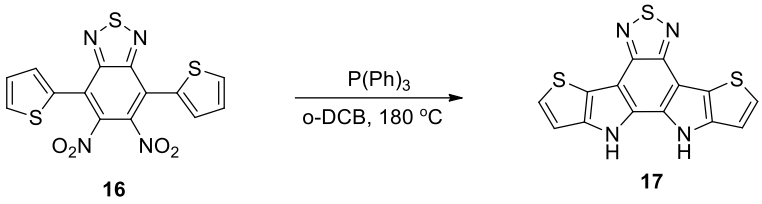

Figure 2.13. Synthetic route of compound 17

5,6-dinitro-4,7-di(thiophen-2-yl)benzo[c][1,2,5]thiadiazole (1.25 g, 3.20 mmol) and triphenylphosphine, PPh_3, (5.88 g, 22.41 mmol) were added 100 mL round bottom flask. The flask was vacuumed and gasses with N_2 gas several times to dry the reaction medium. Then, 20 mL *o*-DCB solvent that dried with bubbling for one day was added to dissolve compounds. The reaction temperature was increased to 180 °C, and the reaction refluxed overnight under a nitrogen atmosphere. The reaction was finished after TLC control and was cooled down. The reaction solvent was separated with silica gel column chromatography with hexane, and then the polarity of the mobile phase was increased (3:1 hexane: ethyl acetate). The collected solvent was evaporated under reduced pressure, and the dark-orange product was obtained (0.42 g, 40% yield).

^{1}H NMR (400 MHz, Acetone) δ 11.25 (s, 2H), 7.55 (d, J = 5.2 Hz, 2H), 7.32 (d, J = 5.2 Hz, 2H).

^{13}C NMR (100 MHz, Acetone) δ 147.4, 141.2, 129.6, 126.3, 119.8, 112.0, 107.6.

2.2.14 Synthesis of 10,11-dioctyl-10,11-dihydro-[1,2,5]thiadiazolo[3,4-*e*] thieno[2',3':4,5]pyrrolo[3,2-*g*]thieno[3,2-*b*]indole

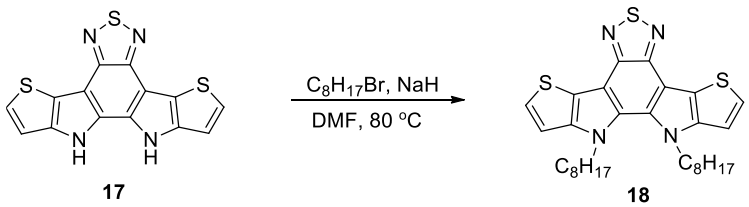

Figure 2.14. Synthetic route of compound 18

Compound 17 (0.40 g, 1.23 mmol), 1-bromooctane (1.5 g, 8.2 mmol) and NaH (60%, 0.34 g, 8.58 mmol) were added to 100 mL schlenk tube. The tube was vacuumed and gassed with N_2 gas several times. Then, 20 mL dry DMF was added to the schlenk tube. The reaction was stirred and refluxed one day under a nitrogen atmosphere at 80 °C. After TLC control, the reaction was finished, and the reaction solvent was evaporated with a rotary evaporator. Then, the crude product was extracted with DCM and brine three times. The organic phase was separated and dried with magnesium sulfate. After the filtration, the mixture was concentrated under reduced pressure and purified with silica gel column chromatography (5:1 hexane: ethyl acetate). Compound 18 was obtained (0.42 g, 62% yield).

^{1}H NMR (400 MHz, $CDCl_3$) δ 7.44 (d, *J* = 5.2 Hz, 2H), 7.19 (d, *J* = 5.2 Hz, 2H), 4.50 (d, *J* = 7.4 Hz, 4H), 1.87 – 1.78 (m, 4H), 1.20 – 1.09 (m, 20H), 0.80 (t, *J* = 7.0 Hz, 6H).

^{13}C NMR (100 MHz, $CDCl_3$) δ 147.6, 145.5, 132.2, 126.8, 121.2, 111.8, 110.9, 50.4, 31.6, 30.0, 29.0, 26.5, 22.5, 14.1.

2.2.15 Synthesis of 2,8-dibromo-10,11-dioctyl-10,11-dihydro-[1,2,5] thiadiazolo[3,4-*e*]thieno[2',3':4,5]pyrrolo[3,2-*g*]thieno[3,2-*b*]indole

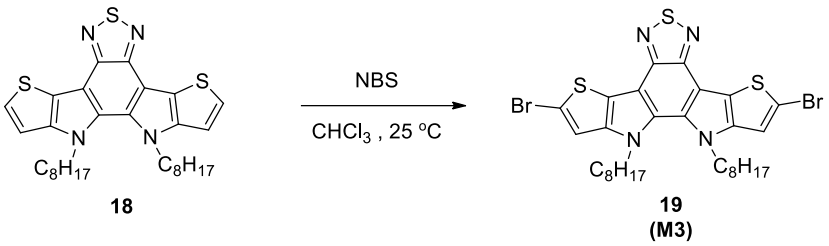

18 19 (M3)

Figure 2.15. Synthetic route of compound 19

Compound 18 (0.40 g, 0.73 mmol) and 30 mL chloroform were added to the two-necked 100 mL round-bottom flask. While the reaction was stirred under a nitrogen atmosphere, NBS (0.10 g, 1.6 mmol), which dissolved in 10 mL chloroform, was added to the reaction drop by drop in 20 min in the dark. After the addition process was completed, the reaction was continued to stir for one hour. Then, the reaction was finished with TLC control. Extraction was performed with brine and chloroform. The organic phase was collected and dried with magnesium sulfate. Then, the mixture was filtered with filter paper, and the organic phase was concentrated under reduced pressure with a rotary evaporator. The crude product was purified using silica gel column chromatography (3:1 hexane: ethyl acetate). The reddish-orange solid was collected (0.32 g, 62% yield).

^{1}H NMR (400 MHz, $CDCl_3$) δ 7.20 (s, *J* = 7.4 Hz, 2H), 4.41 (d, *J* = 7.3 Hz, 4H), 1.84 – 1.75 (m, 4H), 1.23 – 1.11 (m, 20H), 0.81 (t, *J* = 7.1 Hz, 6H).

^{13}C NMR (100 MHz, $CDCl_3$) δ 147.0, 143.0, 130.7, 121.1, 114.9, 113.4, 110.6, 50.2, 31.5, 29.9, 28.9, 28.8, 26.4, 22.4, 13.9.

2.2.16 Synthesis of 10,11-bis(8-bromooctyl)-10,11-dihydro-[1,2,5] thiadiazolo[3,4-*e*]thieno[2',3':4,5]pyrrolo[3,2-*g*]thieno[3,2-*b*]indole

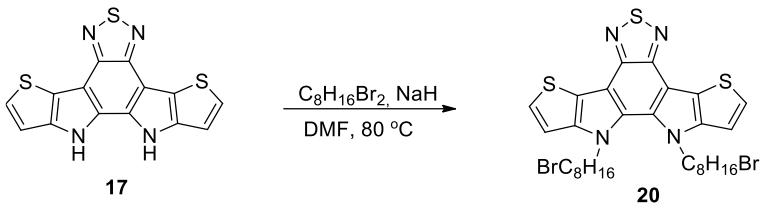

17 20

Figure 2.16. Synthetic route of compound 20

Compound 17 (0.30 g, 0.92 mmol), 1,8-bromooctane (2.5 g, 9.2 mmol) and NaH (60%, 0.26 g, 6.4 mmol) were added to 100 mL schlenk tube. The tube was vacuumed and gassed with N_2 gas several times. Then, 20 mL dry DMF was added to the schlenk tube. The reaction was stirred and refluxed one day under a nitrogen atmosphere at 80 °C. After TLC control, the reaction was finished, and the reaction solvent was evaporated with a rotary evaporator. Then, the crude product was extracted with DCM and brine three times. The organic phase was separated and dried with magnesium sulfate. After the filtration, the mixture was concentrated under reduced pressure and purified with silica gel column chromatography (5:1 hexane: ethyl acetate). Compound 20 was obtained (0.15 g, 23% yield).

^{1}H NMR (400 MHz, $CDCl_3$) δ 7.45 (d, *J* = 5.2 Hz, 2H), 7.20 (d, *J* = 5.2 Hz, 2H), 4.53 (t, *J* = 7.4 Hz, 4H), 3.31 (t, *J* = 6.8 Hz, 4H), 1.81 – 1.67 (m, 8H), 1.22 – 1.05 (m, 16H).

^{13}C NMR (100 MHz, $CDCl_3$) δ 147.6, 145.5, 132.3, 126.9, 121.3, 111.8, 111.0, 50.3, 33.9, 32.5, 29.8, 28.7, 28.4, 27.8, 26.3.

2.2.17 Synthesis of 2,8-dibromo-10,11-bis(8-bromooctyl)-10,11-dihydro-[1,2,5]thiadiazolo[3,4-*e*]thieno[2',3':4,5]pyrrolo[3,2-*g*]thieno[3,2-*b*]indole

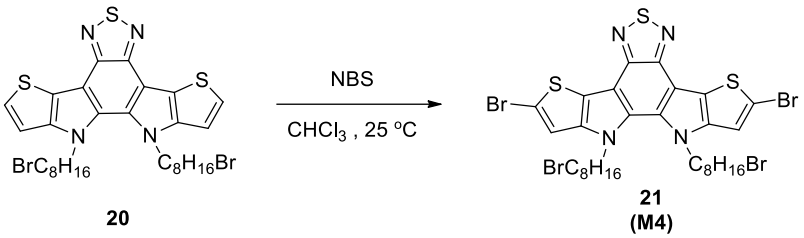

Figure 2.17. Synthetic route of compound 21

Compound 18 (0.15 g, 0.20 mmol) and 20 mL chloroform were added to the two-necked 100 mL round-bottom flask. While the reaction was stirred under a nitrogen atmosphere, NBS (0.27 g, 0.46 mmol), which dissolved in 10 mL chloroform, was added to the reaction drop by drop in 20 min in the dark. After the addition process was completed, the reaction was continued to stir for one hour. Then, the reaction was finished with TLC control. Extraction was performed with brine and chloroform. The organic phase was collected and dried with magnesium sulfate. Then, the mixture was filtered with filter paper, and the organic phase was concentrated under reduced pressure with a rotary evaporator. The crude product was purified using silica gel column chromatography (3:1 hexane: ethyl acetate). The reddish-orange solid was collected (0.13 g, 71% yield).

^{1}H NMR (400 MHz, $CDCl_3$) δ 7.20 (s, 2H), 4.42 (t, *J* = 7.4 Hz, 4H), 3.32 (t, *J* = 6.7 Hz, 4H), 1.81 – 1.68 (m, 8H), 1.28 – 1.01 (m, 16H).

^{13}C NMR (100 MHz, $CDCl_3$) δ 147.0, 143.1, 130.8, 121.2, 114.9, 113.6, 110.7, 50.20, 33.8, 32.4, 29.8, 28.6, 28.2, 27.7, 26.1.

2.3 Synthesis of Polymers

2.3.1 Synthesis of P1

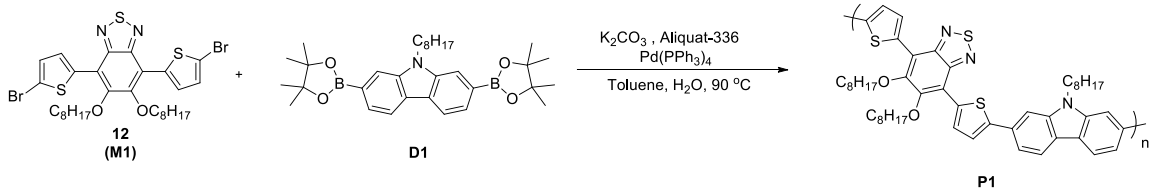

Figure 2.18. Synthetic route of P1

Compound 12 (0.13 g, 0.18 mmol) commercially purchased donor group (D1) (0.10 g, 0.18 mmol) was added to 50 mL schlenk tube. The schlenk tube was vacuumed and gassed with N_2 several times. Then, potassium carbonate (K_2CO_3, 2M, in water) was placed in the schlenk tube, and toluene (toluene: water 3:2 ratio) solvent was added with two drops of Aliquat-336. After that, the bubbling process was performed for 30 min. Pd $(PPh_3)_4$ (0.025 g, 0.022 mmol) was added, and the reaction medium was stirred at 90 °C for 36 hr. Upon noticing condensation in the solution, cold methanol was poured into the reaction mixture and precipitated. The methanol-crude polymer mixture was mixed for 30 minutes by discarding the palladium scavenger to get rid of possible palladium residues. Then, a Soxhlet treatment was applied to the crude polymer with methanol, hexane, acetone, and chloroform solvents, respectively. The polymer was collected in the chloroform fraction (0.095 g, 60% yield).

GPC Results: M_n= 3.8 kDa, M_w=7.8 kDa, PDI=2.04

2.3.2 Synthesis of P1-Br

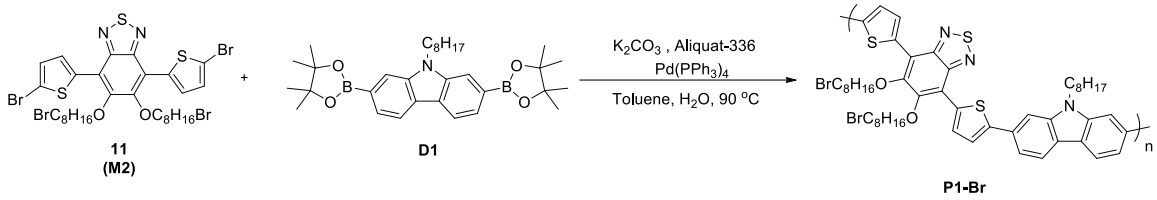

Figure 2.19. Synthetic route of P1-Br

Compound 11 (0.12 g, 0.14 mmol) commercially purchased donor group (D1) (0.075 g, 0.14 mmol) was added to 50 mL schlenk tube. The schlenk tube was vacuumed and gassed with N_2 several times. Then, potassium carbonate (K_2CO_3, 2M, in water) was placed in the schlenk tube, and toluene (toluene: water 3:2 ratio) solvent was added with two drops of Aliquat-336. After that, the bubbling process was performed for 30 min. Pd $(PPh_3)_4$ (0.020 g, 0.017 mmol) was added, and the reaction medium was stirred at 90 °C for 36 hr. Upon noticing condensation in the solution, cold methanol was poured into the reaction mixture and precipitated. The methanol-crude polymer mixture was mixed for 30 minutes by discarding the palladium scavenger to get rid of possible palladium residues. Then, a Soxhlet treatment was applied to the crude polymer with methanol, hexane, acetone, and chloroform solvents, respectively. The polymer was collected in the chloroform fraction (0.072 g, 51% yield).

GPC Results: M_n= 6.2 kDa, M_w=7.0 kDa, PDI=1.12

2.3.3 Synthesis of P1-SH

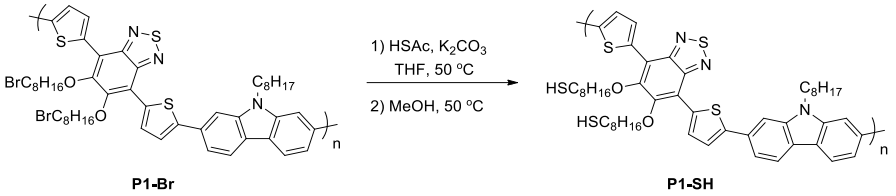

Figure 2.20. Synthetic route of P1-SH

P1-Br (0.060 g, 0.059 mmol) and potassium carbonate (K_2CO_3) (0.036 g, 0.259 mmol) were dissolved in 15 mL dry THF in a 25 mL schlenk tube and stirred under nitrogen gas for 30 min. Then, thioacetic acid (C_2H_4OS) (0.010 mL, 0.130 mmol) was added to the solution and the reaction medium was brought to 50 °C and stirred for 15 hours. Then, 15 mL of methanol was added to the solution and stirring was continued for 30 minutes. To neutralize the reaction medium, 1-2 drops of diluted HCl were added and the reaction was terminated. After the solvents were removed under reduced pressure, the organic phase was collected by treatment with chloroform and water. After the collected organic phase was dried with magnesium sulfate, chloroform was removed with the aid of reduced pressure and P1-SH (0.050 g, 91% yield) was obtained.

GPC Results: M_n= 5.0 kDa, M_w=10.0 kDa, PDI=2.01

2.3.4 Synthesis of P2

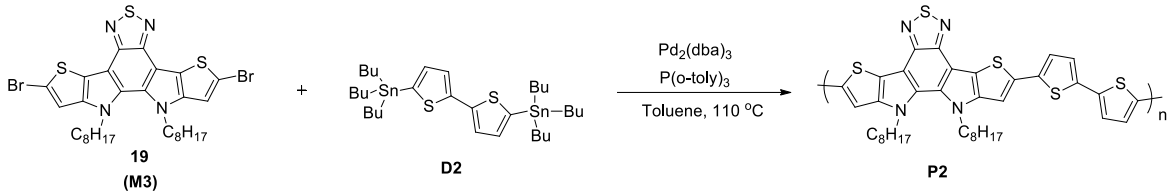

Figure 2.21. Synthetic route of P2

Compound 19 (0.15 g, 0.21 mmol), commercially purchased donor group (D2) (0.16 g, 0.21 mmol) and tri(o-tolyl) phosphine ($(C_{21}H_{21})P$) (0.005 g, 0.017 mmol) were placed in a two-neck 25 mL schlenk tube. To purify the reaction environment from moisture and oxygen as much as possible, after vacuuming 3 times, nitrogen gas was given to the environment. After this treatment, the compounds in the tube were dissolved in dry toluene (7 mL) solvent. The solution was degassed under nitrogen gas to get rid of possible water in the solvent. After the degassing process was completed, tris(dibenzylideneacetone)dipalladium (0) ($Pd_2(dba)_3$) (0.004 g, 0.004 mmol) was added and the reaction medium was stirred at 110 °C for 15 hours. Upon noticing solidification in the solution, the reaction liquid was poured into cold methanol and precipitated. The methanol crude polymer mixture was mixed for 30 minutes by discarding the palladium trap to get rid of possible palladium residues. Then, the Soxhlet treatment was applied to the crude polymer with methanol, acetone, hexane, chloroform solvents, respectively. The chloroform fraction of the clean polymer was collected (97 mg, 62% yield).

GPC Results: M_n= 2.8 kDa, M_w=3.4 kDa, PDI=1.22

2.3.5 Synthesis of P3

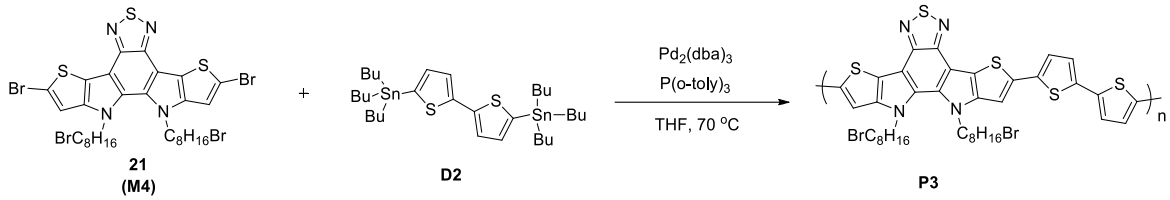

Figure 2.22. Synthetic route of P3

Compound 19 (0.088 g, 0.10 mmol), commercially purchased donor group (D2) (0.076 g, 0.10 mmol) and tri(o-tolyl) phosphine ($(C_{21}H_{21})P$) (0.003 g, 0.008 mmol) were placed in a two-neck 25 mL schlenk tube. To purify the reaction environment from moisture and oxygen as much as possible, after vacuuming 3 times, nitrogen gas was given to the environment. After this treatment, the compounds in the tube were dissolved in dry THF (5 mL) solvent. The solution was degassed under nitrogen gas to get rid of possible water in the solvent. After the degassing process was completed, tris(dibenzylideneacetone)dipalladium (0) ($Pd_2(dba)_3$) (0.002 g, 0.002 mmol) was added and the reaction medium was stirred at 70 °C for 15 hours. Upon noticing solidification in the solution, the reaction liquid was poured into cold methanol and precipitated. The methanol crude polymer mixture was mixed for 30 minutes by discarding the palladium trap to get rid of possible palladium residues. Then, the Soxhlet treatment was applied to the crude polymer with methanol, acetone, hexane, chloroform solvents, respectively. The chloroform fraction of the clean polymer was collected (60 mg, 66% yield).

GPC Results: M_n= 3.0 kDa, M_w=4.1 kDa, PDI=1.39

2.4 Synthesis of Gold Nanoparticle

In this study, the gold nanoparticles were synthesized with laser ablation technique in a liquid. The following is an explanation of the fundamentals of nanoparticle production by laser ablation in liquid. The laser light transforms the target material

from solid to plasma at the point where it focuses on it. A shock wave is formed as a result of this effect at the point where the plasma cloud is formed. This shock wave causes energy to be released into the fluid. As a result of the liquid's effect, the plasma begins to cool and transforms into a gas. As a result of the gaseous conversion, an oscillating cavitation bubble is created. The target substance, which has cooled from the plasma to the gaseous state, and the liquid substance, which has cooled from the liquid to the gaseous state, are inside this bubble. In this bubble, nanoparticles begin to develop. Later, this cavitation bubble explodes, and because of the explosion results in the formation of another shock wave. The shock wave's nanoparticles spread into the liquid, resulting in the formation of a nanoparticle colloid [56].

The synthesis of Au-NPs was carried out with a pulsed ND:YLF (neodymium-doped yttrium lithium fluoride) laser, which is commercially available. The radiation wavelength of the laser was 527 nm, and the average radiation power was 21 W. In addition, the pulse duration was 10 ns, and the pulse energy was 21 mJ for 1kHz. The Au block was cleaned in an ultrasonic bath with acetone and alcohol to avoid contamination after being washed with distilled water. Then, the Au block was put in a vessel with 8 mL of solvent. Then, the pulsed laser was focused on the Au block using a lens. This process took 5 min. In this production, 8 mL colloid with Au-NPs was produced at approximately 0.500 mg/mL concentration.

2.5 Characterization of Polymers and Gold Nanoparticles

2.5.1 Polymer Characterizations

The structural characterization for the synthesized polymers was performed with nucleic magnetic resonance (NMR) spectroscopy analyses, while the size characterization was carried out with gel permeation chromatography (GPC). The information about optical and electronic properties was learned with UV-Vis spectroscopy and cyclic voltammetry (CV). In addition, the thermal analyses were

performed using the thermal gravimetric analysis (TGA) method and differential scanning calorimetry (DSC) method. The photovoltaic performances of the synthesized polymers were studied while constructing solar cell devices.

2.5.1.1 Nuclear Magnetic Resonance Spectroscopy

The chemical structures of molecules and polymers were characterized using Bruker Spectrospin Avance DPX-400 spectrometer with NMR spectroscopy technique as mentioned materials and equipment part. The units of presented chemical shifts for ^{1}H NMR and ^{13}C NMR are in terms of ppm. TMS that is an internal reference gives a signal at 0 ppm. Three different deuterated solvents were used in this study. These were chloroform-d ($CDCl_3$), dimethyl sulfoxide-d_6 ($(CD_3)_2SO$) and acetone-d_6 ($(CD_3)_2CO$). The signals for the deuterated solvents appear at 7.26 ppm, 2.50 ppm, and 2.05 ppm for ^{1}H NMR, respectively, and in the ^{13}C NMR, 77.16 ppm for chloroform-d, 39.52 ppm for dimethyl sulfoxide-d_6, 29.84 ppm, and 206.26 ppm for acetone-d_6.

2.5.1.2 Gel Permeation Chromatography

Gel permeation chromatography (GPC) technique is one of the most effective techniques which is used for the determination of the average molecular weight distribution of polymers. In addition, the polydispersity index (PDI) of polymers can also calculate with this technique. The stationary phase is solid, and the mobile phase is liquid. Moreover, the standard calibration is performed with polystyrene reference. Chloroform was used as a mobile phase, and the characterizations were made with a 2.0 mg/mL concentration.

2.5.1.3 Electrochemical Studies

Cyclic voltammetry (CV) is a valuable method for investigating the synthesized polymers' redox potentials and estimating their HOMO and LUMO energy levels. Electronic band gaps of polymers are also calculated from the difference between HOMO and LUMO energy levels.

CV setup includes a three-electrode system which consists of the reference electrode (RE), counter electrode (CE), and the working electrode (WE). Silver (Ag) wire was used as the reference electrode, while the platinum wire was used as the counter electrode. Moreover, ITO that was coated with the synthesized polymer is the working electrode. The polymers were coated by the spray coating technique. The supporting electrolyte that ensured ionic conductivity was tetrabutylammonium hexafluorophosphate ($TBAPF_6$), and acetonitrile (ACN) was chosen as a solvent to dissolve the supporting electrolyte. The reason for preferring ACN solvent is that the solvent should not dissolve the polymer while it dissolves the electrolyte. In addition, the electrolyte should not react with the solvent. All electrodes were located in a cell that was filled with ACN solvent, which includes 0.1 M $TBAPF_6$, as shown in Figure 2.23. Potentiostat applied preferred potential to the working electrode with respect to the reference electrode. A current was generated between the counter and the working electrode.

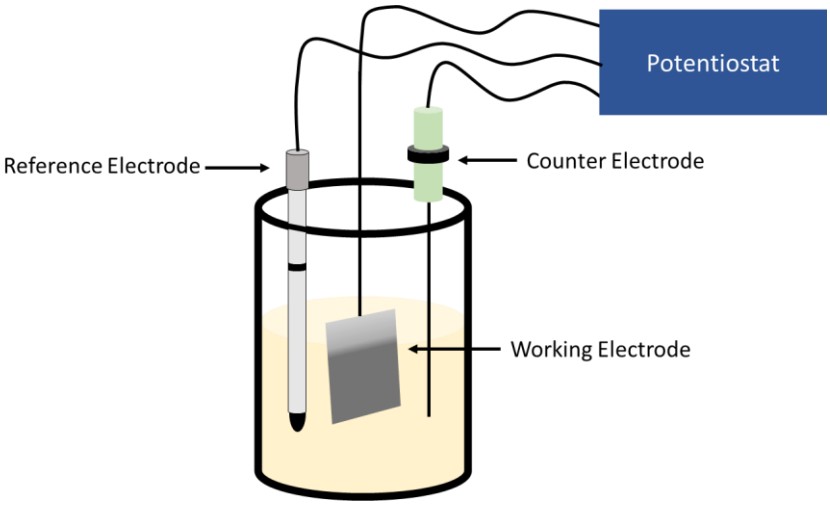

Figure 2.23. Experimental setup of cyclic voltammetry

2.5.1.4 Optical Studies

The optical energy band gaps of semiconductors are estimated by UV-Vis spectroscopy using light absorption as a function of wavelength. In this method, visible and near-infrared (NIR) ranges are scanned with a spectrophotometer. All studies were performed on both solution and thin-film absorption spectra. The polymers were dissolved in the chloroform solvent, and spray coating was applied for thin-film analysis.

2.5.1.5 Thermal Studies

Two varied methods were performed to analyze the thermal properties of the synthesized polymers. These methods were thermal gravimetric analysis (TGA) and differential scanning calorimetry (DSC). The information about the change in weight with temperature change is obtained from the TGA measurement. In addition, the decomposition temperature (T_d) is determined at the point where there is a 5% weight loss. Moreover, to determine the melting point (T_m) and the glass transition temperature (T_g), DSC analysis is performed by applying the varied rate of heat flow among the reference and the polymer in time.

2.5.1.6 Device Fabrication and Photovoltaic Studies

The conventional bulk heterojunction organic solar cell devices were fabricated by coating ITO/PEDOT:PSS/Polymer:$PC_{71}BM$/LİF/Al on the glass substrate, respectively. In the first step, zinc powder and hydrochloric acid were introduced to ITO-coated glass that is commercially available to decrease the active area on the glass. The cleaning process of ITO with detergent, distilled water, and isopropyl alcohol in order using an ultrasonication bath for 15 min for each mentioned solvent was the second step. After that, O_2 plasma treatment was performed for 5 min to increase the work function of ITO as the third step. Moreover, O_2 plasma treatment provides decreased surface tension for ITO to ease the coating of the PEDOT:PSS layer and to remove organic contamination on the surface. In the fourth step, PEDOT:PSS solution, which passed through a polyethersulfone (PES) filter with 0.45 μm pore size, was coated with the spin coating technique and annealed at 140 °C for 15 min to eliminate residues that come from water. Thereafter, in the fifth step, a blend of Polymer:PCBM that dissolved in the solvent was also coated with spin coating and passed through a polytetrafluoroethylene (PTFE) filter that has a 0.45 μm pore size on the PEDOT:PSS layer in the glove box system. Finally, metal evaporation was performed in a vacuum evaporation chamber that was placed in the glove box system, and LiF/Al layer was coated. After the fabrication of the devices, the photovoltaic measurements were carried out under illumination with AM 1.5G filter in the glove box system using the Keithley instrument.

2.5.2 Gold Nanoparticle Characterizations

In this study, the characterization of plasmonic Au-NPs was carried out with UV-Vis spectroscopy and scanning electron microscopy (SEM) techniques by National Nanotechnology Research Center (UNAM).

CHAPTER 3

RESULTS AND DISCUSSIONS

3.1 Optical and Morphological Studies of Gold Nanoparticles

In this study, the laser ablation technique was used for nanoparticle synthesis in a liquid by research group of Dr. Bülend Ortaç. The basis of this technique can be explained as follow. At the point where the laser light is focused on the target, a plasma cloud is formed. With the effect of the liquid, the plasma begins to cool and turns into a gas. An oscillating cavitation bubble is formed because of the gaseous conversion. Nanoparticles start to form in this bubble. Later, this cavitation bubble bursts, and a shock wave is formed as a result of the explosion. Nanoparticles formed by this shock wave disperse into the liquid, and a nanoparticle colloid is produced [57].

In this production, the concentration of gold nanoparticles was approximately 0.500 mg/mL. The purity of gold is 91.6%, and the remainder contains copper. The size characterization of the produced particles was done in scanning electron microscopy, and the characterization of the plasmonic property was done in ultraviolet-visible spectroscopy. According to the result obtained in UV-Vis spectroscopy, as shown in Figure 3.1, the nanoparticles produced have plasmonic properties, and the peak absorption wavelength of the colloid is 548 nm [35]. The size of the particles produced appears to be less than 50 nm, and they are not monodispersed, as shown in Figure 3.2.

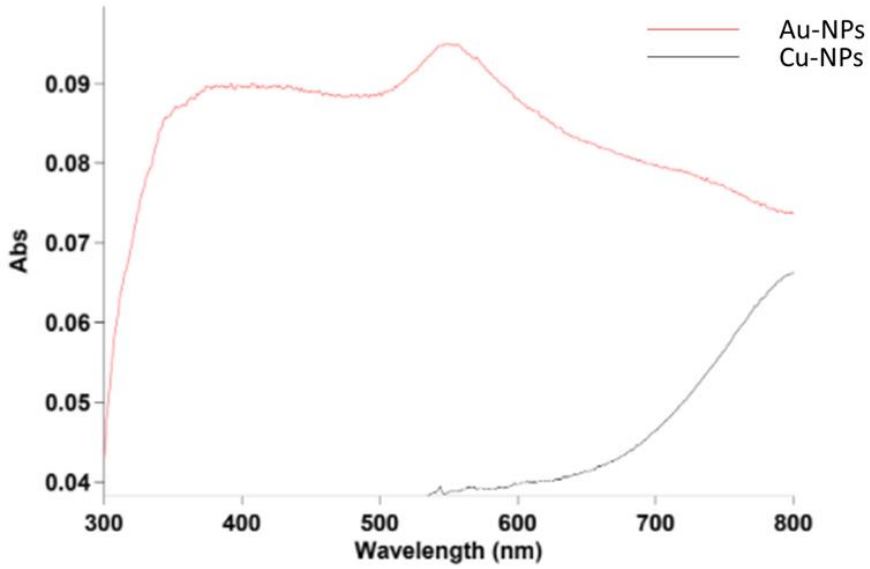

Figure 3.1.UV-Vis spectrum of the produced particles

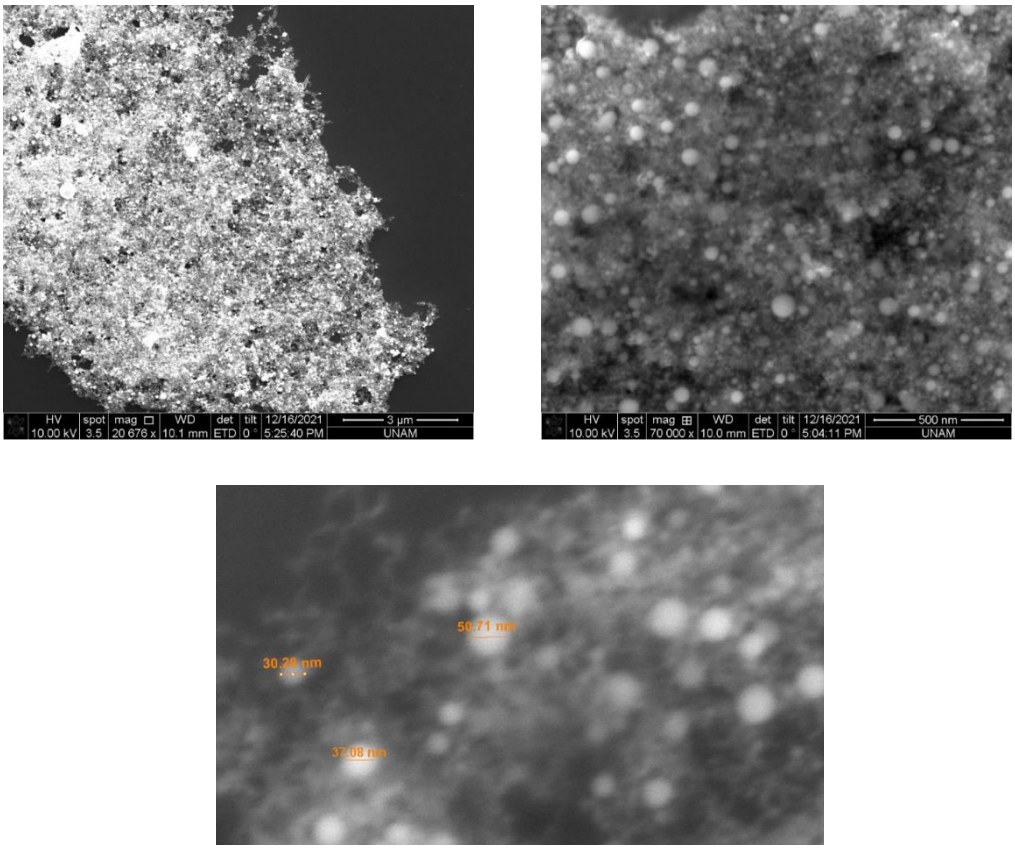

Figure 3.2. SEM images of produced nanoparticles

3.2 Electrochemical Studies of Polymers

As mentioned earlier in Section 2.5.1., cyclic voltammetry (CV) is a valuable method for investigating the synthesized redox potentials of polymers and estimating their HOMO and LUMO energy levels by using a three-electrode system. Polymers, which dissolve in chloroform, were spray coated on glass that was already coated with ITO and served as a working electrode in the experiment. The cyclic voltammograms of P1, P1-Br, and P1-SH are shown in Figure 3.3. According to oxidation and reduction values, all corresponding polymers have an ambipolar character so that polymers show n-dopable and p-dopable properties.

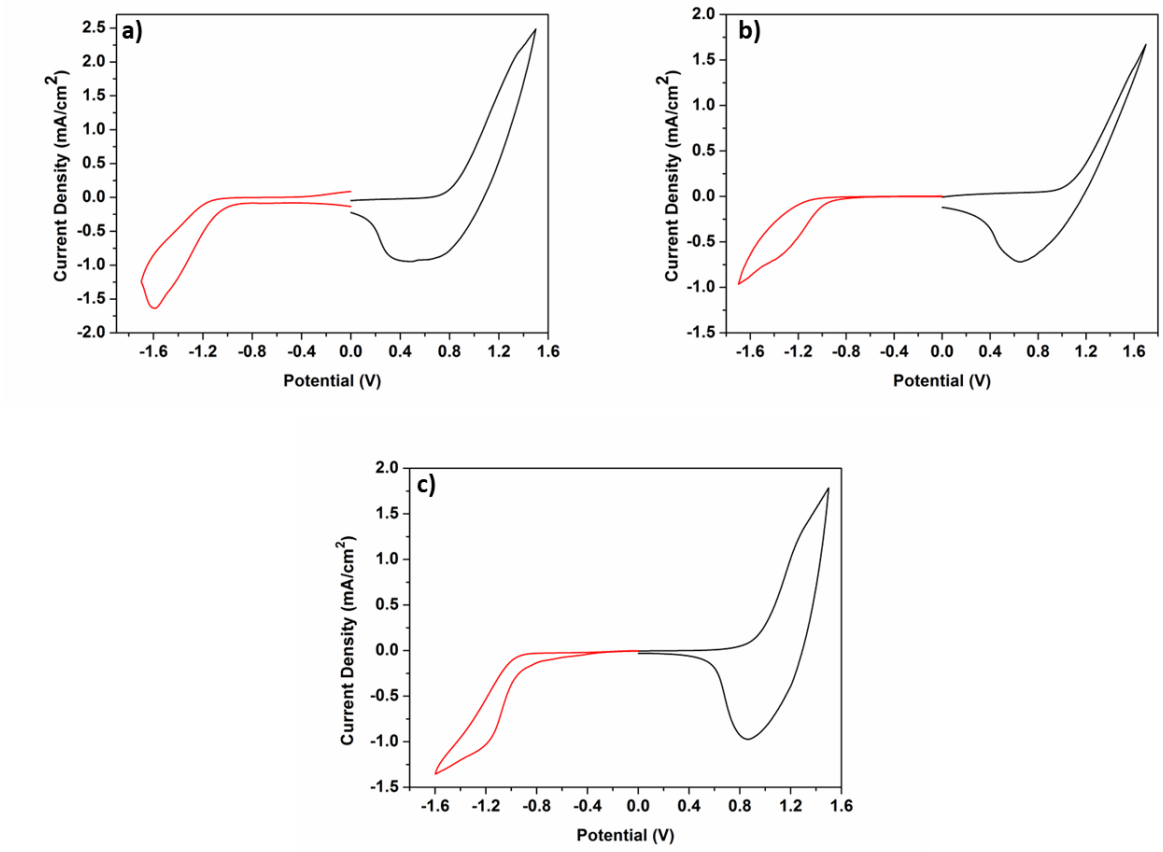

Figure 3.3. Cyclic Voltammograms of polymers a) P1, b)P1-Br, c) P1-SH in 0.1 M $TBAPF_6$ /ACN at 100 mV/s scan rate

From the cyclic voltammograms, onset oxidation and onset reduction potentials were obtained. The E_{ox}^{onset} of P1, P1-Br, and P1-SH were found as 0.80, 1.05, and 0.93, while E_{red}^{onset} of polymers were found as -1.05, -0.90, and -0.90, respectively. HOMO and LUMO energy levels and electronic band gap of polymers were calculated from the following equations using onset reduction and onset oxidation potential values obtained from CV (Standard Hydrogen Electrode vs vacuum level was taken 4.75 eV).

$$HOMO = -(4.75 + E_{ox}^{onset})eV$$

$$LUMO = -(4.75 + E_{red}^{onset})eV$$

$$E_g^{el} = (HOMO - LUMO)eV$$

HOMO energy levels were calculated -5.55 eV, -5.80 eV, and -5.68 eV, while LUMO energy levels were evaluated -3.70 eV, -3.85 eV and -3.85 eV in order of P1, P1-Br and P1-SH. The electronic band gaps were found as 1.85 eV, 1.95 eV, and 1.83 eV, respectively.

Table 3.1. Electrochemical properties of the P1, P1-Br and P1-SH

Polymer	E_{ox} (V)	E_{red} (V)	E_{ox}^{onset} (V)	E_{red}^{onset} (V)	HOMO (eV)	LUMO (eV)	Eg^{el} (eV)
P1	1.35	-1.60	0.80	-1.05	-5.55	-3.70	1.85
P1-Br	1.60	-1.40	1.05	-0.90	-5.80	-3.85	1.95
P1-SH	1.30	-1.20	0.93	-0.90	-5.68	-3.85	1.83

All polymers have HOMO and LUMO values that are ideal for building organic solar cells. For effective charge transfer, the energy levels of $PC_{71}BM$ and the polymers produce large enough HOMO-HOMO and LUMO-LUMO offsets. Additionally,

electronic band gaps of polymers are small (2.0 eV), which improves the likelihood that photons from solar radiation can be captured [58].

Compared to P1, P1-Br has a wider electrical band gap. A decline in effective π-conjugation length may be the cause of this band gap expansion [59]. Given that bromine is a very large atom, bromine groups at the ends of alkyl chains may interfere with the linearity and aggregation of polymers in the solid state.

In comparison to P1 and P1-Br, P1-SH has a narrower electrical band gap. The likelihood that a reaction between the sulfhydryl (SH) side chains will result in the formation of a disulfide bond. An electron is released when an S anion from one sulfhydryl group works as a nucleophile and attacks the side chain of another to form a disulfide bond [60]. The electronic band gap might decrease as a result of this circumstance.

The cyclic voltammograms of P2 and P3 are shown in Figure 3.4. According to cyclic voltammograms, P2 and P3 have also shown n-dopable and p-dopable properties, which indicate ambipolar character.

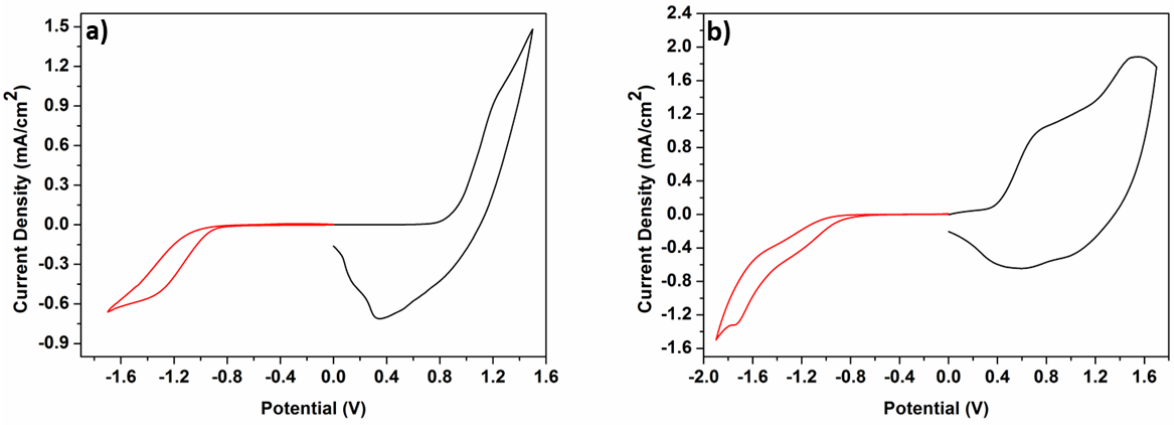

Figure 3.4. Cyclic Voltammograms of polymers a) P2, b)P3 in 0.1 M $TBAPF_6$ /ACN at 100 mV/s scan rate

From the cyclic voltammograms, onset oxidation and onset reduction potentials were obtained. The E_{ox}^{onset} of P2 and P3 were investigated as 0.92 V and 0.58 V, while

E_{red}^{onset} of polymers were detected as -0.95 V and -1.25 V, respectively. HOMO and LUMO energy levels and electronic band gap of polymers were calculated from the same equations using onset reduction and onset oxidation potential values obtained from CV.

For P2, HOMO energy level was calculated -5.67 eV while LUMO energy level was evaluated -3.80 eV. The electronic band gap found as 1.87 eV.

For P3, HOMO energy level was calculated -5.33 eV while LUMO energy level was evaluated -3.50 eV. The electronic band gap found as 1.83 eV.

Table 3.2. Electrochemical properties of the P2 and P3

Polymer	E_{ox} (V)	E_{red} (V)	E_{ox}^{onset} (V)	E_{red}^{onset} (V)	HOMO (eV)	LUMO (eV)	Eg^{el} (eV)
P2	0.95	-1.35	0.92	-0.95	-5.67	-3.80	1.87
P3	0.75	-1.70	0.58	-1.25	-5.33	-3.50	1.83

3.3 Optical Studies of Polymers

In this study, the absorption of polymers in the visible region and near-infrared region were investigated to obtain optical properties. Normalized UV-Vis absorption spectra of the corresponding polymers are shown in Figures 3.4 and 3.5, both spray-coated thin film and solution forms. Optical band gaps were calculated from λ_{max}^{onset} of thin film UV-Vis spectra. As expected, all polymers show two absorption peaks in the visible and near-infrared regions. Generally, the absorption peak indicated in the shorter wavelength (350 -450 nm) or near-IR part comes from the π-π^* transition, while the absorption peak revealed visible area or higher wavelength (450-700 nm) comes from intramolecular chain transfer between donor and acceptor materials [61]. Moreover, in the solid state, the interchain interactions are increased with higher

crystallinity and aggregation. Therefore, thin film spectra of all polymers show a bathochromic or redshift at their maximum wavelength (λ_{max}) as expected [62].

The optical band gap of the P1 polymer analog in the literature is 1.96 eV [44]. However, considering the lower molecular weight of the polymer synthesized in this study, it is an expected result that the optical band gap of the P1 polymer decreases at 1.81 eV [63]. The alkyl chains of P1-Br have a bromine functional group at the end of them. Due to the size of the bromine atom, bromine groups at the terminals of alkyl chains can interfere with the linearity and aggregation of solid polymers. This may cause an increase in the optical band gap. In addition, a similar situation exists for the P1-SH polymer. Both the presence of a relatively large atom at the end of the alkyl chain and the possibility of crosslinking between thiol groups may have caused an increase in the optical band gap [64].

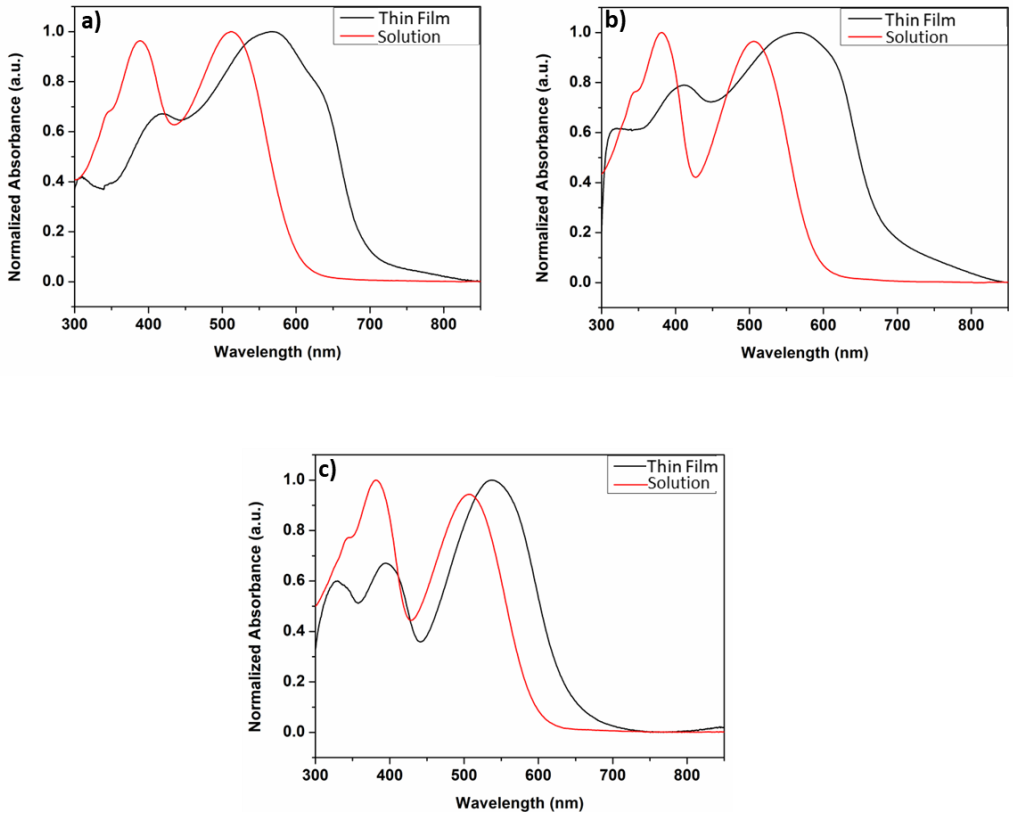

Figure 3.5. Normalized UV-Vis absorption spectra of synthesized a) P1, b)P1-Br, c) P1-SH in $CHCl_3$ solution and thin film

Table 3.3. Optical properties of the P1, P1-Br and P1-SH

Polymer	Thin Film λ_{max} (nm)	Thin Film λ_{max}^{onset} (nm)	Eg^{op} (eV)
P1	565	685	1.81
P1-Br	565	670	1.85
P1-SH	540	637	1.95

P2 and P3 showed higher band broadening and a higher red shift in the solid state compared to other polymers. In addition, the presence of long wavelength shoulders in the solid state indicates high aggregation [65]. The planar and fused structural properties of P2 and P3 from the cyclization of two thiophene rings on the benzothiadiazole structure result in improved intermolecular electronic interactions in the solid state.

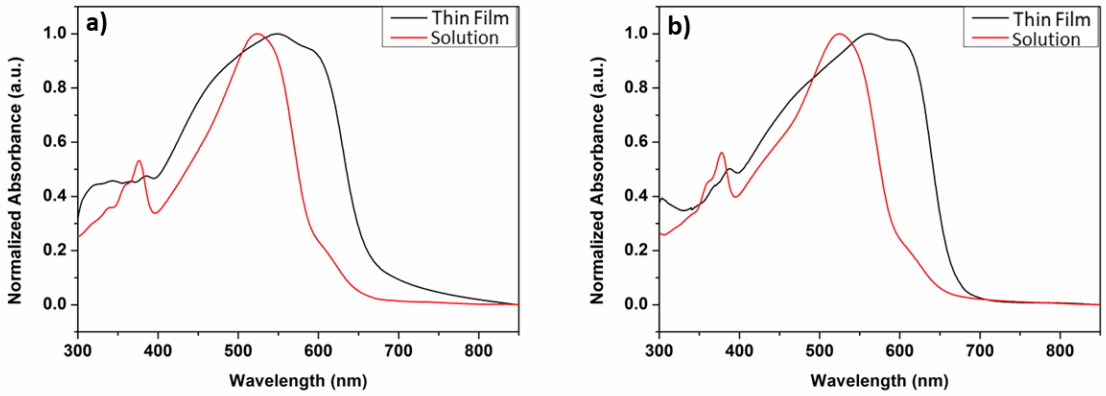

Figure 3.6. Normalized UV-Vis absorption spectra of synthesized a) P2, b)P3 in $CHCl_3$ solution and thin film

Table 3.4. Optical properties of the P2 and P3

Polymer	Thin Film λ_{max} (nm)	Thin Film λ_{max}^{onset} (nm)	Eg^{op} (eV)
P2	545	665	1.87
P3	560	670	1.85

3.4 Thermal Studies of Polymers

Thermal analyses of the synthesized polymers were performed with TGA, and thermograms are available in the appendix part. Analyses were carried out at rising heating speed at a temperature of 10 °C/min between 25 and 600 °C under a nitrogen atmosphere. According to Table 3.5, the decomposition temperature, at which 5% weight loss starts, of the polymers P1, P1-Br, P1-SH, P2, and P3 are 360 °C, 305 °C, 280 °C, 255 °C, and 245 °C, respectively. The morphology of the constructed devices could be affected by the thermal stability of polymers. Therefore, this situation can also affect the efficiency of the solar cell. The deformation and degradation of the morphology of constructed devices could be decreased by using polymers with higher thermal stability [66]. When the differences in solar cell efficiencies of P1, P1-Br, and P1-SH are compared, it can be said that thermal stabilities could be one of the factors affecting the power conversion efficiency of devices.

Table 3.5. Results of polymerizations and thermal studies of polymers

Polymer	M_n (kDa)	M_w(kDa)	PDI	T_d (°C)
P1	3.8	7.8	2.04	360
P1-Br	6.2	7.0	1.12	305
P1-SH	5.0	10.0	2.01	280

P2	2.8	3.4	1.22	255
P3	3.0	4.1	1.39	245

3.5 Organic Solar Cell Applications of Polymers

As mentioned in section 2.5.1, the conventional bulk heterojunction organic solar cell devices were fabricated by conventional architectures, ITO/PEDOT:PSS/Polymer:$PC_{71}BM$/LİF/Al. The short circuit current density and open circuit voltage were obtained under illumination (AM 1.5G, 100 mW/cm^2). $PC_{71}BM$ is inherently more soluble than other fullerenes such as $PC_{61}BM$ [67]. In addition, $PC_{61}BM$ has lower absorption and a less broad peak in the visible region than $PC_{71}BM$ [68]. In this study, therefore, $PC_{71}BM$ was used for the fullerene acceptor.

The energy level diagram of organic solar cell devices constructed with P1, P1-Br, and P1-SH are illustrated in Figure 3.6. The information about HOMO and LUMO energy levels and also band gaps are obtained from CV measurement. P1 is already synthesized polymer in the literature with different alkyl chains and the organic solar cell device of the polymer in this series was fabricated under conditions where the polymers exhibit optimum photovoltaic performance in the literature [44]. Polymer:$PC_{71}BM$ ratio was 1:2 (w/w), and all solutions were prepared in the o-DCB solvent. Figure 3.7 represents the J-V curves of the P1, P1-Br, and P1-SH for the 1:2 Polymer:$PC_{71}BM$ ratio. When the photovoltaic performance of P1 and P1-Br is investigated, it is observed that PCE decreases from 2.06 % to 1.52%. It can be explained by the decrease in the Jsc. This is the expected result because the existence of the brom atom at the tip of the alkyl chain restrains charges and excitons. So that photocurrent production efficiency and PCE decrease. In the thiol modification of the same polymer, P1-SH, the PCE decreases to 1.22% with the decline in both FF

and Jsc values. This situation reveals that the thiol modification of this polymer chain is poor in terms of photovoltaic performance.

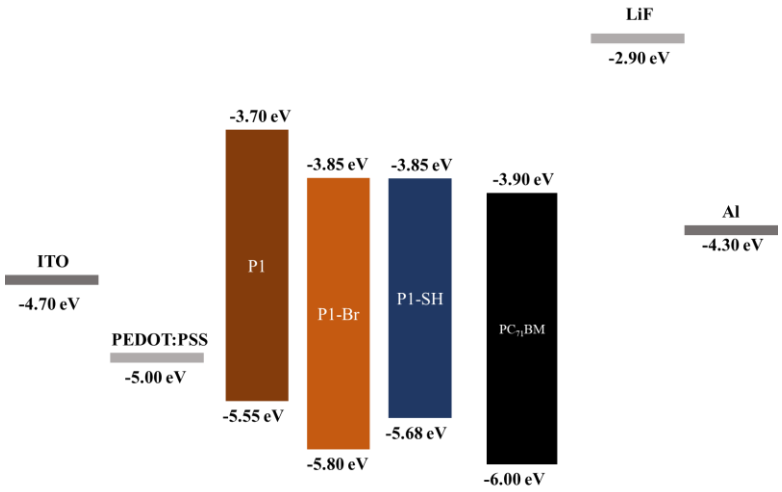

Figure 3.7. Energy level diagram of the P1, P1-Br and P1-SH

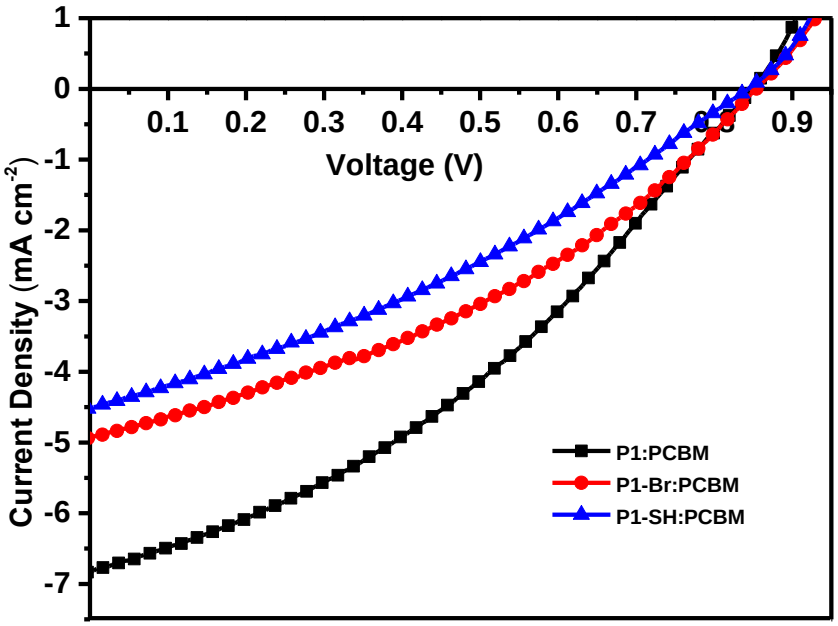

Figure 3.8. J-V curves of the P1, P1-Br and P1-SH for 1:2 Polymer:PCBM ratio

Table 3.6. Comparison of photovoltaic properties of P1, P1-Br and P1-SH

Polymer	Solvent	P:$PC_{71}BM$ (w:w)	Concentration (mg ml^{-1})	J_{sc} (mA cm^{-2})	V_{oc} (V)	FF (%)	PCE (%)
P1	o-DCB	1:2	24	6.82	0.85	36	2.06
P1-Br	o-DCB	1:2	24	4.91	0.85	36	1.52
P1-SH	o-DCB	1:2	24	4.50	0.85	32	1.22

Optimization of solar cells containing P1-SH continued with the addition of gold nanoparticles to the active layer solutions. Gold nanoparticle optimizations are shown in Table 3.7. Two different solvents were used to disperse the gold nanoparticle. As a result of the characterization, it was seen that using THF as a solvent gave better results than methanol. Then, nanoparticles were dispersed in THF at different concentrations to be optimized. Although it was observed that the power conversion efficiency increased as the gold nanoparticle concentration increased, the highest power conversion efficiency obtained with the addition of gold nanoparticles is 1.08%.

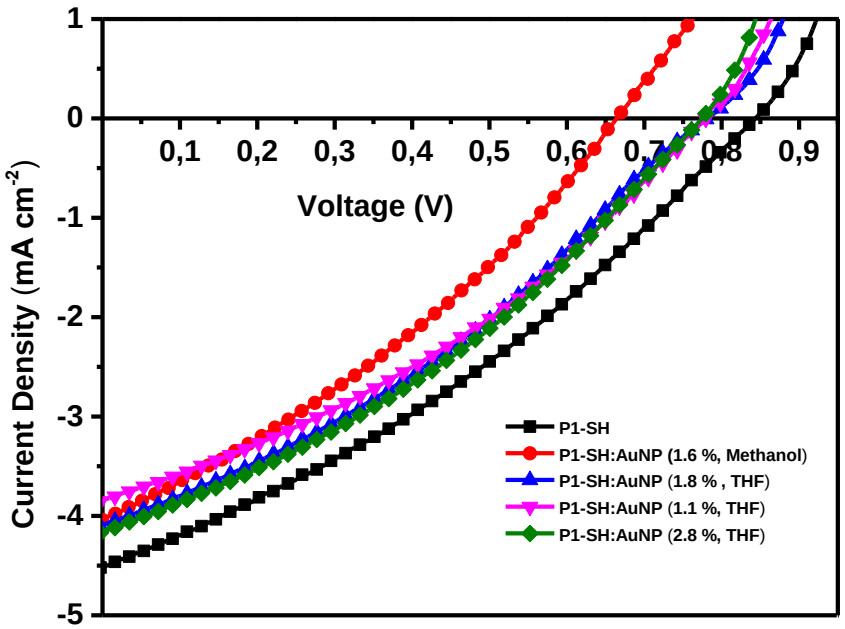

Figure 3.9. J-V curves of the P1-SH with AuNP in different solvents and at different concentrations

Table 3.7. Comparison of photovoltaic properties of the P1, P1-SH and P1-SH:AuNP

Polymer	Au-NP (%)	Au-NP Solvent	P:$PC_{71}BM$ (w:w)	Concentration (mg/ml)	J_{sc} (mA/cm^2)	V_{oc} (V)	FF (%)	PCE (%)
P1	-	-	1:2	24	6.82	0.85	36	2.06
P1-SH	-	-	1:2	24	4.50	0.85	32	1.22
P1-SH	1.6	MeOH	1:2	24	4.02	0.67	32	0.86
P1-SH	1.1	THF	1:2	24	3.83	0.78	34	1.02
P1 SH	1.8	THF	1:2	24	4.09	0.78	32	1.04
P1-SH	**2.8**	**THF**	**1:2**	**24**	**4.18**	**0.78**	**33**	**1.08**

Low solubilities of P2 and P3 did not allow for obtaining proper thin film to fabricate working solar cell devices.

3.6 Morphology Analysis of Polymers

The topographic characterizations of the active layers were studied by atomic force microscopy (AFM). The level differences in AFM results reveal the aggregation and solubility issues of the blends. The root mean square roughness (Rq) of the P1, P1-Br, P1-SH, and P1-SH:AuNPs layers blended with PCBM were calculated as 1.54 nm, 0.62 nm, 1.15 nm, and 0.71 nm, respectively. The thicknesses of the active layers were measured as 110 nm, 110 nm, 108 nm, and 94 nm, respectively. When the results were examined, it was observed that all surfaces were smooth, and there was no distinctive situation between the surfaces.

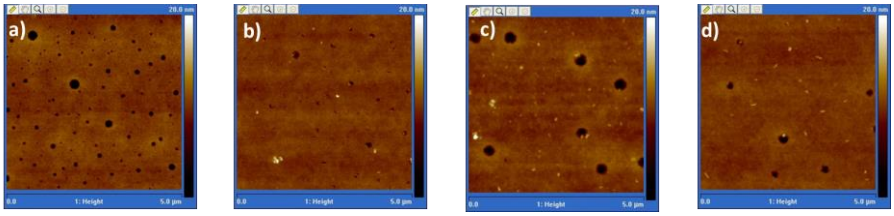

Figure 3.10. AFM images of photoactive layers a) P1:$PC_{71}BM$ (1:2, w:w), b) P1-Br :$PC_{71}BM$ (1:2, w:w), c) P1-SH :$PC_{71}BM$ (1:2, w:w), d) P1-SH-AuNP:$PC_{71}BM$ (1:2, w:w)

The morphology characterizations of the active layers were studied by Transmission electron microscopy (TEM). The results project the two-dimensional image of the blends. The dark areas correspond to PCBM while white regions correspond to polymer, giving an insight into the active layer morphology. The results primarily provide a homogeneous and interpenetrating network, and there are no signs of fibril structures.

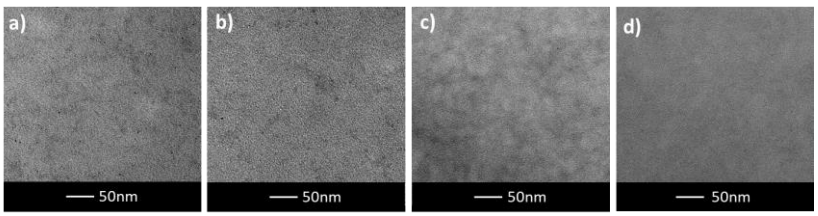

Figure 3.11. TEM images of a) P1:$PC_{71}BM$ (1:2, w:w), b) P1-Br :$PC_{71}BM$ (1:2, w:w), c) P1-SH :$PC_{71}BM$ (1:2, w:w), d) P1-SH-AuNP:$PC_{71}BM$ (1:2, w:w)

CHAPTER 4

CONCLUSION

Five different conjugated polymers were synthesized for this study. Polymers were synthesized at low molecular weight to perform post-polymerization reactions. Optical and morphological studies of gold nanoparticles were investigated. The size characterization of the produced particles was done in scanning electron microscopy, and the characterization of the plasmonic property was done in ultraviolet-visible spectroscopy. The size of the particles produced appears to be less than 50 nm. According to the result obtained in UV-vis spectroscopy, the nanoparticles produced have plasmonic properties, and the peak absorption wavelength of colloid is 548 nm. Electrochemical, optical, thermal, and photovoltaic studies of all polymers were also investigated. All polymers showed ambipolar character and suitable energy levels. HOMO and LUMO levels of polymers were found as -5.55 eV/-3.70 eV, -5.80 eV/ -3.85 eV, -5.68 eV/-3.85 eV, -5.67 eV/-3.80 eV, and -5.33 eV/-3.50 eV for P1, P1-Br, P1-SH, P2, and P3 respectively. Optical band gaps of polymers were calculated from thin-film absorption spectra and found 1.81, 1.85, 1.95, 1.87, and 1.85 for P1, P1-Br, P1-SH, P2 and P3, respectively. According to thermal studies, P1, P1-Br and P1-SH are thermally stable up to 360 °C, 305 °C, and 280 °C, respectively, while P2 and P3 are thermally stable up to 255 °C and 245 °C, respectively. Photovoltaic studies of P1, P1-Br and P1-SH were investigated and best device performances in terms of PCE were found as 2.06 % for P1, 1.52 % for P1-Br, 1.22 % for P1-SH. Photovoltaic studies of P1-SH:AuNPs were investigated and the best device performance in terms of PCE was found as 1.08 %. There were no signs of fibril structures for P1, P1-Br and P1-SH and P1-SH:AuNP which resulted in a decrease in PCE. Low solubilities of P2 and P3 did not allow to obtain proper thin film to fabricate working solar cell devices. These results indicate that synthesized polymers

are not promise high power conversion efficiencies for the solar cell application, and interaction with gold nanoparticles for P1-SH does not give effective results.

REFERENCES

[1] I. - All rights reserved, Database documentation RENEWABLES INFORMATION 2021 EDITION, (n.d.). http://wds.iea.org/wds/pdf/ren_documentation.pdf. (accessed February 2, 2022).

[2] Renewables - Fuels & Technologies - IEA, (n.d.). https://www.iea.org/fuels-and-technologies/renewables (accessed February 2, 2022).

[3] Renewable Energy | Center for Climate and Energy Solutions, (n.d.). https://www.c2es.org/content/renewable-energy/ (accessed February 2, 2022).

[4] P.G.V. Sampaio, M.O.A. González, Photovoltaic solar energy: Conceptual framework, Renewable and Sustainable Energy Reviews. 74 (2017) 590–601. https://doi.org/10.1016/j.rser.2017.02.081.

[5] K. Orgil, S. Project, Comparison of Organic and Inorganic Solar Photovoltaic Systems, 2018.

[6] Best Research-Cell Efficiency Chart | Photovoltaic Research | NREL, (n.d.). https://www.nrel.gov/pv/cell-efficiency.html (accessed February 3, 2022).

[7] Glossary of basic terms in polymer science (IUPAC Recommendations 1996), n.d.

[8] D.D.C. Bradley, J. Burroughes, A.B. Holmes, A. Kraft, Light-emitting diodes based on conjugated polymers Poly(arlene vinylene)s for organic electronics View project Fluorinated conjugated polymers View project, 1992. https://www.researchgate.net/publication/3586942.

[9] H. Shirakawa, E.J. Louis, A.G. MacDiarmid, C.K. Chiang, A.J. Heeger, Synthesis of electrically conducting organic polymers: Halogen derivatives of polyacetylene, (CH) x, Journal of the Chemical Society, Chemical Communications. (1977) 578. doi:10.1039/c39770000578.

[10] T.H. Le, Y. Kim, H. Yoon, Electrical and electrochemical properties of conducting polymers, Polymers (Basel). 9 (2017). https://doi.org/10.3390/polym9040150.

[11] T. Tadesse, Application of Conjugated Organic Polymers for Photovoltaic's: Review, J Phys Chem Biophys. 08 (2018). https://doi.org/10.4172/2161-0398.1000263.

[12] J.C.S. Costa, R.J.S. Taveira, C.F.R.A.C. Lima, A. Mendes, L.M.N.B.F. Santos, Optical band gaps of organic semiconductor materials, Opt Mater (Amst). 58 (2016) 51–60. https://doi.org/10.1016/j.optmat.2016.03.041.

[13] S. Günes, H. Neugebauer, N.S. Sariciftci, Conjugated polymer-based organic solar cells, Chem Rev. 107 (2007) 1324–1338. https://doi.org/10.1021/cr050149z.

[14] E.E. Havinga, W. ten Hoeve, H. Wynberg, Alternate donor-acceptor small-band-gap semiconducting polymers; Polysquaraines and polycroconaines, Synthetic Metals. 55 (1993) 299–306. doi:10.1016/0379-6779(93)90949-w.

[15] H. Lee, D. Lee, D.H. Sin, S.W. Kim, M.S. Jeong, K. Cho, Effect of donor–acceptor molecular orientation on charge photogeneration in organic solar cells, NPG Asia Mater. 10 (2018) 469–481. https://doi.org/10.1038/s41427-018-0054-1.

[16] 287616-Article Text-397221-1-10-20150217 (1), (n.d.).

[17] J. Liu, J.-B. Baek, L. Dai, Conjugated Polymer Synthesis, in: Encyclopedia of Polymeric Nanomaterials, Springer Berlin Heidelberg, 2014: pp. 1–7. https://doi.org/10.1007/978-3-642-36199-9_273-1.

[18] S. Singh Gujral, S. Khatri, P. Riyal, Synthesis and Characterization of Asymmetrical Gemini Surfactants View project Suzuki Cross Coupling Reaction-A Review, 2012. https://www.researchgate.net/publication/258934824.

[19] V. Farina, V. Krishnamurthy, W.J. Scott, The Stille reaction, Organic Reactions . (1997) 1–652. https://doi.org/doi:10.1002/0471264180.or050.01.

[20] H. Kim, S. Nam, J. Jeong, S. Lee, J. Seo, H. Han, Y. Kim, Organic solar cells based on conjugated polymers: History and recent advances, Korean Journal of Chemical Engineering. 31 (2014) 1095–1104. https://doi.org/10.1007/s11814-014-0154-8.

[21] S. Günes, H. Neugebauer, N.S. Sariciftci, Conjugated polymer-based organic solar cells, Chem Rev. 107 (2007) 1324–1338. https://doi.org/10.1021/cr050149z.

[22] N.S. Sariciftci, L. Smilowitz, A.J. Heeger, F. Wudi, Eos 72 (fall suppl, 1991. www.sciencemag.org.

[23] M. Zhang, H. Wang, C.W. Tang, Effect of the highest occupied molecular orbital energy level offset on organic heterojunction photovoltaic cells, Appl Phys Lett. 97 (2010). https://doi.org/10.1063/1.3491214.

[24] Y. Min Nam, J. Huh, W. Ho Jo, Optimization of thickness and morphology of active layer for high performance of bulk-heterojunction organic solar cells, Solar Energy Materials and Solar Cells. 94 (2010) 1118–1124. https://doi.org/10.1016/j.solmat.2010.02.041.

[25] A.J. Heeger, 25th anniversary article: Bulk heterojunction solar cells: Understanding the mechanism of operation, Advanced Materials. 26 (2014) 10–28. https://doi.org/10.1002/adma.201304373.

[26] C. Sae-Kung, B.F. Wright, T.M. Clarke, G.G. Wallace, A.J. Mozer, Effects of Interfacial Layers on the Open Circuit Voltage of Polymer/Fullerene Bulk Heterojunction Devices Studied by Charge Extraction Techniques, ACS Appl Mater Interfaces. 11 (2019) 21030–21041. https://doi.org/10.1021/acsami.9b02850.

[27] C.B. Nielsen, S. Holliday, H.Y. Chen, S.J. Cryer, I. McCulloch, Non-Fullerene Electron Acceptors for Use in Organic Solar Cells, Acc Chem Res. 48 (2015) 2803–2812. https://doi.org/10.1021/acs.accounts.5b00199.

[28] X. Liu, C. Zhang, C. Duan, M. Li, Z. Hu, J. Wang, et al., Morphology optimization via side chain engineering enables all-polymer solar cells with excellent fill factor and stability, Journal of the American Chemical Society. 140 (2018) 8934–8943. doi:10.1021/jacs.8b05038.

[29] H. Hoppe, N.S. Sariciftci, Organic solar cells: An overview, J Mater Res. 19 (2004) 1924–1945. https://doi.org/10.1557/JMR.2004.0252.

[30] L. Wang, M. Hasanzadeh Kafshgari, M. Meunier, Optical Properties and Applications of Plasmonic-Metal Nanoparticles, Adv Funct Mater. (2020). https://doi.org/10.1002/adfm.202005400.

[31] D. Alloyeau, C. Mottet, C. Ricolleau, eds., Nanoalloys, Springer London, London, 2012. https://doi.org/10.1007/978-1-4471-4014-6.

[32] J. Liu, H. He, D. Xiao, S. Yin, W. Ji, S. Jiang, D. Luo, B. Wang, Y. Liu, Recent advances of plasmonic nanoparticles and their applications, Materials. 11 (2018). https://doi.org/10.3390/ma11101833.

[33] H.A. Atwater, A. Polman, Plasmonics for improved photovoltaic devices, Nat Mater. 9 (2010) 205–213. https://doi.org/10.1038/nmat2629.

[34] X. Chen, M. Gu, Hole Blocking Layer-Free Perovskite Solar Cells with High Efficiencies and Stabilities by Integrating Subwavelength-Sized Plasmonic Alloy Nanoparticles, ACS Appl Energy Mater. 2 (2019) 2094–2103. https://doi.org/10.1021/acsaem.8b02145.

[35] J.L. Wu, F.C. Chen, Y.S. Hsiao, F.C. Chien, P. Chen, C.H. Kuo, M.H. Huang, C.S. Hsu, Surface plasmonic effects of metallic nanoparticles on the performance of polymer bulk heterojunction solar cells, ACS Nano. 5 (2011) 959–967. https://doi.org/10.1021/nn102295p.

[36] V. Shrotriya, E.H.E. Wu, G. Li, Y. Yao, Y. Yang, Efficient light harvesting in multiple-device stacked structure for polymer solar cells, Appl Phys Lett. 88 (2006). https://doi.org/10.1063/1.2172741.

[37] A. Yakimov, S.R. Forrest, High photovoltage multiple-heterojunction organic solar cells incorporating interfacial metallic nanoclusters, Appl Phys Lett. 80 (2002) 1667–1669. https://doi.org/10.1063/1.1457531.

[38] B. Paci, G.D. Spyropoulos, A. Generosi, D. Bailo, V.R. Albertini, E. Stratakis, E. Kymakis, Enhanced structural stability and performance durability of bulk heterojunction photovoltaic devices incorporating metallic nanoparticles, Adv Funct Mater. 21 (2011) 3573–3582. https://doi.org/10.1002/adfm.201101047.

[39] J.A. Larsson, M. Nolan, J.C. Greer, Interactions between thiol molecular linkers and the Au13 nanoparticle, Journal of Physical Chemistry B. 106 (2002) 5931–5937. https://doi.org/10.1021/jp014483k.

[40] S. Casalini, C.A. Bortolotti, F. Leonardi, F. Biscarini, Self-assembled monolayers in organic electronics, Chem Soc Rev. 46 (2017) 40–71. https://doi.org/10.1039/c6cs00509h.

[41] J.C. Love, L.A. Estroff, J.K. Kriebel, R.G. Nuzzo, G.M. Whitesides, Self-assembled monolayers of thiolates on metals as a form of nanotechnology, Chem Rev. 105 (2005) 1103–1169. https://doi.org/10.1021/cr0300789.

[42] P.E. Laibinis, G.M. Whitesides, .Omega.-terminated alkanethiolate monolayers on surfaces of copper, silver, and gold have similar wettabilities, Journal of the American Chemical Society. 114 (1992) 1990–1995. doi:10.1021/ja00032a009.

[43] D.L. Kokkin, R. Zhang, T.C. Steimle, I.A. Wyse, B.W. Pearlman, T.D. Varberg, Au-S Bonding Revealed from the Characterization of Diatomic Gold Sulfide, AuS, Journal of Physical Chemistry A. 119 (2015) 11659–11667. https://doi.org/10.1021/acs.jpca.5b08781.

[44] H.Y. Chen, S.C. Yeh, C.T. Chen, C.T. Chen, Comparison of thiophene- and selenophene-bridged donor-acceptor low band-gap copolymers used in bulk-heterojunction organic photovoltaics, J Mater Chem. 22 (2012) 21549–21559. https://doi.org/10.1039/c2jm33735e.

[45] A.A.B. Alghamdi, D.C. Watters, H. Yi, S. Al-Faifi, M.S. Almeataq, D. Coles, J. Kingsley, D.G. Lidzey, A. Iraqi, Selenophene vs. thiophene in benzothiadiazole-based low energy gap donor-acceptor polymers for photovoltaic applications, J Mater Chem A Mater. 1 (2013) 5165–5171. https://doi.org/10.1039/c3ta00122a.

[46] E. Stratakis, E. Kymakis, Nanoparticle-based plasmonic organic photovoltaic devices, Materials Today. 16 (2013) 133–146. https://doi.org/10.1016/j.mattod.2013.04.006.

[47] D.H. Wang, K.H. Park, J.H. Seo, J. Seifter, J.H. Jeon, J.K. Kim, J.H. Park, O.O. Park, A.J. Heeger, Enhanced power conversion efficiency in PCDTBT/PC 70 BM bulk heterojunction photovoltaic devices with embedded silver nanoparticle clusters, Adv Energy Mater. 1 (2011) 766–770. https://doi.org/10.1002/aenm.201100347.

[48] K. Kim, D.L. Carroll, Roles of Au and Ag nanoparticles in efficiency enhancement of poly(3-octylthiophene)/C 60 bulk heterojunction photovoltaic devices, Appl Phys Lett. 87 (2005) 1–3. https://doi.org/10.1063/1.2128062.

[49] H. Shen, P. Bienstman, B. Maes, Plasmonic absorption enhancement in organic solar cells with thin active layers, J Appl Phys. 106 (2009). https://doi.org/10.1063/1.3243163.

[50] C.H. Kim, S.H. Cha, S.C. Kim, M. Song, J. Lee, W.S. Shin, S.J. Moon, J.H. Bahng, N.A. Kotov, S.H. Jin, Silver nanowire embedded in P3HT:PCBM for high-efficiency hybrid photovoltaic device applications, ACS Nano. 5 (2011) 3319–3325. https://doi.org/10.1021/nn200469d.

[51] M. Xue, L. Li, B.J. Tremolet De Villers, H. Shen, J. Zhu, Z. Yu, A.Z. Stieg, Q. Pei, B.J. Schwartz, K.L. Wang, Charge-carrier dynamics in hybrid plasmonic organic solar cells with Ag nanoparticles, Appl Phys Lett. 98 (2011). https://doi.org/10.1063/1.3601742.

[52] G.D. Spyropoulos, M.M. Stylianakis, E. Stratakis, E. Kymakis, Organic bulk heterojunction photovoltaic devices with surfactant-free Au nanoparticles embedded in the active layer, Appl Phys Lett. 100 (2012). https://doi.org/10.1063/1.4720510.

[53] Y.J. Cheng, C.H. Chen, Y.J. Ho, S.W. Chang, H.A. Witek, C.S. Hsu, Thieno[3,2-b]pyrrolo donor fused with benzothiadiazolo, benzoselenadiazolo and quinoxalino acceptors: Synthesis, characterization, and molecular properties, Org Lett. 13 (2011) 5484–5487. https://doi.org/10.1021/ol202199v.

[54] P. Zhou, Z.G. Zhang, Y. Li, X. Chen, J. Qin, Thiophene-fused benzothiadiazole: A strong electron-acceptor unit to build D-A copolymer for highly efficient polymer solar cells, Chemistry of Materials. 26 (2014) 3495–3501. https://doi.org/10.1021/cm501052a.

[55] Z.S. Huang, H.L. Feng, X.F. Zang, Z. Iqbal, H. Zeng, D. bin Kuang, L. Wang, H. Meier, D. Cao, Dithienopyrrolobenzothiadiazole-based organic dyes for efficient dye-sensitized solar cells, J Mater Chem A Mater. 2 (2014) 15365–15376. https://doi.org/10.1039/c4ta02639j.

[56] S. Ibrahimkutty, P. Wagener, A. Menzel, A. Plech, S. Barcikowski, Nanoparticle formation in a cavitation bubble after pulsed laser ablation in liquid studied with high time resolution small angle x-ray scattering, Appl Phys Lett. 101 (2012) 103104. https://doi.org/10.1063/1.4750250.

[57] A.E. Deniz, H.A. Vural, B. Ortaç, T. Uyar, Gold nanoparticle/polymer nanofibrous composites by laser ablation and electrospinning, Mater Lett. 65 (2011) 2941–2943. https://doi.org/10.1016/j.matlet.2011.06.045.

[58] R. Kroon, M. Lenes, J.C. Hummelen, P.W.M. Blom, B. de Boer, Small bandgap polymers for organic solar cells (polymer material development in the last 5 years), Polymer Reviews. 48 (2008) 531–582. https://doi.org/10.1080/15583720802231833.

[59] J. Roncali, Molecular engineering of the band gap of π-conjugated systems: Facing technological applications, Macromol Rapid Commun. 28 (2007) 1761–1775. https://doi.org/10.1002/marc.200700345.

[60] G. Rajpal, P. Arvan, Disulfide Bond Formation, in: Handbook of Biologically Active Peptides, Elsevier Inc., 2013: pp. 1721–1729. https://doi.org/10.1016/B978-0-12-385095-9.00236-0.

[61] Y. Li, D. Liu, J. Wang, Z.G. Zhang, Y. Li, Y. Liu, T. Zhu, X. Bao, M. Sun, R. Yang, Crystalline medium-bandgap light-harvesting donor material based on β-naphthalene asymmetric-modified benzodithiophene moiety toward efficient polymer solar cells, Chemistry of Materials. 29 (2017) 8249–8257. https://doi.org/10.1021/acs.chemmater.7b02495.

[62] M.G. Manjunatha, A.V. Adhikari, P.K. Hegde, C.S. Suchand Sandeep, R. Philip, Optical characterization of a new Donor-acceptor type conjugated polymer derived from 3,4-diphenylthiophene, J Mater Sci. 44 (2009) 6069–6077. https://doi.org/10.1007/s10853-009-3838-4.

[63] S. Hayashi, S.I. Yamamoto, T. Koizumi, Effects of molecular weight on the optical and electrochemical properties of EDOT-based π-conjugated polymers, Sci Rep. 7 (2017). https://doi.org/10.1038/s41598-017-01132-5.

[64] J. Polavka, M. Uher, L. Lapcík, M. Čeppan, J. Valašek, B. Havllnová, Crosslinking of polymers by the effect of ultraviolet radiation Crosslinking of polyvinyl alcohol) in the presence of terephthalic aldehyde, Chemical Papers. 34 (1980) 780–787.

[65] H. Akpinar, Ş.C. Cevher, L. Wei, A. Cirpan, B.M. Wong, D. Venkataraman, P.M. Lahti, Poly((2-alkylbenzo[1,2,3]triazole-4,7-diyl)vinylene)s for organic

solar cells, J Polym Sci B Polym Phys. 53 (2015) 1539–1545. https://doi.org/10.1002/polb.23785.

[66] S. Bertho, G. Janssen, T.J. Cleij, B. Conings, W. Moons, A. Gadisa, J. D'Haen, E. Goovaerts, L. Lutsen, J. Manca, D. Vanderzande, Effect of temperature on the morphological and photovoltaic stability of bulk heterojunction polymer:fullerene solar cells, Solar Energy Materials and Solar Cells. 92 (2008) 753–760. https://doi.org/10.1016/j.solmat.2008.01.006.

[67] G. Bernardo, M. Melle-Franco, A.L. Washington, R.M. Dalgliesh, F. Li, A. Mendes, S.R. Parnell, Different agglomeration properties of PC61BM and PC71BM in photovoltaic inks-a spin-echo SANS study, RSC Adv. 10 (2020) 4512–4520. https://doi.org/10.1039/c9ra08019h.

[68] F. Zhang, Z. Zhuo, J. Zhang, X. Wang, X. Xu, Z. Wang, Y. Xin, J. Wang, J. Wang, W. Tang, Z. Xu, Y. Wang, Influence of PC60BM or PC70BM as electron acceptor on the performance of polymer solar cells, in: Solar Energy Materials and Solar Cells, 2012: pp. 71–77. https://doi.org/10.1016/j.solmat.2011.09.006.

APPENDICES

A. Spectra and Thermal Analyses

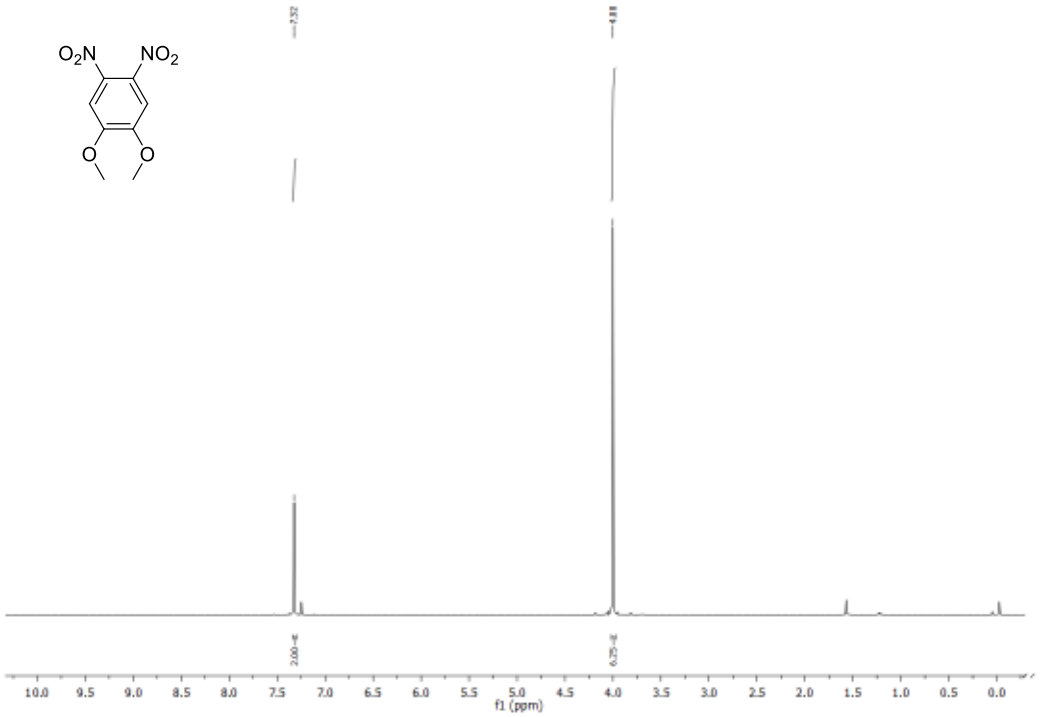

Figure A. 1. ^{1}H NMR spectrum of compound 2 in $CDCl_3$

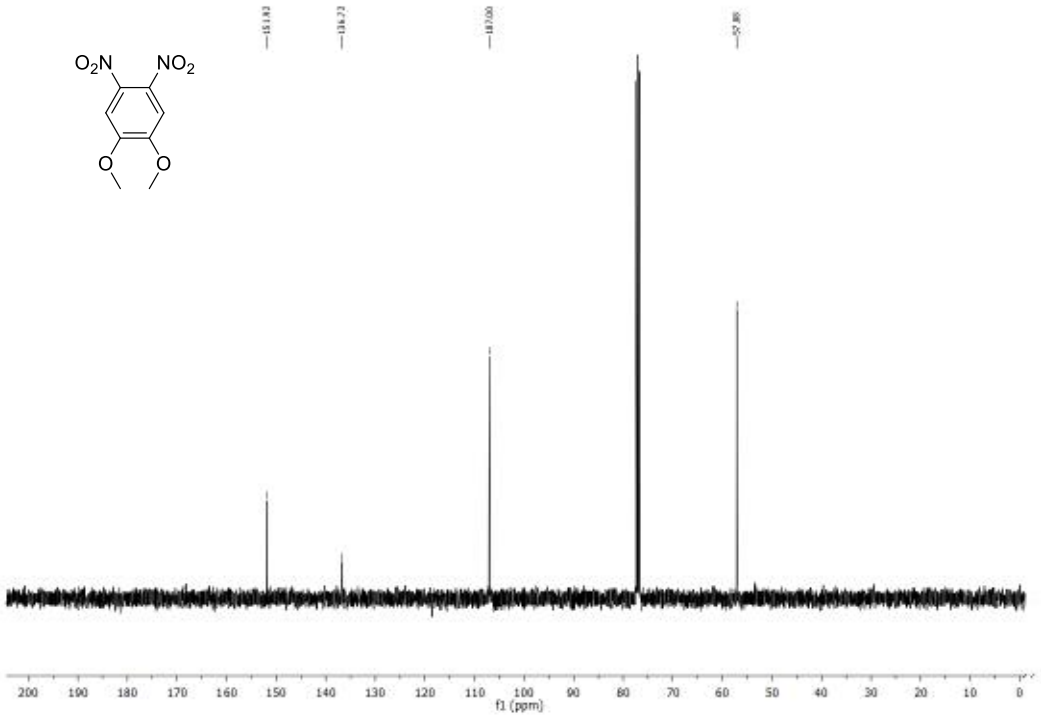

Figure A. 2. ^{13}C NMR spectrum of compound 2 in $CDCl_3$

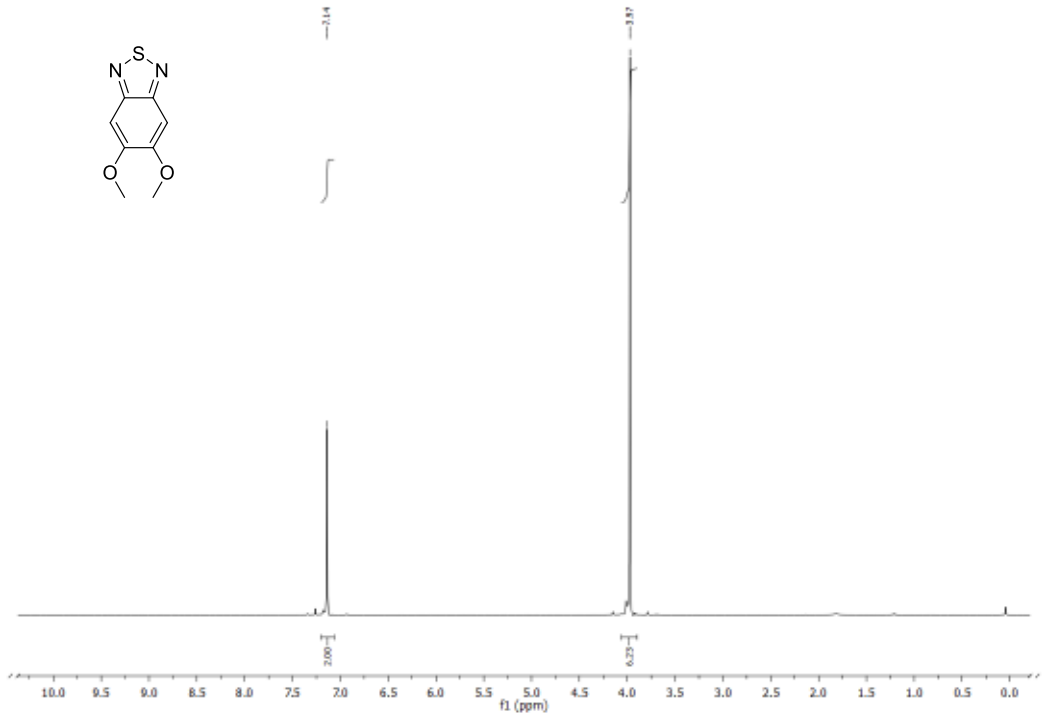

Figure A. 3. ^{1}H NMR spectrum of compound 4 in $CDCl_3$

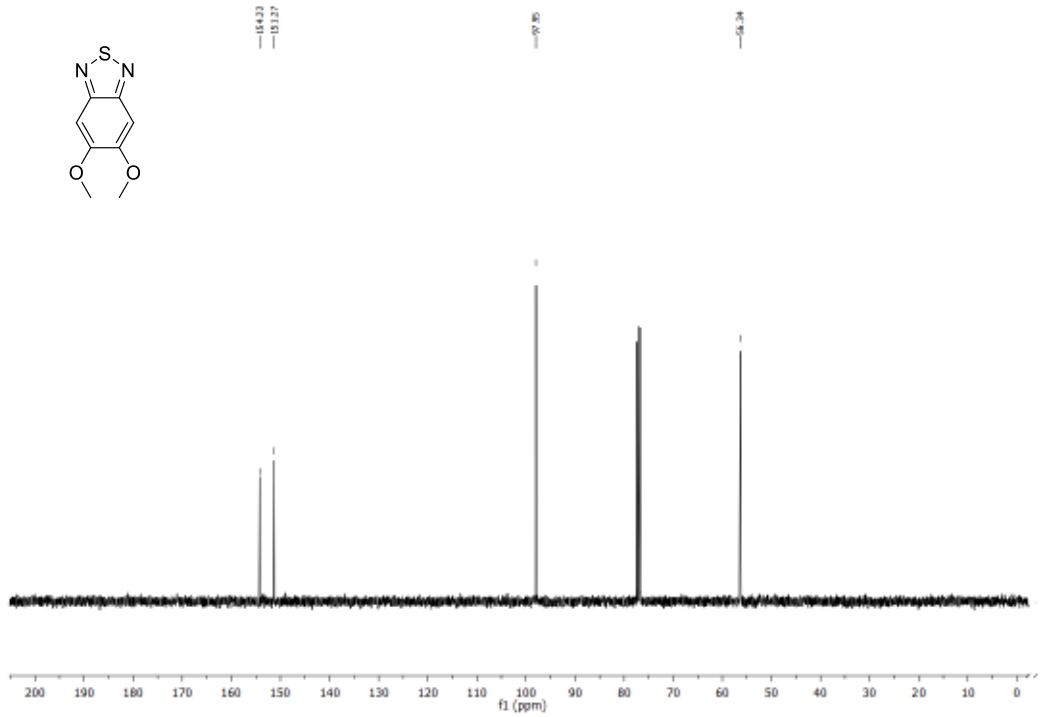

Figure A. 4. ^{13}C NMR spectrum of compound 4 in $CDCl_3$

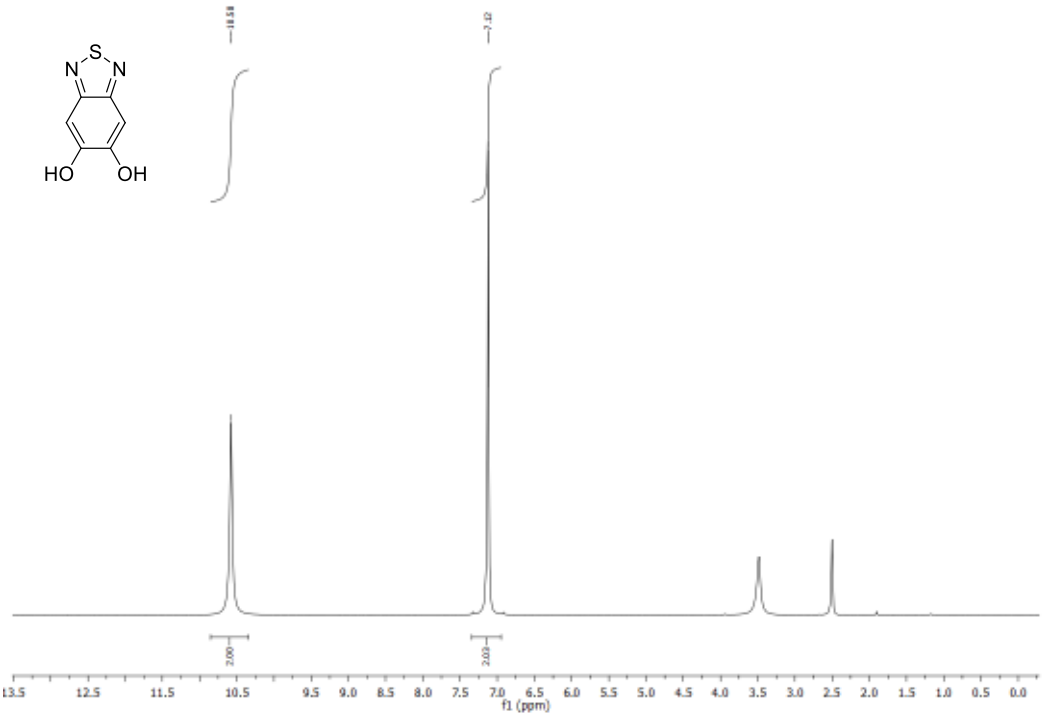

Figure A. 5. ^{1}H NMR spectrum of compound 5 in DMSO

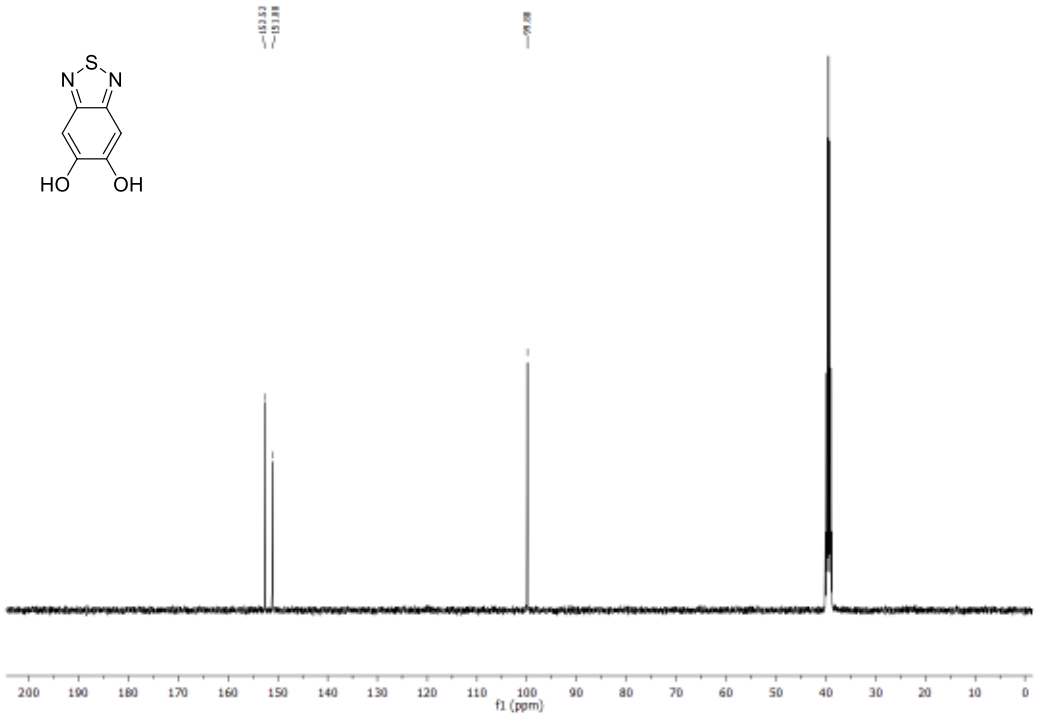

Figure A. 6.^{13}C NMR spectrum of compound 5 in DMSO

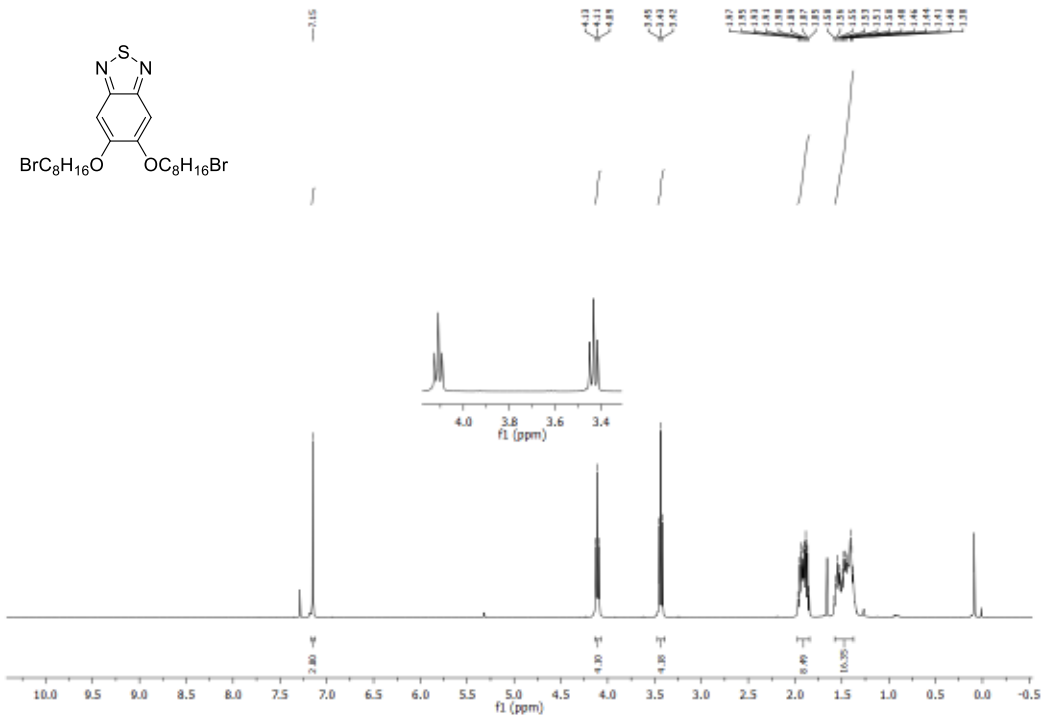

Figure A. 7. ^{1}H NMR spectrum of compound 6 in $CDCl_3$

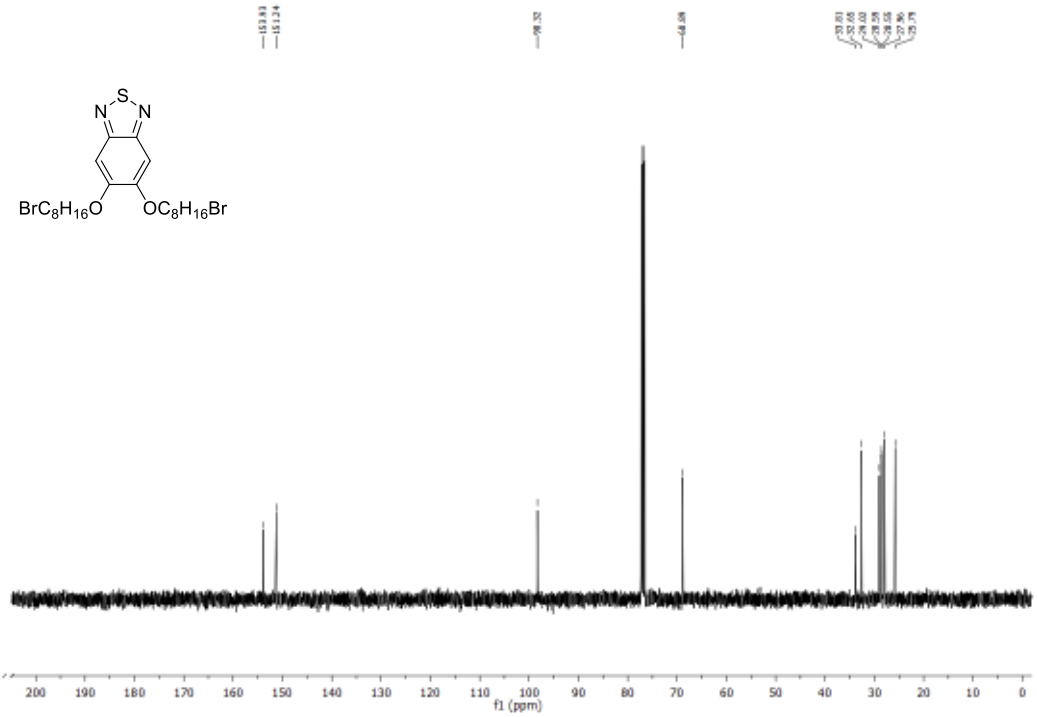

Figure A. 8.^{13}C NMR spectrum of compound 6 in $CDCl_3$

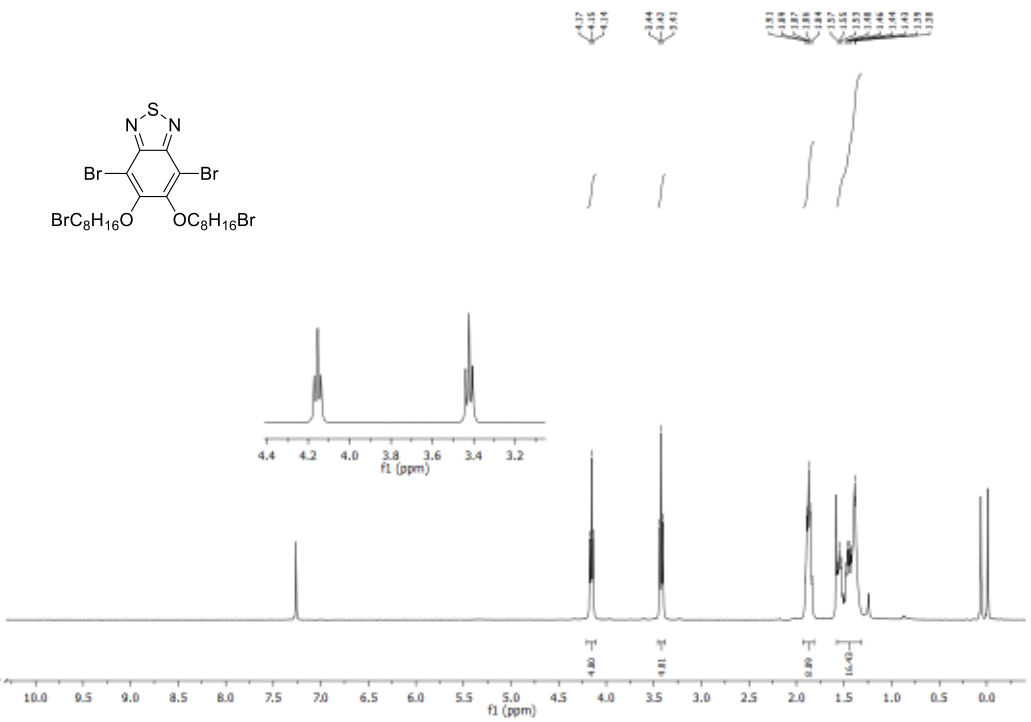

Figure A. 9. ^{1}H NMR spectrum of compound 7 in $CDCl_3$

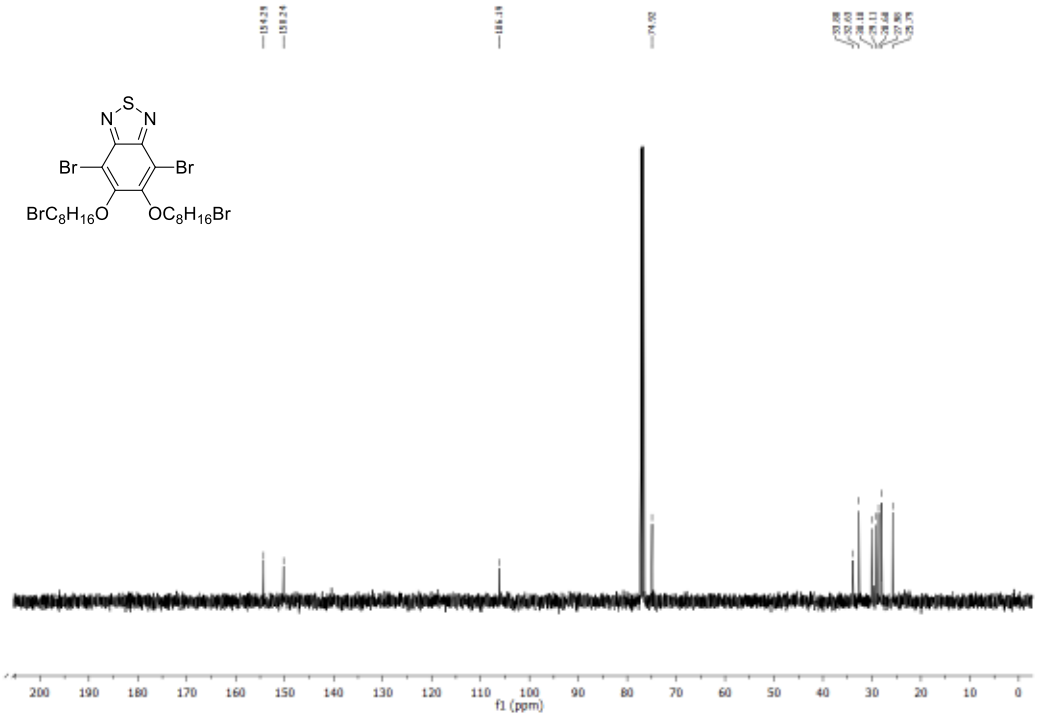

Figure A. 10. ^{13}C NMR spectrum of compound 7 in $CDCl_3$

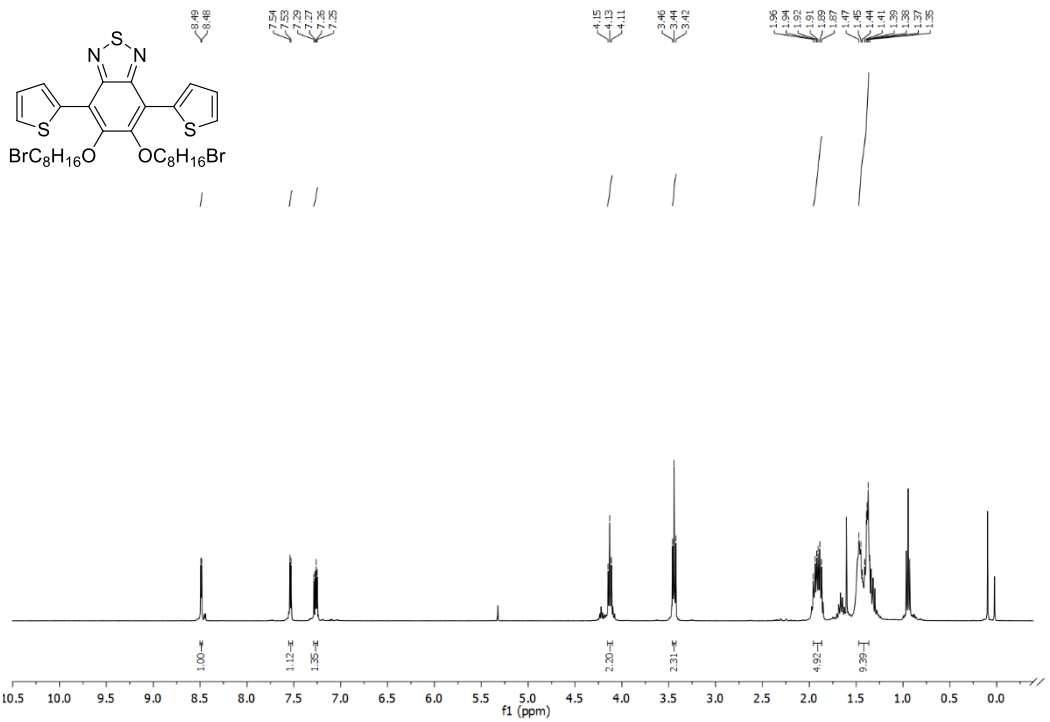

Figure A. 11. ^{1}H NMR spectrum of compound 10 in $CDCl_3$

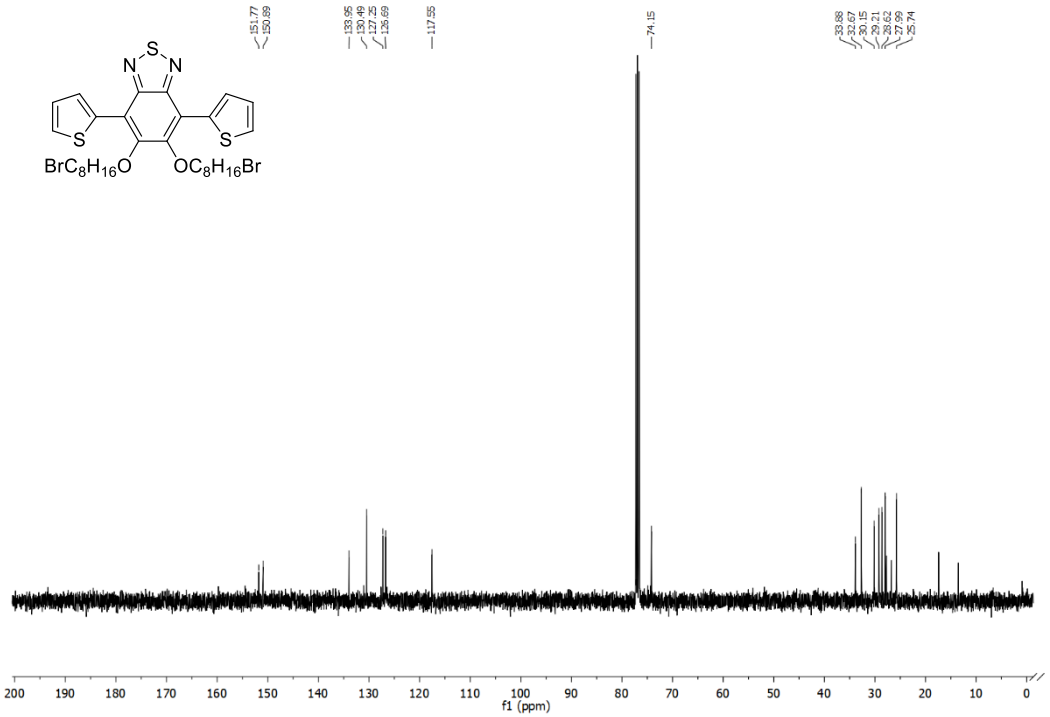

Figure A. 12. ^{13}C NMR spectrum of compound 10 in $CDCl_3$

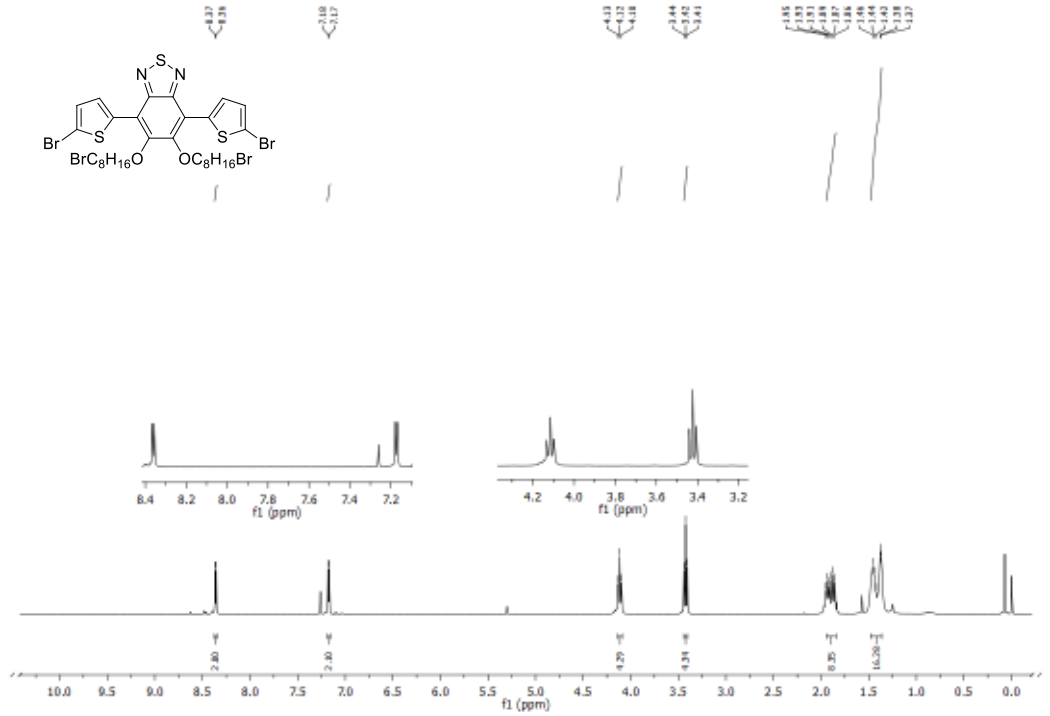

Figure A. 13. ^{1}H NMR spectrum of compound 11 in $CDCl_3$

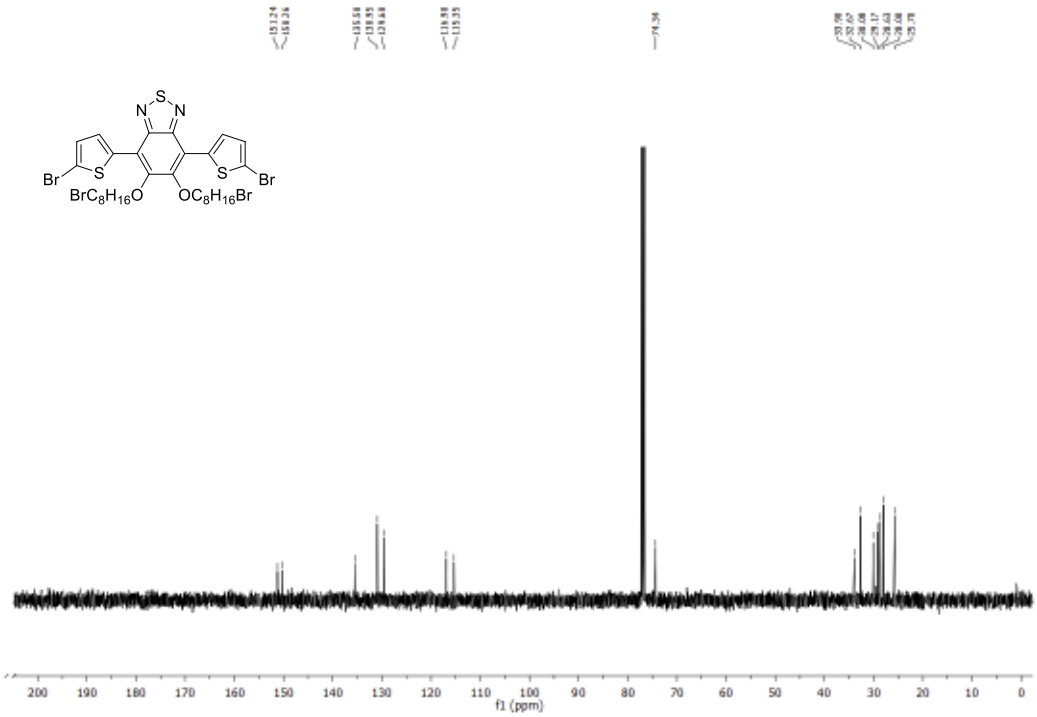

Figure A. 14. ^{13}C NMR spectrum of compound 11 in $CDCl_3$

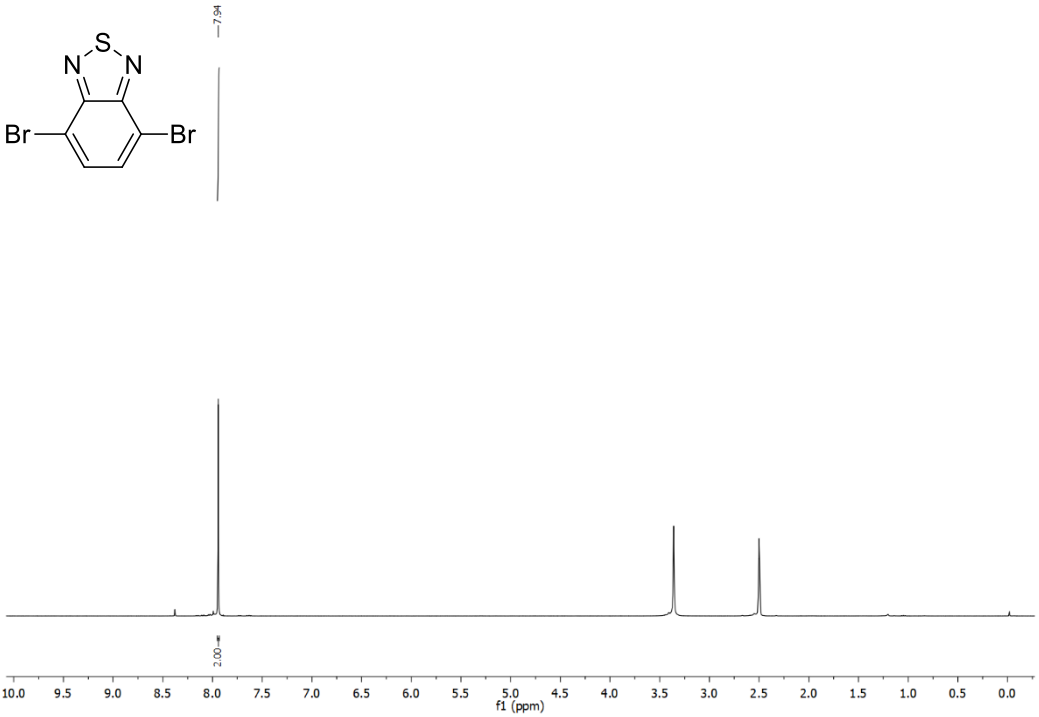

Figure A. 15. ^{1}H NMR spectrum of compound 14 in DMSO

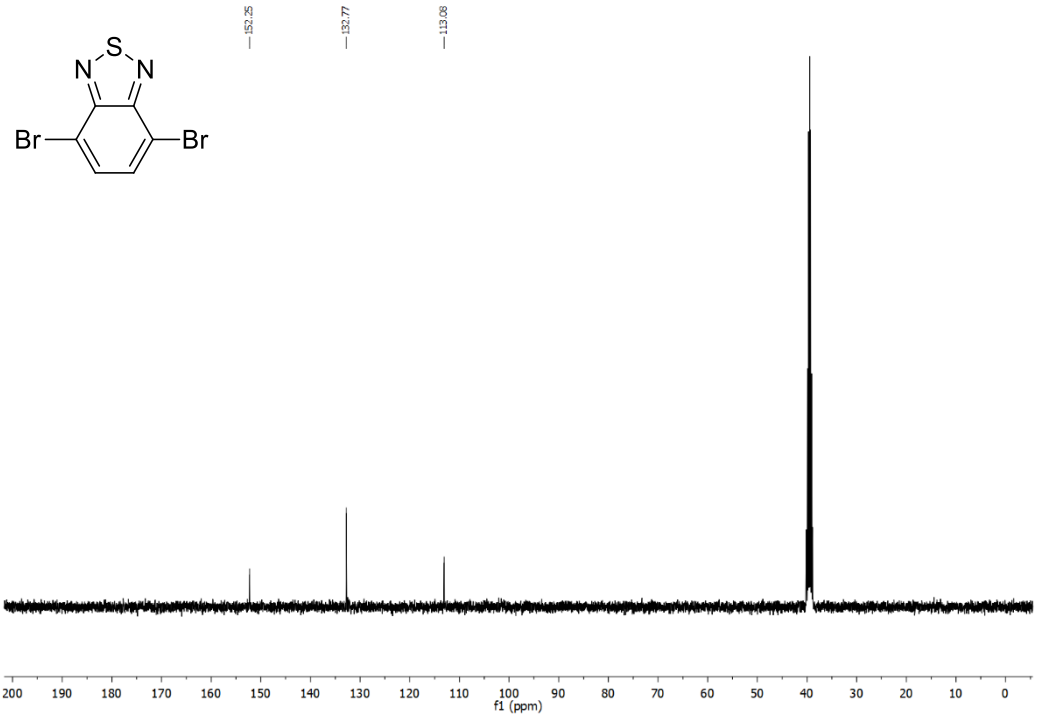

Figure A. 16. ^{13}C NMR spectrum of compound 14 in DMSO

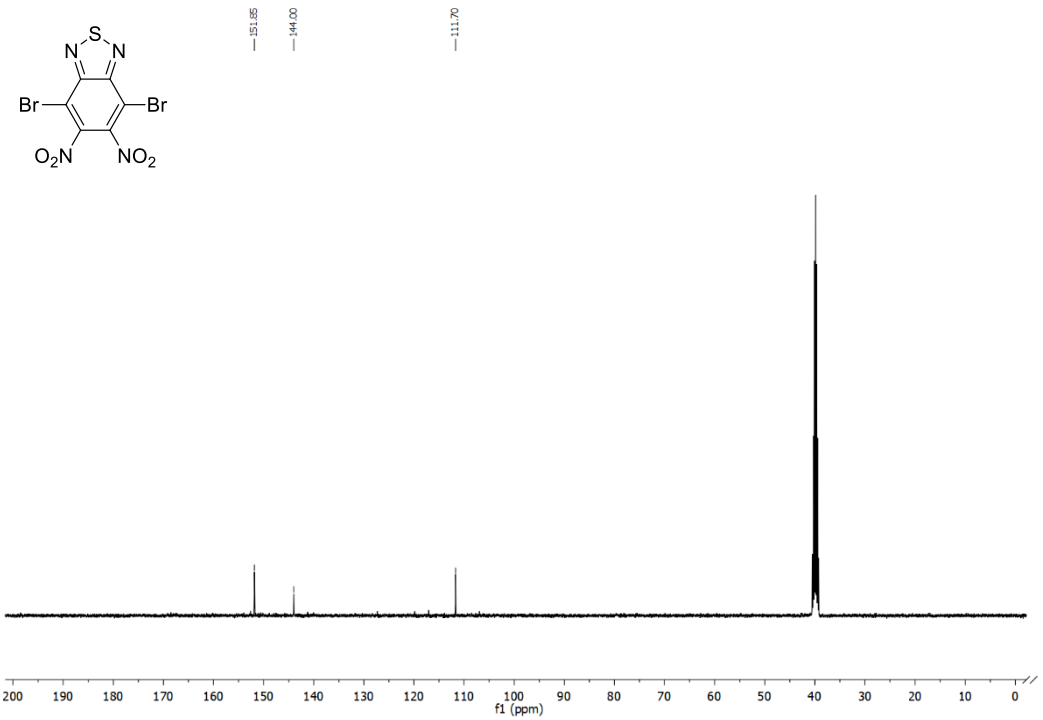

Figure A. 17.13C NMR spectrum of compound 15 in DMSO

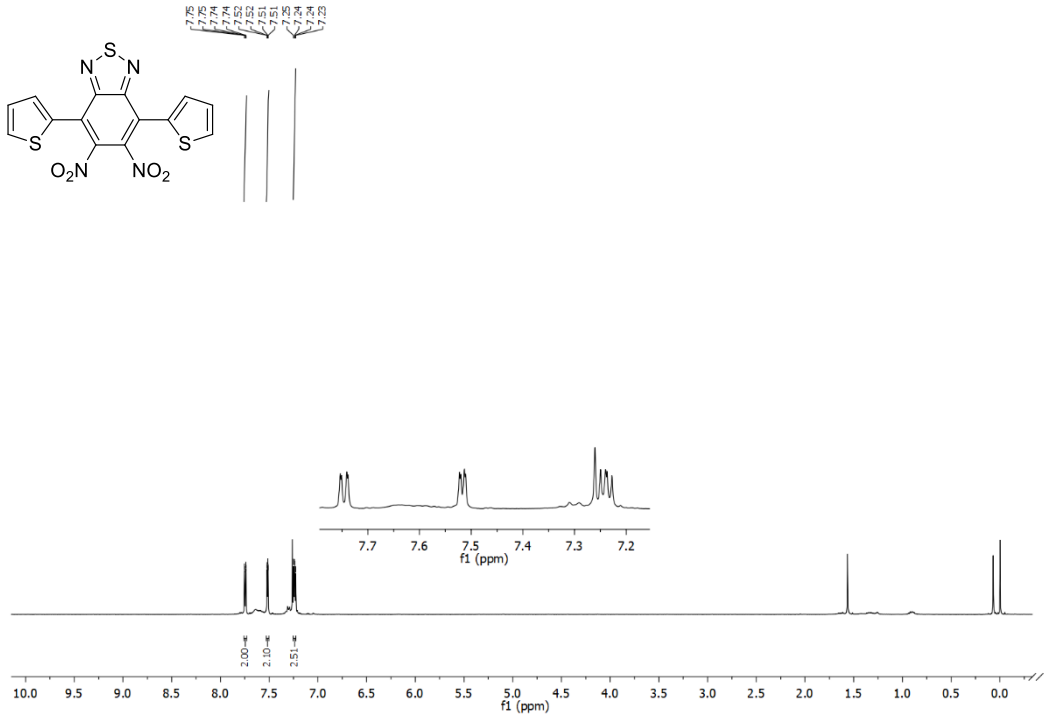

Figure A. 18. ^{1}H NMR spectrum of compound 16 in $CDCl_3$

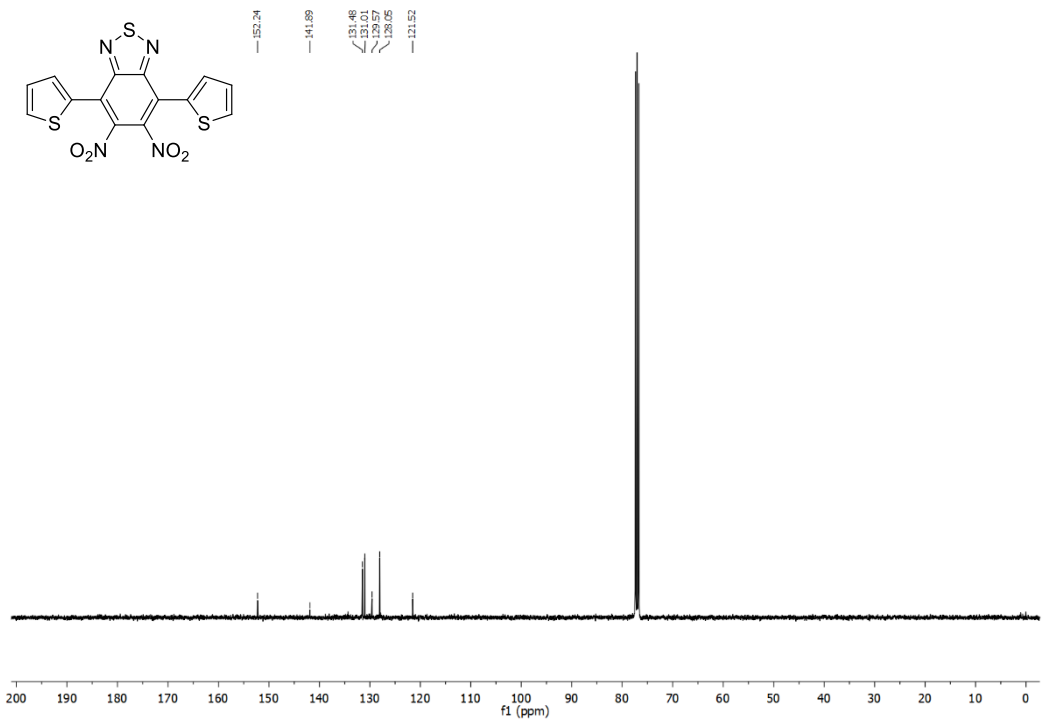

Figure A. 19. ^{13}C NMR spectrum of compound 16 in $CDCl_3$

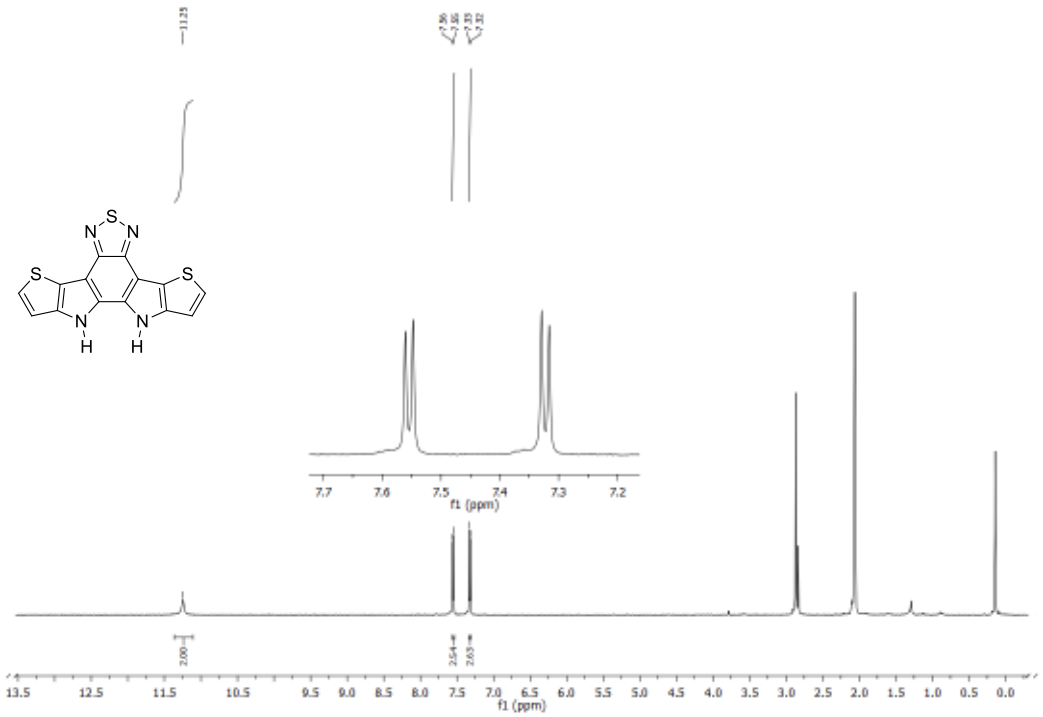

Figure A. 20. ^{1}H NMR spectrum of compound 17 in $(CD_3)_2CO$

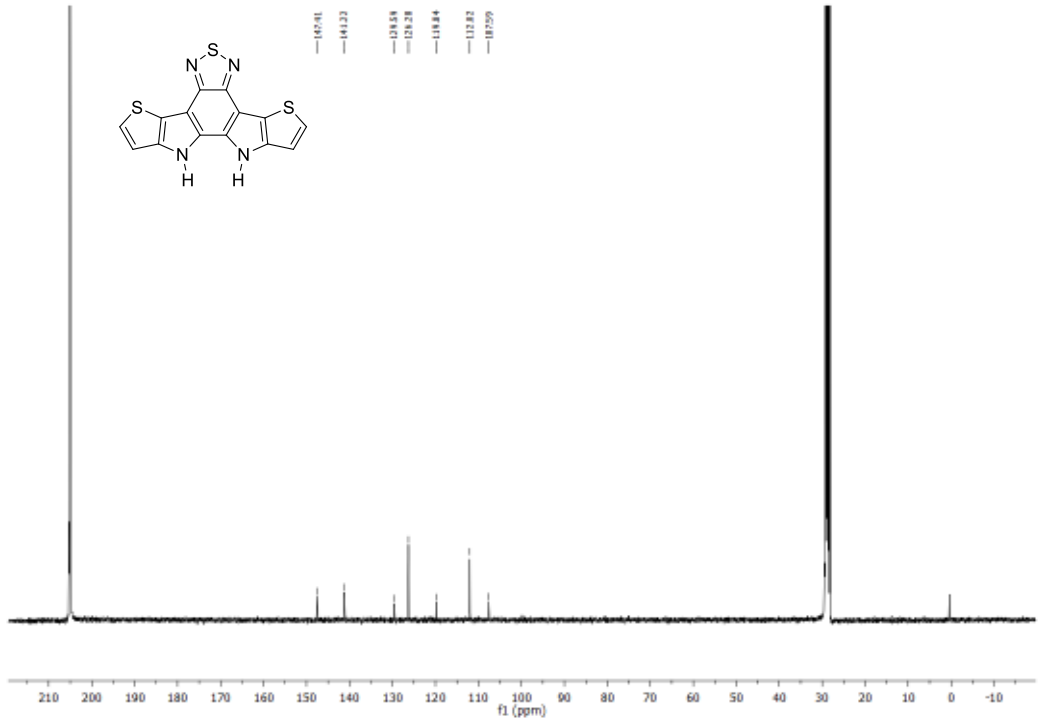

Figure A. 21. ^{13}C NMR spectrum of compound 17 in $(CD_3)_2CO$

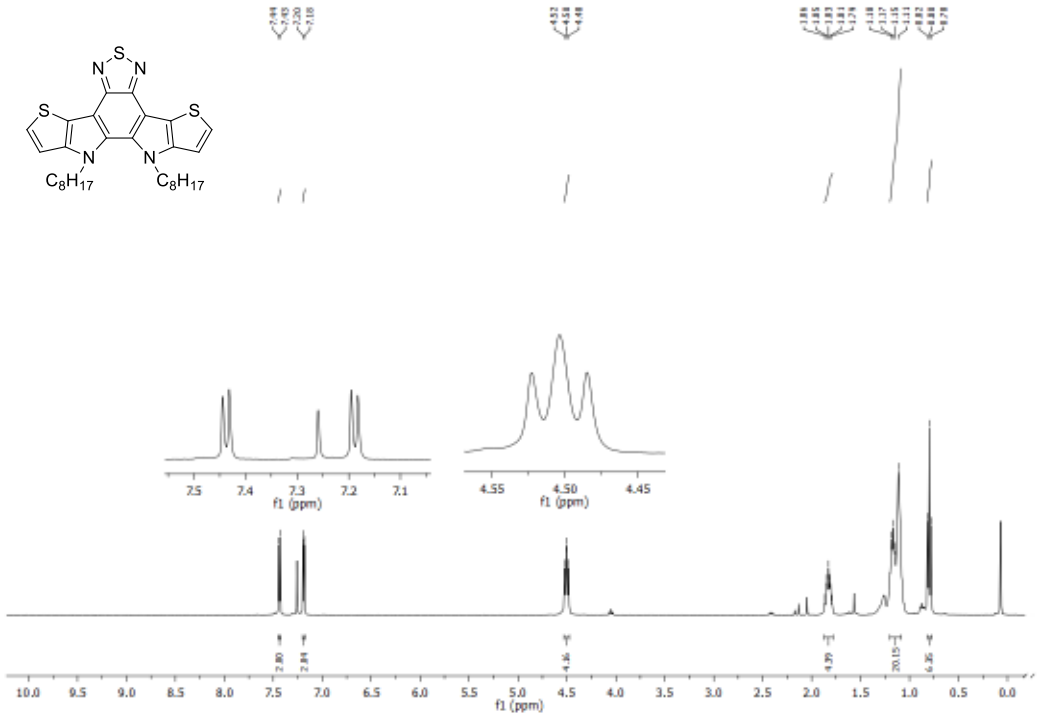

Figure A. 22. ^{1}H NMR spectrum of compound 18 in $CDCl_3$

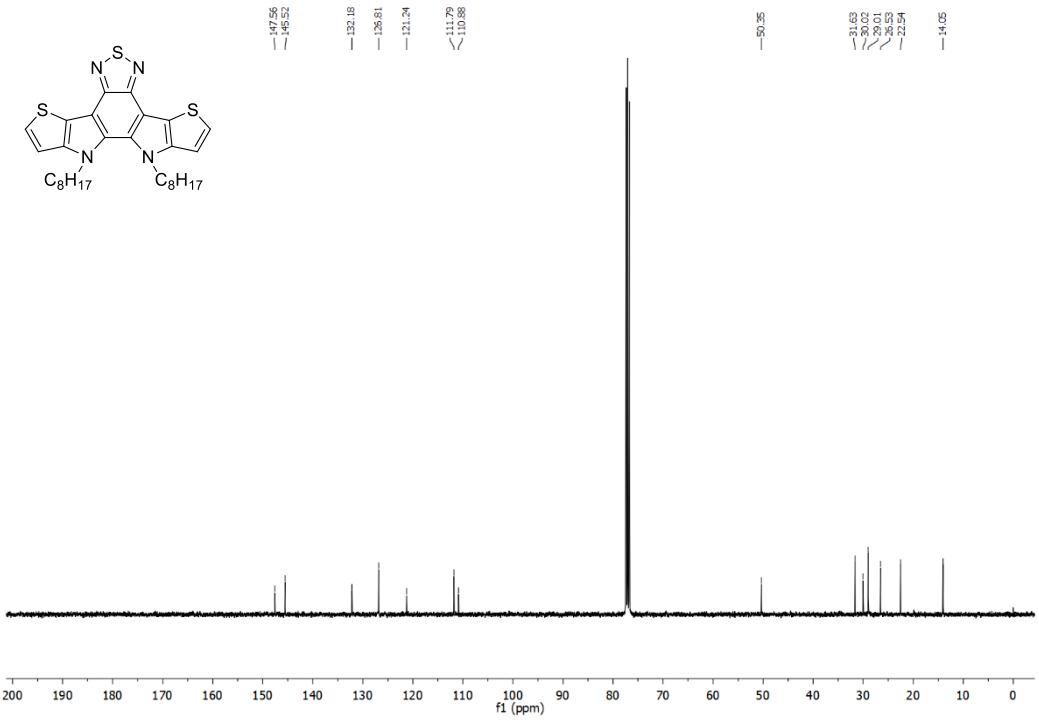

Figure A. 23. ^{13}C NMR spectrum of compound 18 in $CDCl_3$

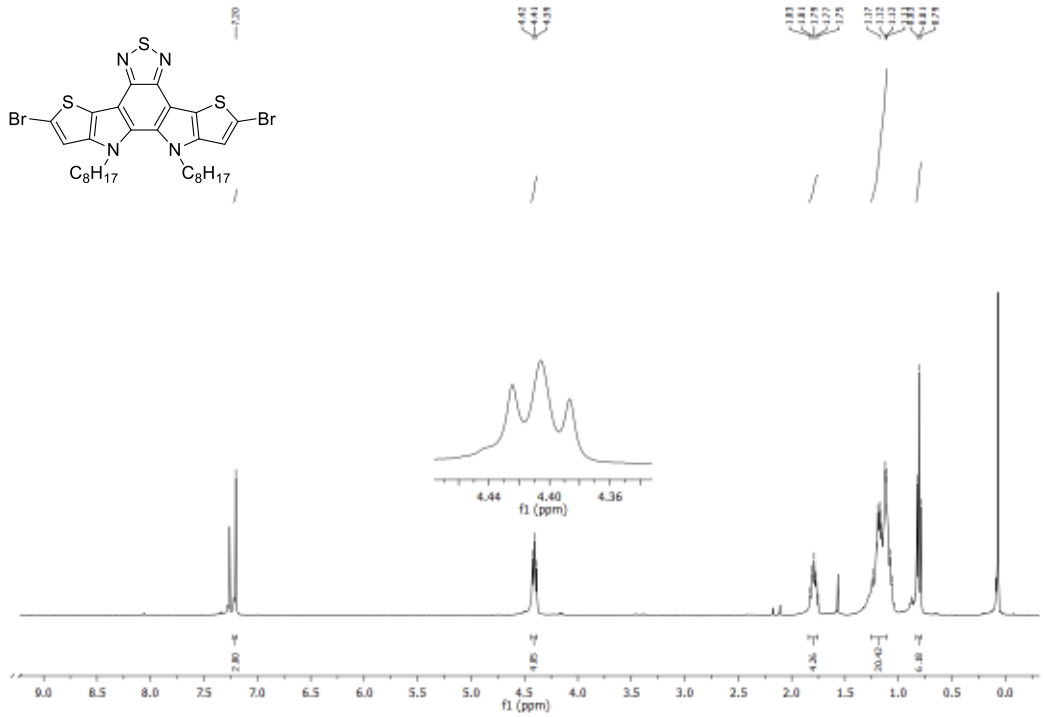

Figure A. 24. ^{1}H NMR spectrum of compound 19 in $CDCl_3$

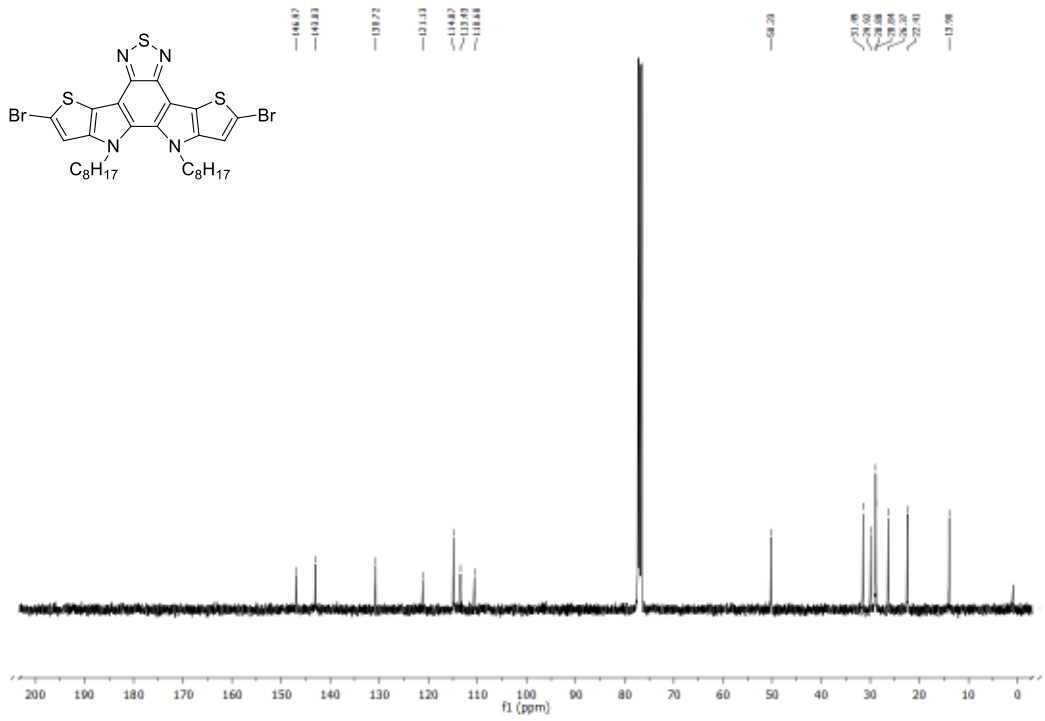

Figure A. 25. ^{13}C NMR spectrum of compound 19 in $CDCl_3$

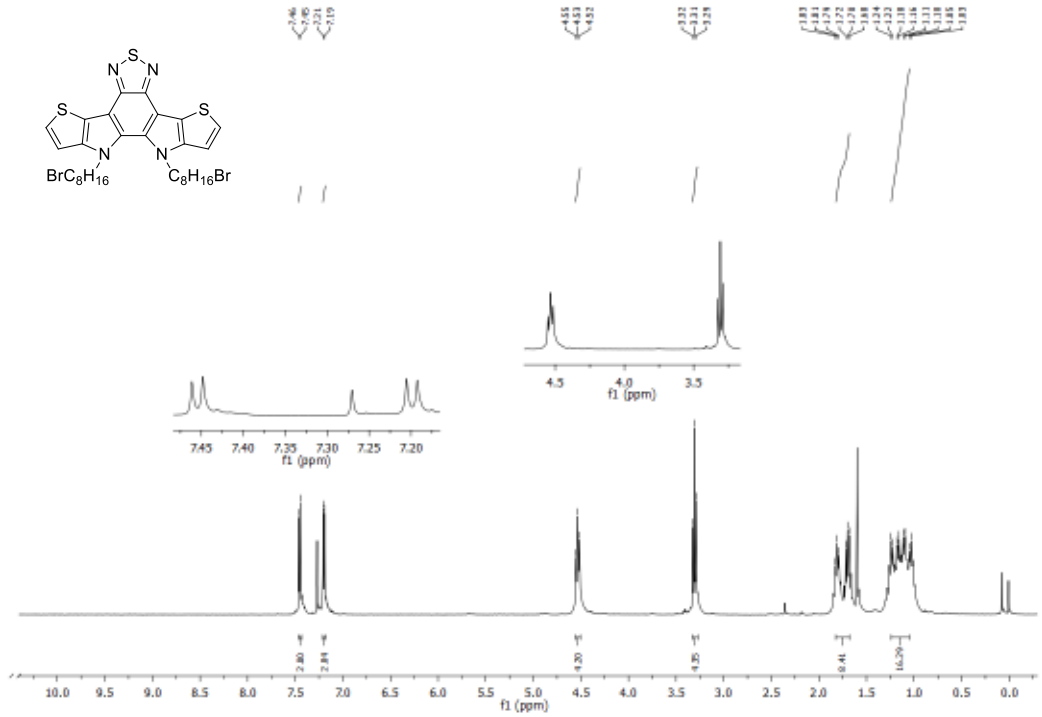

Figure A. 26. ^{1}H NMR spectrum of compound 20 in $CDCl_3$

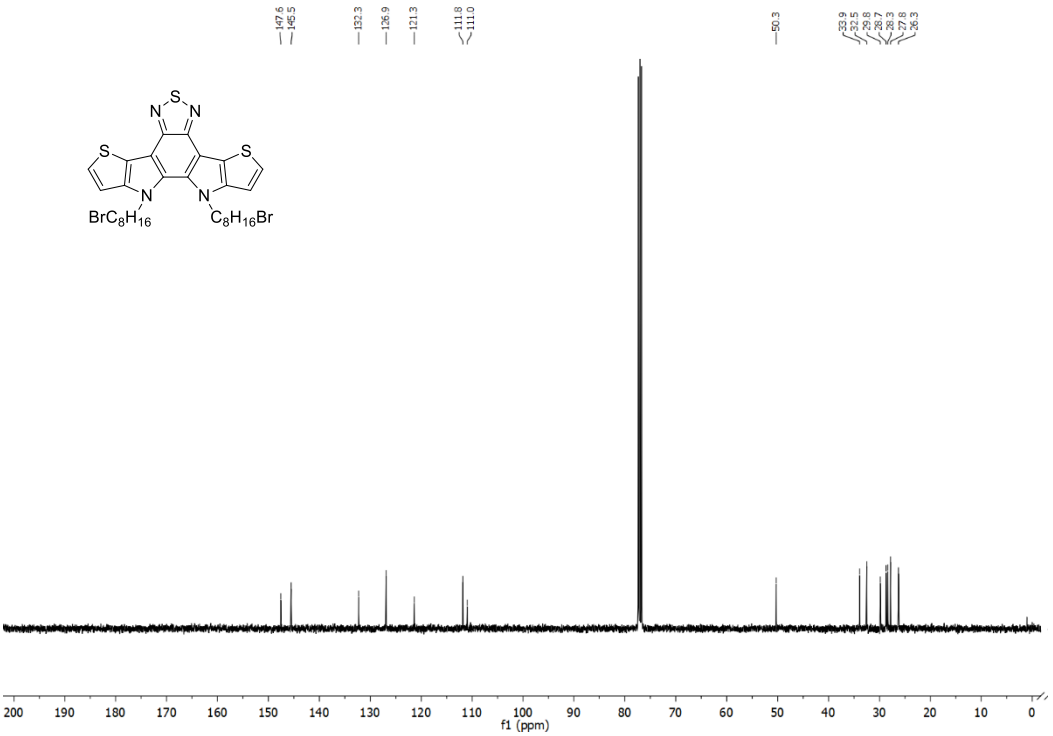

Figure A. 27. ^{13}C NMR spectrum of compound 20 in $CDCl_3$

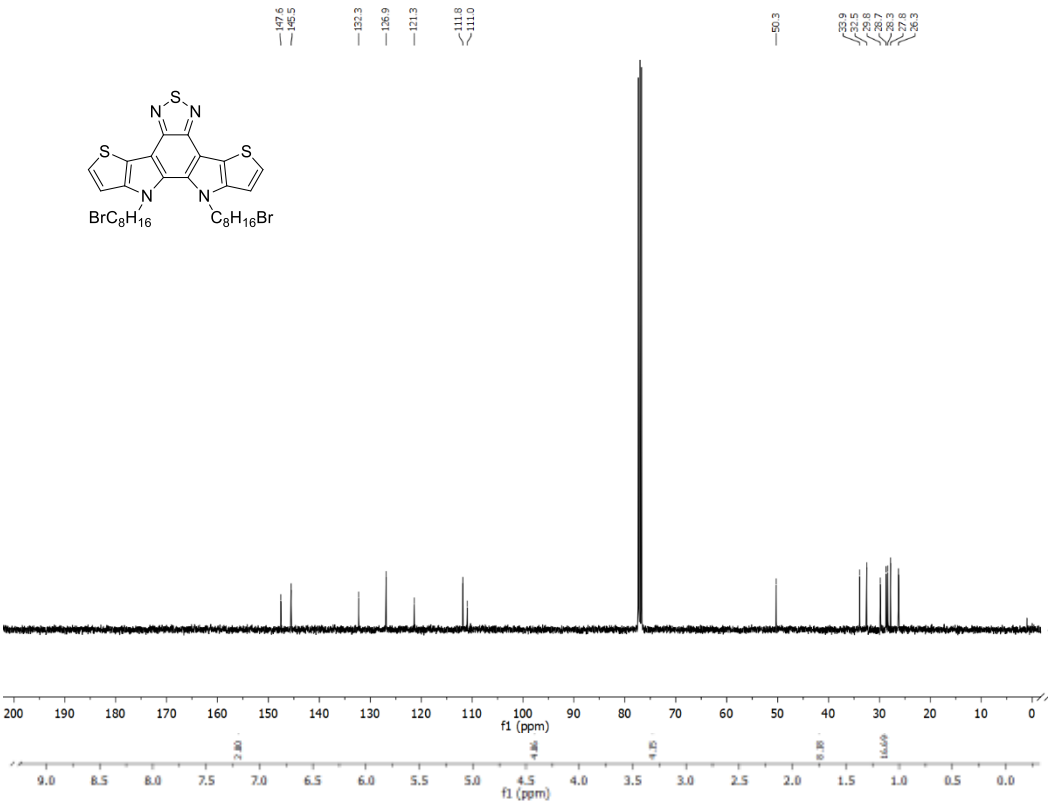

Figure A. 28. ^{1}H NMR spectrum of compound 21 in $CDCl_3$

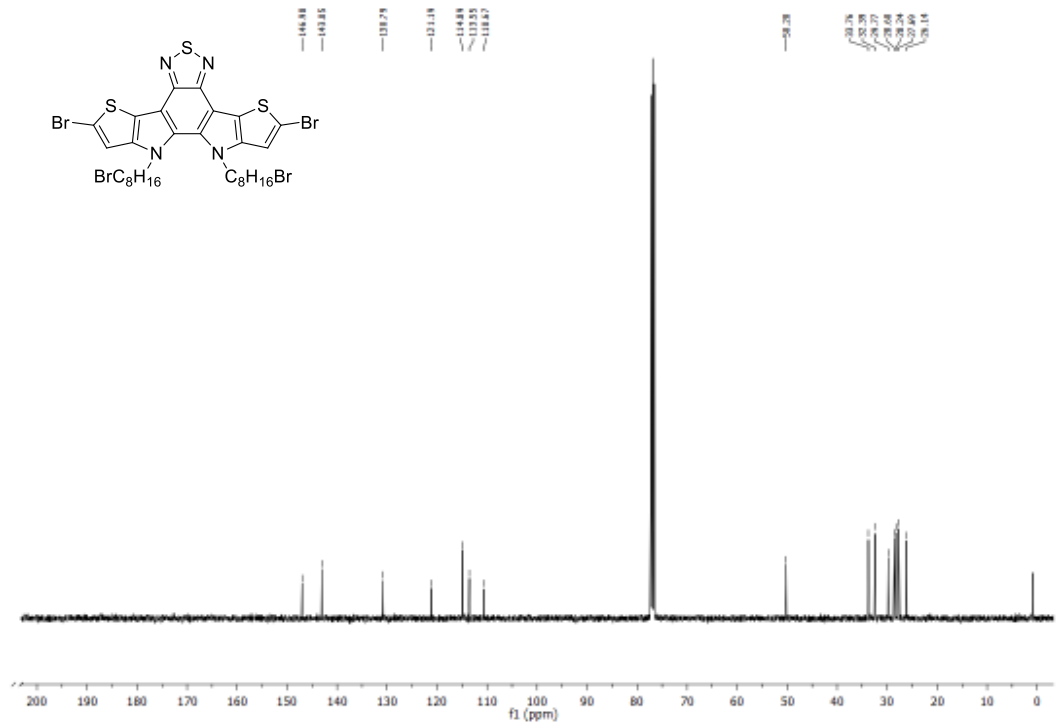

Figure A. 29. ^{13}C NMR spectrum of compound 21 in $CDCl_3$

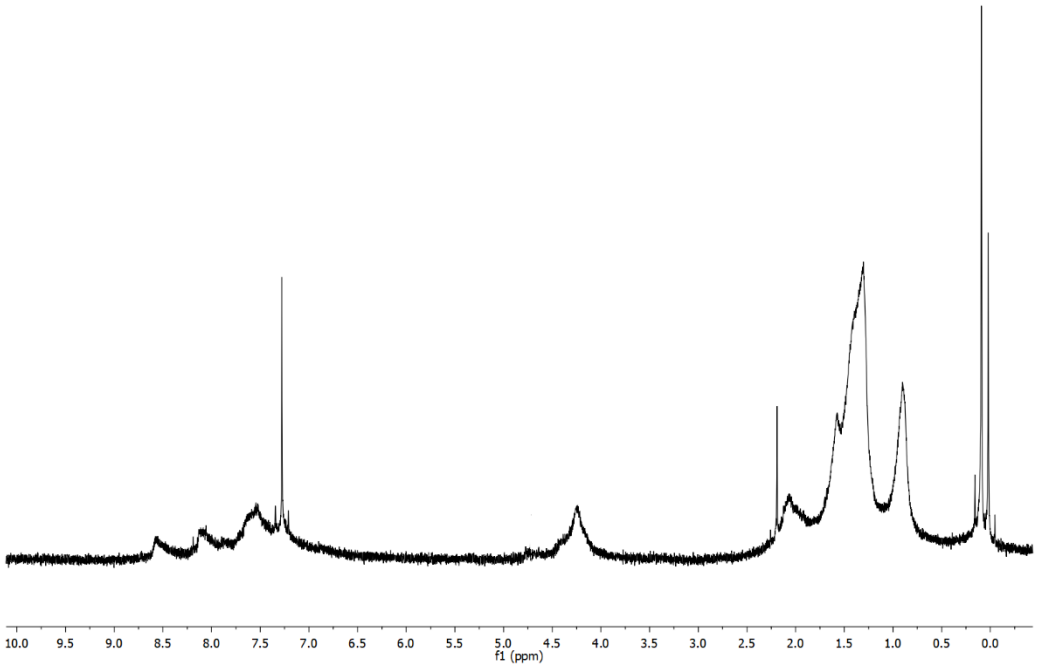

Figure A. 30. ^{1}H NMR spectrum of P1 in $CDCl_3$

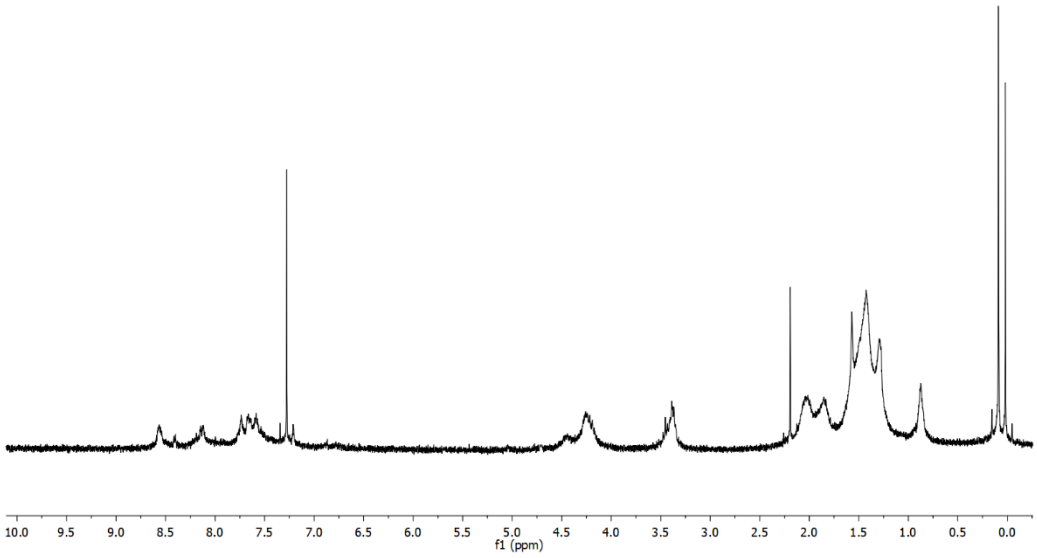

Figure A. 31. ^{1}H NMR spectrum of P1-Br in $CDCl_3$

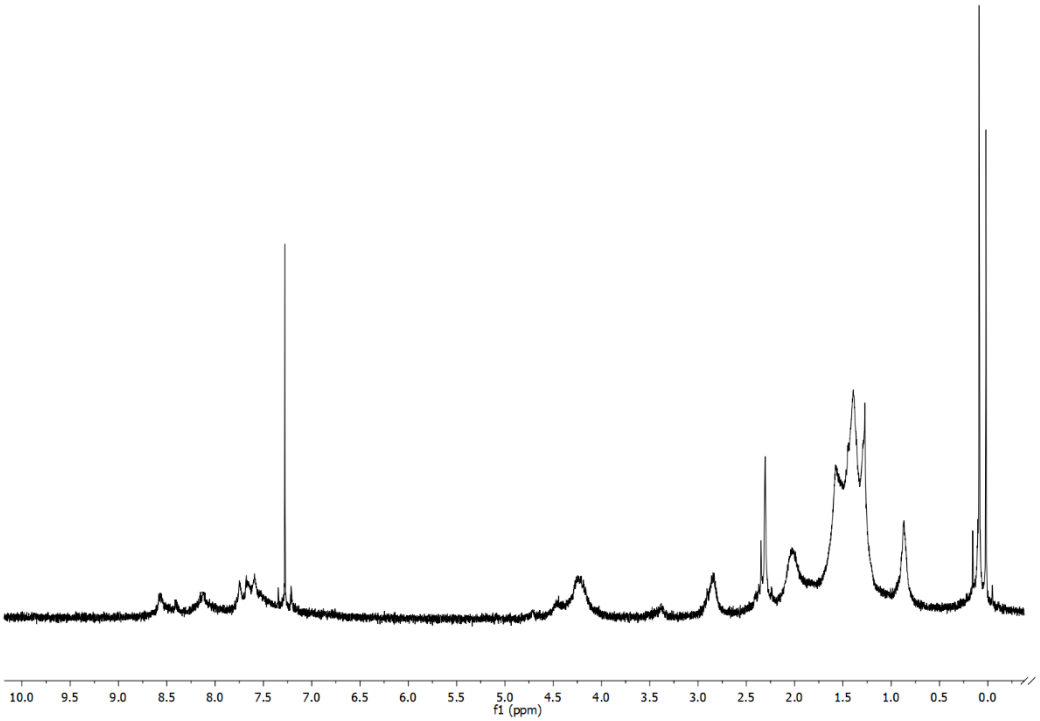

Figure A. 32. ^{1}H NMR spectrum of P1-SH in $CDCl_3$

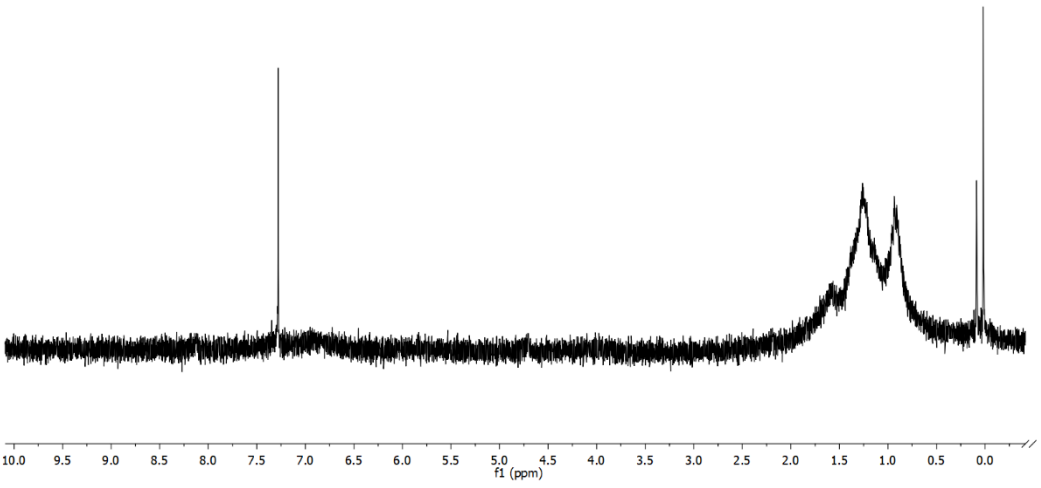

Figure A. 33. ^{1}H NMR spectrum of P2 in $CDCl_3$

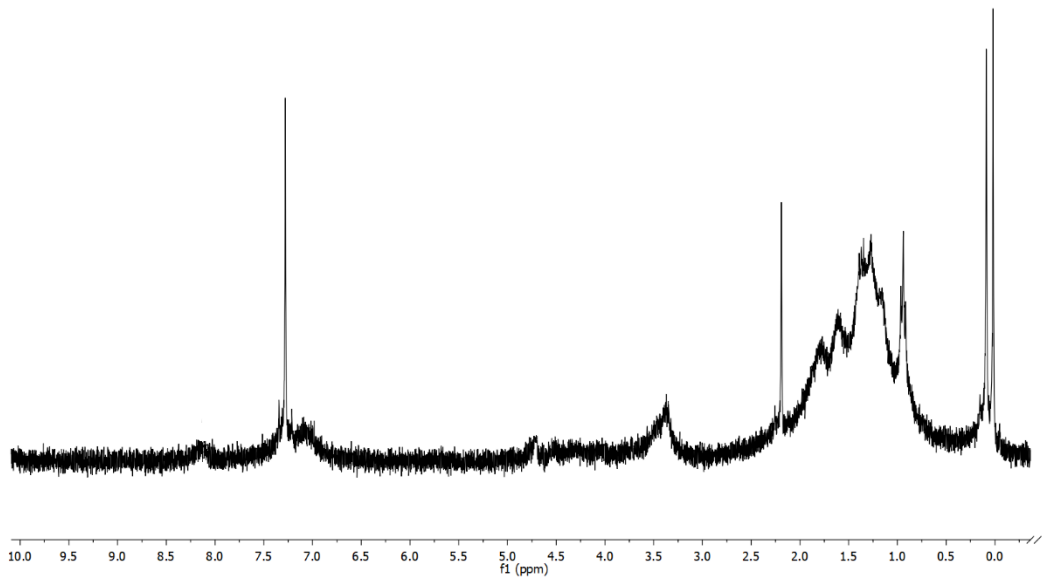

Figure A. 34. ^{1}H NMR spectrum of P3 in $CDCl_3$

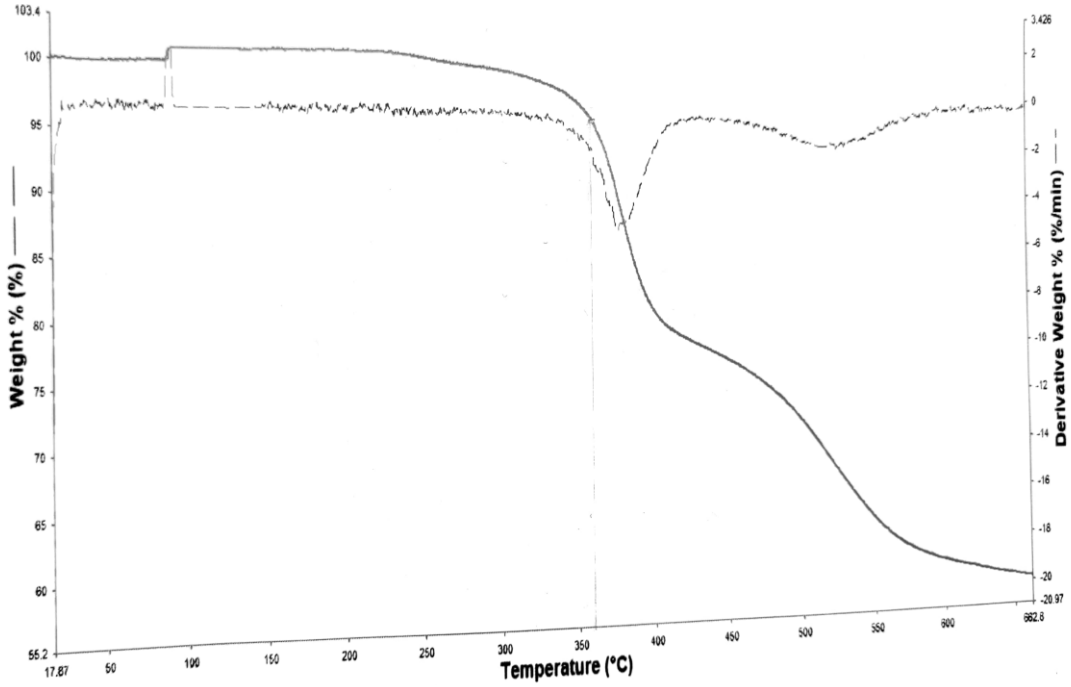

Figure A. 35. TGA analysis of P1

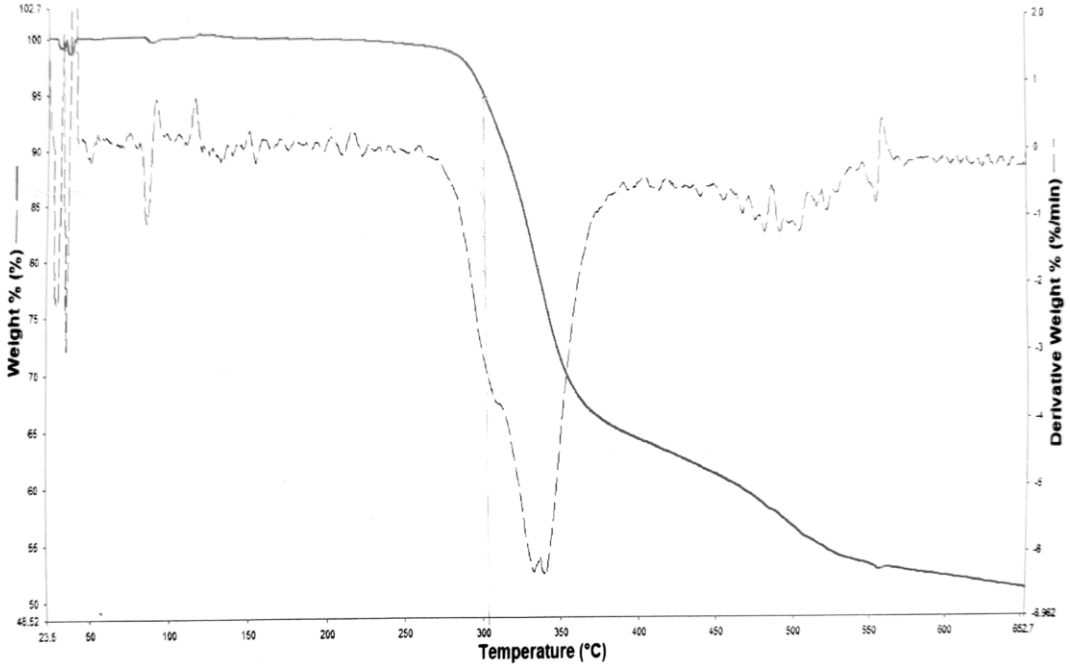

Figure A. 36. TGA analysis of P1-Br

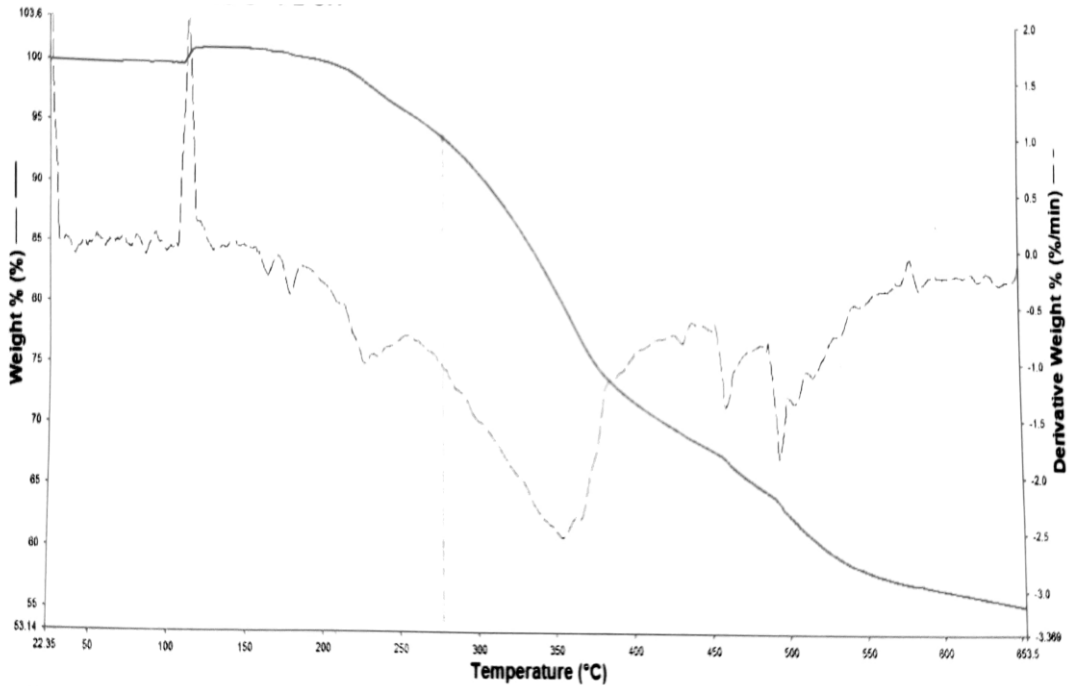

Figure A. 37. TGA analysis of P1-SH

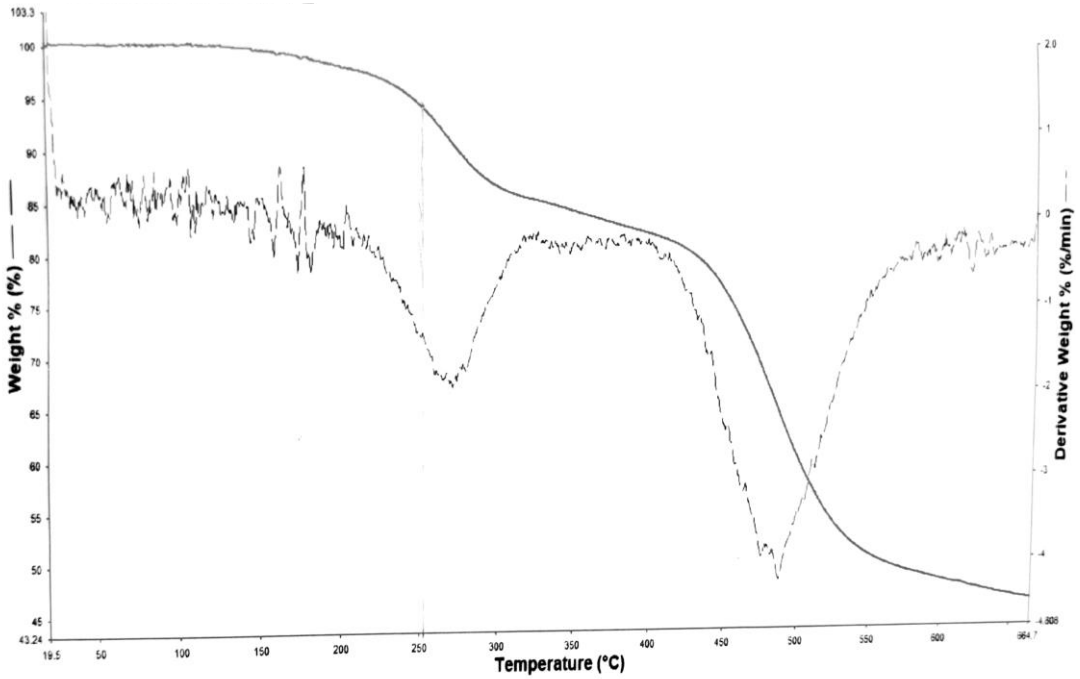

Figure A. 38. TGA analysis of P2

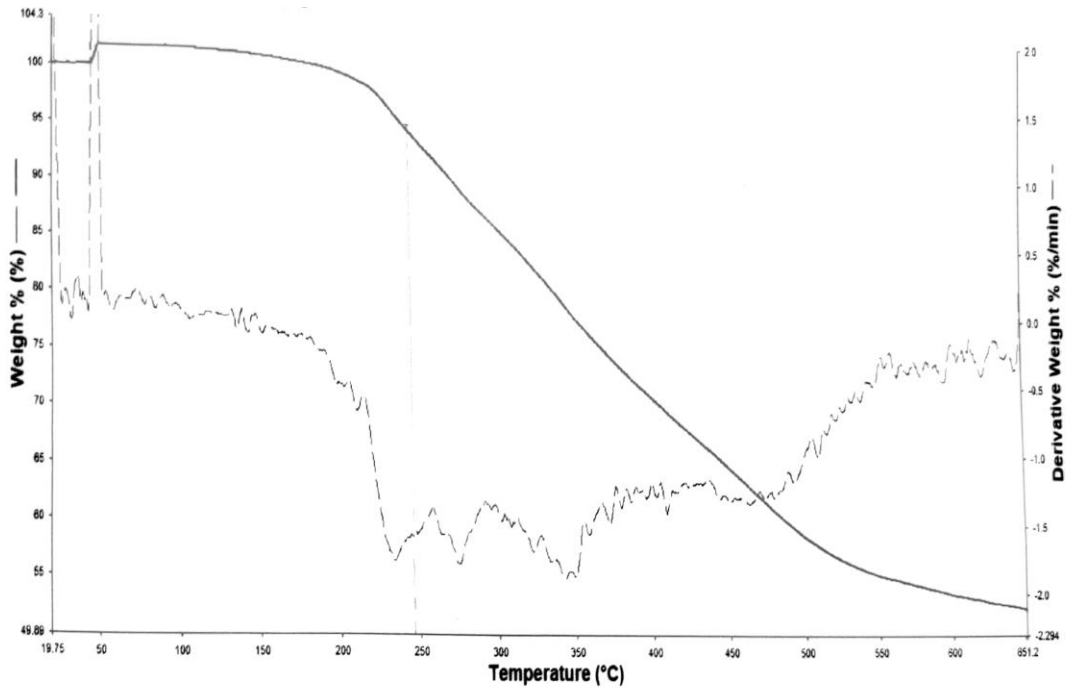

Figure A. 39. TGA analysis of P3

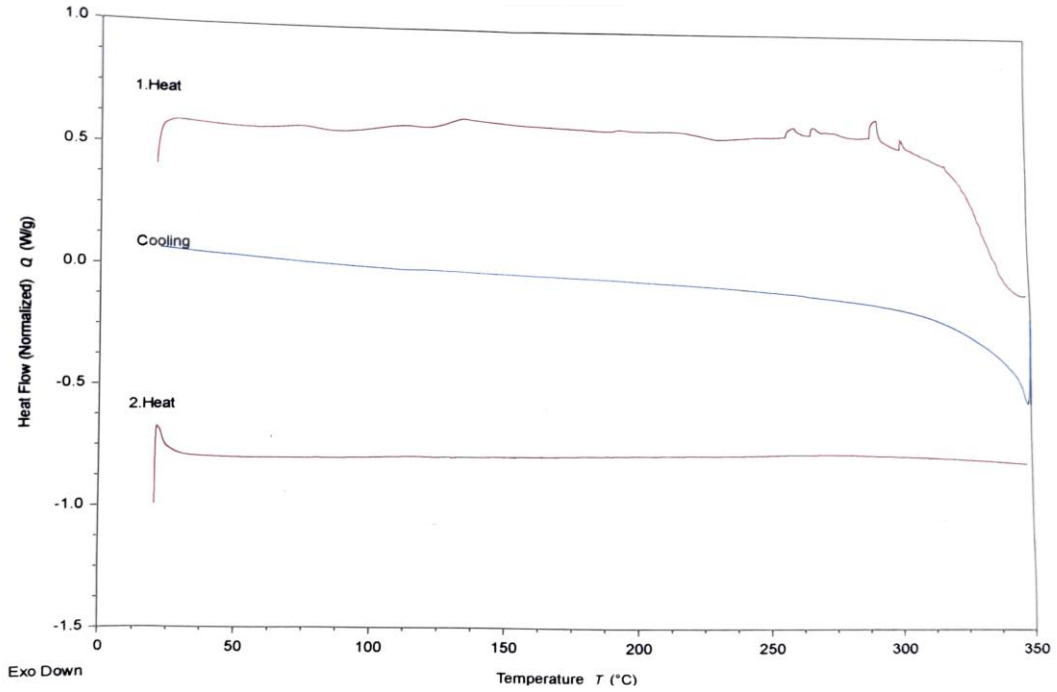

Figure A. 40. DSC analysis of P1

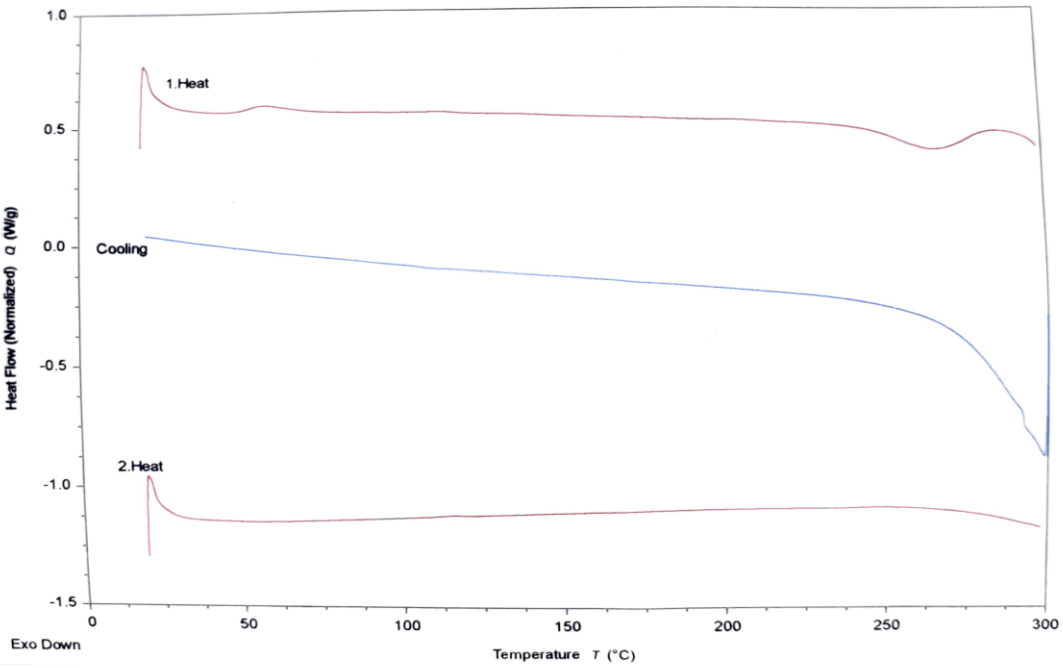

Figure A. 41. DSC analysis of P1-Br

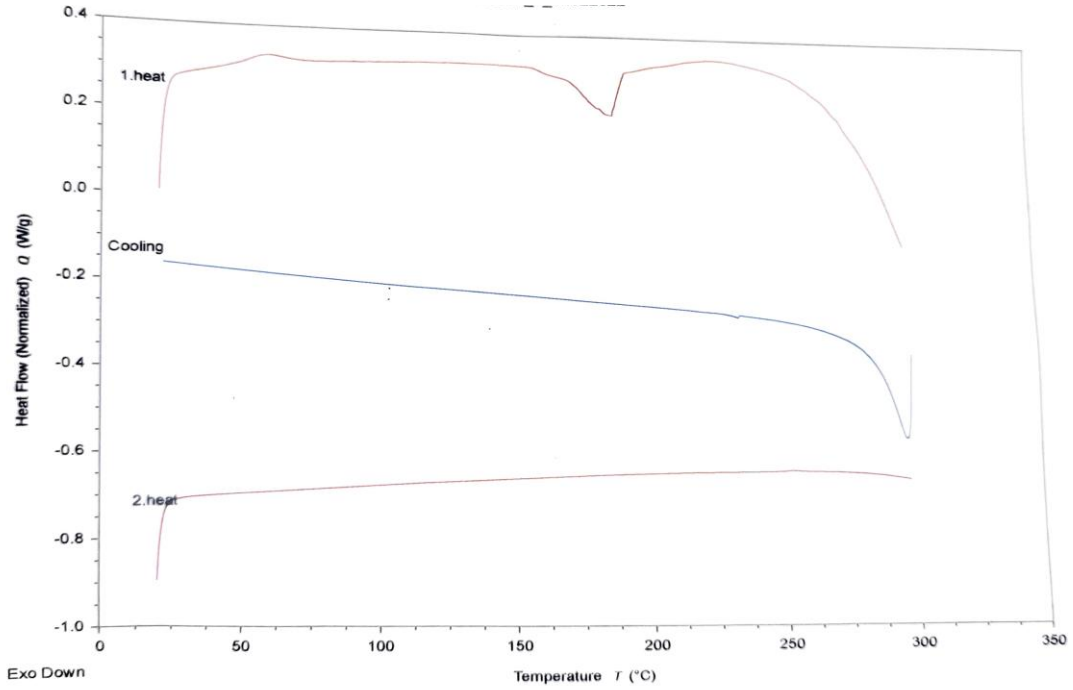

Figure A. 42. DSC analysis of P1-SH

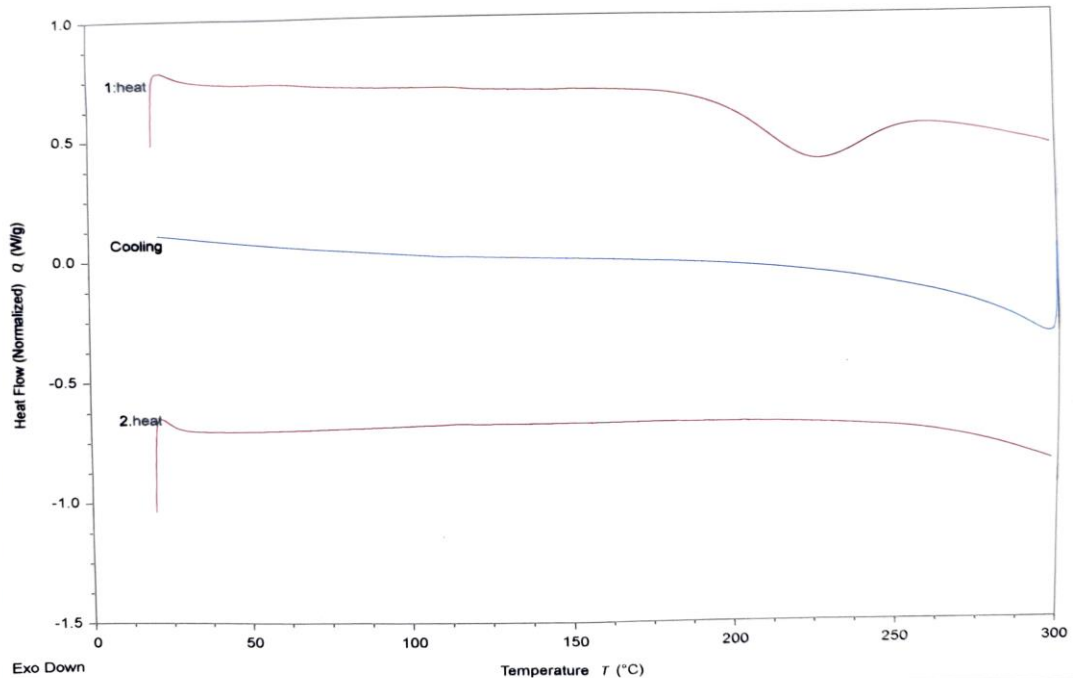

Figure A. 43. DSC analysis of P2

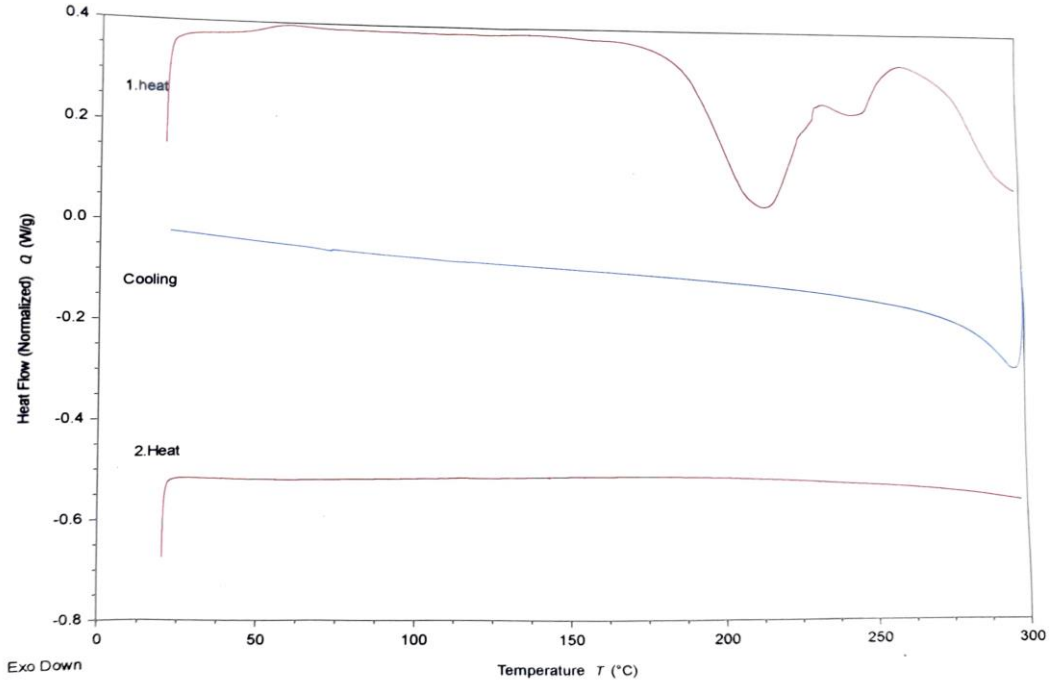

Figure A. 44. DSC analysis of P3